SYNTHESIS AND OPTICAL CHARACTERIZATION OF VANADIUM OXIDE NANOCRYSTALS

by

Mehnaz Tarannum

A dissertation submitted to the faculty of
The University of North Carolina at Charlotte
in partial fulfillment of the requirements
for the degree of Doctor of Philosophy in
Optical Science and Engineering

Charlotte

2024

Approved by:

_____
Dr. Michael Fiddy

_____
Dr. Haitao Zhang

_____
Dr. Tino Hofmann

_____
Dr. Juan Luis Vivero-Escoto

ABSTRACT

MEHNAZ TARANNUM. Synthesis and Optical Characterization of Vanadium Oxide Nanocrystals. (Under the direction of DR. MICHAEL FIDDY)

Nanotechnology has the potential to revolutionize various fields, addressing complex issues such as cancer treatment, waste remediation, and energy storage. To achieve this, precise engineering of nanocrystals at the atomic level is essential, going beyond mere control of size and shape. The unique properties of nanomaterials, which differ from their bulk counterparts, are influenced by surface chemistry, defects, and local structure. These characteristics are determined by the synthesis methods used, making a deep mechanistic understanding of these processes crucial for engineering nanoscale structures and properties. To contribute to the rapidly evolving field of nanoscience, this dissertation focuses on the solution-based synthesis of vanadium oxide nanocrystals. Vanadium oxides are promising candidates for applications in catalysis, sensing, cathode materials for high-density lithium batteries, smart windows, neuromorphic computing, and optical switching. However, vanadium oxides exhibit multiple oxidation states (+2 to +5) and polymorphs. Consequently, the colloidal synthesis of high-quality vanadium oxide nanocrystals in a specific oxidation state and stoichiometry remains challenging. This dissertation advances the synthesis of vanadium oxide nanocrystals, emphasizing the effects of synthetic parameters on their oxidation state and crystal structure. Key findings include the successful synthesis of anosovite V_3O_5 nanocrystals via a hot-injection method, marking the first colloidal synthesis of this rare phase from a readily available precursor. By adjusting vanadium precursor-to-alcohol-to-amine ratio, controlled reduction of vanadium was achieved to selectively synthesize V_3O_5 and V_2O_3 nanocrystals. The dissertation also presents an alcohol-mediated valence-state controlled synthesis method for selective preparation of pure corundum-structured V_2O_3 and anosovite V_3O_5 nanocrystals. Comprehensive characterization, including spectroscopic ellipsometry and diffuse

reflectance spectroscopy, reveals unique optical properties deviating from bulk behavior, attributed to the nanoscale size effects. In addition, a heat-up method was developed for synthesizing VOx nanocrystals by thermal decomposition of vanadyl acetylacetonate, demonstrating the formation of vanadium monoxide nanocrystals. The reaction pathways for the formation of these nanocrystals via hot-injection method and heat-up methods were analyzed with ATR-FTIR spectroscopy. The findings will advance the fundamental understanding of vanadium oxide nanocrystal synthesis and pave the way for their application as advanced functional nanomaterials.

ACKNOWLEDGEMENTS

I extend my deepest gratitude to my academic advisor, Dr. Shunji Egusa, for providing me with the freedom to explore my interests and fostering an environment that encouraged my development as an independent researcher. Not only did he provide me with valuable suggestions on how to write scientific papers, but he also helped me muster the confidence and overcome the discomfort of speaking freely in front of a large audience. He inspired me to step out of my comfort zone, and I will forever be grateful to him for that. I am grateful to my committee chair, Dr. Michael Fiddy, for his support. I would like to express my appreciation to my esteemed committee members, Dr. Zhang, Dr. Hofmann, and Dr. Vivero for their valuable contributions to my academic journey. I am indebted to the Department Chair, Dr. Boreman, and Graduate Program Director, Dr. Tino Hofmann, for their extraordinary support during challenging times. I would like to express my heartfelt gratitude to Dr. Angela Allen, who showed exceptional kindness when I needed it the most. My sincere thanks to Scott Williams, Dr. Lou Deguzman, Daniel Furr, Dr. Jeffery Thousand, Dr. Adam Fessler, Dr. Clifford Carlin and Dr. Youxing Chen for their invaluable help and technical expertise. I would like to acknowledge Dr. Jianing Sun, Dr. Andrea Donohue and Dr. Tom Tiwald from J.A. Woollam for the valuable discussion on spectroscopic ellipsometry. Thanks to my amazing colleagues in Egusa lab – Dr. Jacob Dixon, Alex Palermo and Ratul Ghosh for the exceptional camaraderie. A special thanks goes to Dr. Lisa Russell-Pinson for her guidance in refining my academic writing skills. My heartfelt appreciation goes to my parents and my sister for believing in me and supporting my passion to pursue a degree abroad. My deepest gratitude to Sajjad, Sohan, Liza, Nasheen, Synthia Tagar, Saurav, Faria, Maliha and Maruf for assisting me in settling down in a new country thousands of miles away from home. I am truly grateful for the unwavering support of Suba, Shuchi, Serang, Manira, Madhumita, Luke, Sabeeh, Uma, Arpit,

Venky, Nourin, Shahina and Rasna throughout the duration of my PhD. Thank you so much for holding my hand during difficult times. Special thanks to Ekush-BSO for their support whenever I needed them. I extend my appreciation to Dr. Stacey Martin, my primary care physician, for her remarkable care and support. Lastly, I want to acknowledge Richard O'Neale Atkinson for helping me navigate through the most challenging time of my life. Thank you to every person mentioned for being an integral part of my academic journey and providing invaluable support.

DEDICATION

Strongest women I know on earth, my inspirations: my late grandmother Rabeya M. Hussain, my late aunt Bilkis Begum, and my parents.

TABLE OF CONTENTS

LIST OF FIGURES

LIST OF ABBREVIATIONS

IMT	Insulator – To – Metal Transition
ATR-FTIR	Attenuated Total Reflection Fourier Transform Infrared Spectroscopy
TEM	Transmission Electron Microscopy
XRD	X-ray Diffraction
OAm	Oleylamine
ODE	1-octadecanol
HD	Heptadecane
bp	Boiling Point
HRTEM	High-Resolution Transmission Electron Microscopy
HDD	Hexadecanediol
AFI	Antiferromagnetic Insulator
PM	Paramagnetic Metal
BnOH	Benzyl Alcohol
AFM	Atomic Force Microscope
SEM	Scanning Electron Microscopy
MSE	Mean Squared Error
QP	Quasiparticle

UHB	Upper Hubbard Bands
LHB	Lower Hubbard Bands
acac	Acetylacetonate
OAc	Oleic Acid
BE	Benzyl Ether

CHAPTER 1 : INTRODUCTION

1.1 Nanocrystals

Nanocrystals are crystalline particles with at least one dimension less than 100 nm, containing ten to thousands of atoms. They act as a bridge between molecular and bulk forms of matter, combining aspects of both to create unique materials with properties that are not present in either extreme. Nanocrystals have attracted significant attention over the past several decades due to their unique size-dependent optical, electronic, magnetic, chemical, and mechanical properties.[1-4]

The size-dependent properties observed in the nanoscale regime primarily originate due to the high surface area-to-volume ratio.[5] Fundamental properties, such as the melting temperature of a metal, the bandgap of a semiconductor, or the remanence of a magnet are known to strongly depend on the size of the crystal, particularly in the nanometer range.[6] As structures decrease in size down to nanometer scale, the percentage of surface atoms increases dramatically. Consequently, nanostructures experience different coordination environments and chemical reactivities compared to their bulk counterparts. This presents material scientists with the opportunity to design nanostructured materials with tunable properties through precise control of particle size and surface chemistry.[6]

Studying methods of nanocrystal synthesis is crucial for understanding the properties of nanoscale materials. Synthetic control over the size-uniformity, shape, composition, crystal structure, and surface properties of the nanocrystals is important for understanding their intrinsic properties without the influence of sample inhomogeneity.[7] From a technological point of view, gaining a rigorous understanding of the properties of individual nanocrystals allows researchers to exploit the collective properties of nanocrystal ensembles.[7] This capability is essential for

designing and fabricating innovative electronic, magnetic, and photonic devices as well as other functional materials based on these nanostructures.

Metal oxide nanocrystals are of growing interest for their technological applications, which result from their interesting properties (magnetic, optical, electric) along with general thermal stability, mechanical hardness, and chemical resistance.[4] Among them, vanadium oxides are particularly fascinating for their unique optoelectronic, electrochemical, catalytic, and structural properties.[8-10] However, the study of nanostructured vanadium oxides is often complicated due to the challenges associated with their synthesis. This dissertation focuses on the solution-based synthesis of vanadium oxide nanocrystals, which not only offers a high degree of control over the synthetic parameters but also allows ease of preparation from readily available materials.

1.2 Vanadium Oxides

Vanadium has the electronic configuration [Ar]$4s^2$ $3d^3$, allowing it to exhibit oxidation states ranging from +5 to −3, with +5, +4, +3, and +2 being the most common.[11] Vanadium forms four main oxides with single oxidation states: VO (+2), V_2O_3 (+3), VO_2 (+4), and V_2O_5 (+5), while others possess mixed oxidation states. These oxidation states manifest in various colors: orange to yellow (+5), blue (+4), and green (+3).[12] The physicochemical properties of vanadium oxides are significantly influenced by the oxidation state of vanadium cations, resulting in excellent intercalation properties,[13] high electrical conductivity,[13] catalytic activities,[14] strong electron-electron correlations,[15] and notable phase transitions (insulator–to–metal transition).[16] Additionally, different preparation methods can produce various nanostructures of vanadium oxides, which enhance ion or electron transport, improve solid-state diffusion in electrochemical energy systems,[17, 18] and increase active sites for molecule or ion interactions and exposed crystal facets for catalysis.[19] These characteristics make vanadium oxides highly promising for

applications in energy conversion and storage, such as ion batteries,[20] water splitting,[21] smart windows,[22] supercapacitors,[23] and sensors.[24]

A series of vanadium oxides with strong electron−electron correlations exhibit insulator–to–metal transition (IMT).[25-27] The IMT in metal oxides has captivated researchers in condensed matter materials sciences for decades.[28] Experimental and theoretical investigations have pursued understanding the underlying mechanisms of this transition, yet they remain elusive. The interest in oxide materials experiencing IMT was sparked by Morin's influential work on phase transitions in binary transition-metal oxides during the 1950s.[25] Morin highlighted the remarkable resistance change observed in certain transition-metal oxides, including vanadium oxides (VO_2, V_2O_3, VO) and titanium sesquioxide (Ti_2O_3), as temperature is varied across the transition temperature (T_{IMT}). One common method to trigger the IMT is thermal stimulation, which involves altering the temperature through heating or cooling. Additional methods for inducing IMT include electrical,[29] optical, magnetic, and strain[30] excitations. IMT in a metal oxide is accompanied by a change in structure, electronic, magnetic, or optical properties. For this reason, nanostructured vanadium oxides are promising for applications such as including electronic switches,[31, 32] optical devices,[33] electronic oscillators,[34] metamaterials,[35] memristors,[36] thermal sensors,[37] and chemical sensors.[38]

1.3 Challenges Associated with Synthesis of Vanadium Oxide Based Nanomaterials

Advancements in thin-film oxide growth techniques, including molecular beam epitaxy (MBE),[39] sputtering,[40] chemical vapor deposition (CVD),[41] and pulsed laser deposition (PLD),[42] have aided in exploring device applications of vanadium oxides as phase transition materials. However, it is challenging to achieve epitaxial or highly crystalline stoichiometric films on appropriate substrates while controlling defect concentrations.[43]

As mentioned before, vanadium oxides exhibit multiple oxidation states ranging from V^{2+} to V^{5+} and possess numerous polymorphs, which are compounds with the same chemical composition but different crystal structures. For example, multiple phases of vanadium dioxide (VO_2) have been reported, including VO_2 (M),[44] VO_2 (R),[45] VO_2 (A),[46] VO_2 (B),[47] VO_2 (C),[48] VO_2 (D)[49] and VO_2 (P).[50] In addition to stoichiometric vanadium oxides (VO, V_2O_3, VO_2 and V_2O_5), there are non-stoichiometric oxides with the general formula of V_nO_{2n-1} (Magnéli phases) and V_nO_{2n+1} (Wadsley phases).[51-53] The complex vanadium-oxygen phase diagram is shown in Figure 1.1.[53] Due to a variety of oxidation states and possible coordination environments, it is challenging to synthesize vanadium oxides in a desired oxidation state and structure. Moreover, non-stoichiometry can adversely affect functional properties and introduce leakage currents that degrade device performance or complicate electrical measurements, given that oxides form ionic lattices and defects are often charged.[43] Therefore, achieving high-quality homogeneous vanadium oxide films without forming non-stoichiometric phases remains a challenge.

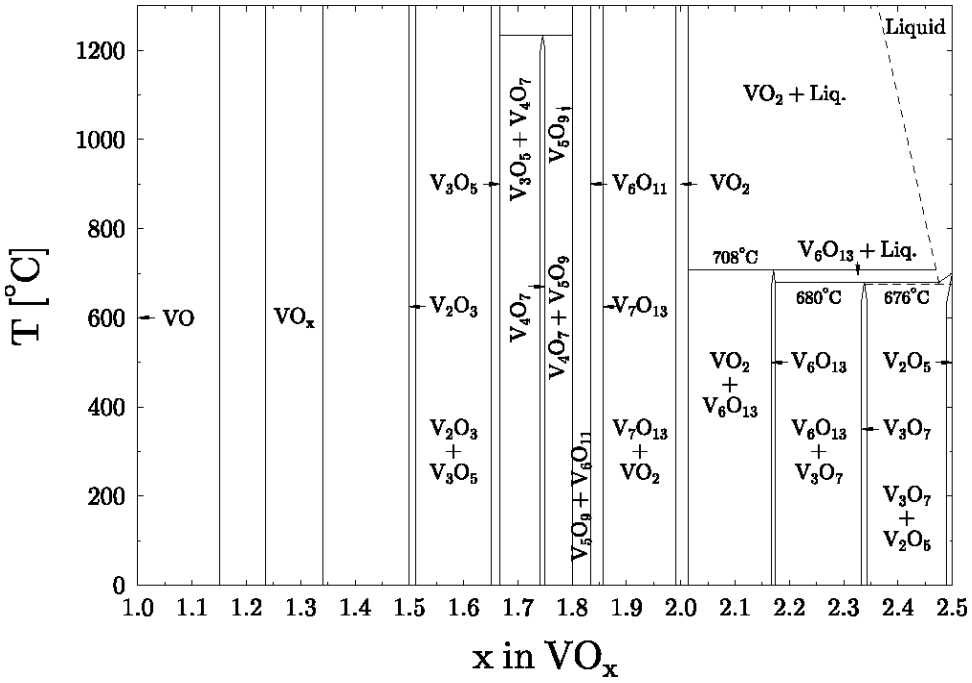

Figure 1.1. Phase diagram of the V−O system.[52]

Nanostructured vanadium oxides are typically prepared utilizing high-temperature metallurgy techniques followed by precise post-synthesis annealing processes, both at carefully controlled oxygen pressures.[40, 42, 54, 55] Optimizing the structure involves selecting lattice-matched substrates, deposition temperature, and method, while stoichiometry is adjusted via precursor deposition rates, background pressure, and post-deposition anneals. These methods are disadvantageous as they offer minimal control over size and, in most cases, require annealing to produce crystalline products.

As an alternative to the above-mentioned methods, a well-controlled colloidal synthesis method is expected to offer size control and size uniformity while eliminating the need for high-temperature post-synthesis annealing, making these materials more readily integrable into devices.[7] Nanocrystal suspensions or powders obtained from solution-based methods can facilitate the study of size-dependent properties without the influence of a substrate.[56, 57] The resulting nanocrystals are also expected to offer improved processability and allow for conformal coating of surfaces.[58]

1.4 Colloidal Synthesis of Metal Oxide Nanocrystals

Colloidal nanocrystals are solution-grown nanometer-sized particles that consists of an inorganic core stabilized by an organic monolayer (also known as capping ligands).[59] The properties of the inorganic core are controlled by their composition, size, and shape. The organic capping layer not only stabilizes the nanocrystals in solution but also provides functional groups that can be used to further modify the surface. This allows for the creation of more complex structures, such as multi-component nanocrystals or nanocrystal assemblies. This combination of attributes makes colloidal nanocrystals promising building blocks for advanced materials and devices.[7]

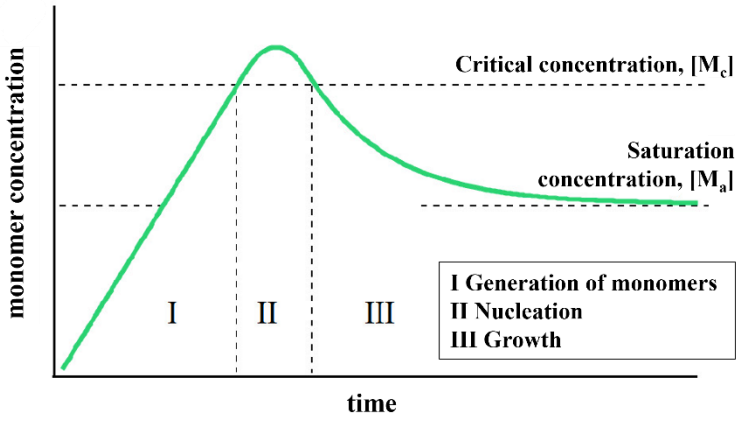

Figure 1.2. LaMer diagram, featuring monomer build-up, nucleation, and growth of nanocrystals in colloidal synthesis.

LaMer and Dinegar's model[60] based on the study of sulfur colloids provides a basis for understanding the nanocrystal growth mechanism in solutions. Three main components in a typical nanocrystal synthesis are: precursors, organic ligands, and solvents. As the reaction medium is heated to the desired temperature, the precursor transforms into monomers, which are the building blocks of nanocrystals. Nanocrystal formation involves two steps: nucleation of seeds and growth. During nucleation stage, monomer concentration reaches a critical concentration [M_c], and then a short burst nucleation occurs with the formation of a finite number of nanoparticles of a critical radius a. The critical radius is the smallest radius at which a nanoparticle does not redissolve. At this point, solution monomers are consumed to form nuclei or seeds, decreasing the solution monomer concentration and preventing the nucleation of new particles. Growth will continue until the monomer concentration is still well above its equilibrium monomer concentration, [M_a] (concentration of monomer required to prevent the dissolution of particles with radius $r \geq a$). If monomer concentration falls below [M_a], then nanoparticles with $r < a$ will dissolve, reforming solution monomer species. Smaller particles will often dissolve first due to their high surface energy, and resulting monomer will support the growth of larger particles. This process is called

Ostwald ripening and is typically used to describe how nanoparticles can become more uniform and monodisperse over time.[61]

Colloidal synthesis often deviates from this straightforward process, however, key principles from the model can provide useful guidance for the synthetic development of nanocrystals. In general, to synthesize monodisperse nanocrystals, it is desirable to separate the nucleation and growth steps in time, meaning nucleation should occur quickly. A rapid nucleation event will reduce the monomer concentration below the nucleation threshold, so remaining monomers in the solution will only add to existing nuclei. Often, there is some overlap between nucleation and growth, resulting in broad size distribution of nanocrystals. However, in optimal conditions, it is possible to maintain a fast growth-focusing regime while staying below the nucleation limit.[7]

There are several methods for synthesis of metal oxide nanocrystals via thermal decomposition. This involves decomposition and consolidation of the precursor in a coordinating or noncoordinating solvent with high boiling point at a high temperature and usually ambient pressure.[59] A common synthetic technique is the hot-injection method, where the metal precursor solution is rapidly injected by hand into a hot solution containing solvent and/or stabilizing ligands. The main advantage of the hot-injection method is that it creates a supersaturation of the monomer species in the beginning of the synthetic procedure, which enables faster nucleation and narrower size dispersion of nanocrystals.[59] Some drawbacks of this method are that nucleation may begin before all the precursor is injected and the injection rate is not constant since it is performed manually. Further, the rapid injection of a lower temperature precursor into a hot solution results in an inhomogeneous reaction temperature, which may affect nanocrystal growth.

Another method is the heat-up method where the metal precursor, organic ligands, and solvent are heated in a mixture to the desired reaction temperature at a controlled rate, and held at this

temperature for a specific amount of time.[62] The size of nanocrystals is determined by the number of nuclei formed during nucleation and can be tuned by varying the temperature ramp rate, the temperature, precursor concentration, and ligand type and concentration. One drawback of heat-up method is that the nanocrystal growth is highly sensitive to the flux of monomer species (derived from the precursor complex) to the surface of the growing crystals.[63] This is difficult to control in heat-up syntheses leading to reproducibility issues. Monomer flux can be controlled by varying the temperature and precursor concentration. However, once the reaction temperature is reached, the precursor concentration—and thus the monomer concentration—changes rapidly, complicating the understanding of how concentration affects nanocrystal growth. Additionally, changing the reaction temperature might necessitate changing the solvent, particularly in reflux reactions where the reaction temperature is set by the solvent's boiling point.[64] When it is required to simultaneously adjust the temperature and solvent, it becomes challenging to systematically study the effect of each parameter on the growth process and the resulting nanocrystal properties.

The size, shape and composition of metal oxide nanocrystals synthesized by thermal decomposition methods are influenced by various synthetic parameters. These include the choice of precursor,[65] precursor-to-ligand ratio, solvent,[66] reaction time,[67] heating rate[67] etc.

The precursor serves as the source of the metal in the metal oxide nanocrystals.[68] Metal acetylacetonates[69] or acetates[63] as well as metal halides[65], have been utilized as precursors. Long-chain hydrocarbons or aromatic compounds selected with high thermal stability and high boiling point are suitable as solvents in nanocrystal syntheses by thermal decomposition. Some of the most common solvents are 1-octadecene[70], benzyl ether,[71] phenyl ether,[69] and squalene.[72] Sun et. al. demonstrated that the solvent choice could affect the size of Fe_3O_4 NCs.[66] 4-nm Fe_3O_4 nanocrystals were synthesized in diphenyl ether (boiling point (bp) = 265 °C), while 6-nm Fe_3O_4 nanocrystals

were obtained in benzyl ether (bp = 300 °C). Ligands passivate the surface of the growing nanocrystals, control or limit their growth, and modify their properties.[73] Amines,[74] carboxylic acids[75] and phosphonic acids[76] are typically used as ligands in nanocrystal synthesis.

The morphology of the TiO_2 nanocrystals was demonstrated to vary significantly depending on the choice of cosurfactant and titanium(IV) halide (TiX_4) precursor under identical reaction conditions.[65] With TiF_4 as the titanium precursor and oleylamine as the cosurfactant, tetragonal bipyramidal anatase NCs were produced.[65] In contrast, using $TiCl_4$ with oleylamine resulted in brookite nanorods. When octadecanol was used as the cosurfactant, TiF_4 produced anatase nanoplates, whereas $TiCl_4$ resulted in tetragonal bipyramidal anatase NCs. It is valuable to systematically understand the roles of these parameters to establish a well-controlled synthesis.[65]

Bennewitz and coworkers demonstrated that the size and composition of MnO nanoparticles can be controlled by the temperature ramping rate and aging time during the thermal decomposition of manganese(II) acetylacetonate.[67] They used two ramping rates (10 °C/min and 20 °C/min) to reach 300 °C, with nanoparticles aged at that temperature for 5, 15, or 30 minutes. A faster ramping rate and shorter aging time produced the smallest nanoparticles (~23 nm). Shorter aging times resulted in a mixture of MnO and Mn_3O_4 nanoparticles, while longer aging times yielded MnO. The optimal condition for forming the smallest pure MnO nanoparticles (~32 nm) was a ramp rate of 20 °C/min with an aging time of 30 minutes.[67]

Each of these parameters discussed above can be finely tuned to achieve desired nanocrystal properties. Therefore, it is important to systematically understand the roles of these parameters to establish a well-controlled colloidal synthesis.

1.5 Colloidal Synthesis of Vanadium Oxide Nanocrystals

While colloidal chemistry offers a high degree of size control and size uniformity, there are only a few reports on direct colloidal synthesis of vanadium oxide nanocrystals. Cheon et al reported synthesis of V_2O_5 nanorods by reacting vanadium oxychloride ($VOCl_3$) with oleic acid and oleylamine in a heat-up synthesis method.[77] This simple method was also applied to synthesize $W_{18}O_{49}$,Mn_3O, and TiO_2 nanocrystals demonstrating the versatility of the method.[77] Synthesis of undoped and Cr–doped V_2O_3 nanocrystals was reported by the thermal decomposition of vanadium (III) and chromium (III) acetylacetonates in the presence of 1,2-dodecanediol, oleylamine, and oleic acid.[78] No temperature-induced phase transition was observed in the undoped V_2O_3 nanocrystals, while Cr–doped nanocrystals exhibited phase transition.[78] Milliron and co-workers reported synthesis of V_2O_3 nanoflowers in metastable bixbyite structure by thermal decomposition of vanadyl(IV) acetylacetonate in the presence of oleylamine, oleic acid and squalene.[72] The size and nanoflower morphology of the particles was shown to be tunable with reaction temperature. The authors suggested that oleylamine reduced the vanadium oxidation state from 4+ in the precursor salt to the final 3+ state in the nanocrystals. Specific precursor-to-oleic acid-to-oleylamine ratio was required to produce the bixbyite phase. No nanocrystals formed in the absence of oleylamine. The crystal structure of the nanocrystals obtained in the absence of oleic acid could not be identified due to broad XRD patterns.[72] Schaak and co-workers prepared colloidal vanadium oxide nanostructures using vanadyl(IV) sulfate ($VOSO_4$) as precursor and commercially available ZnO nanoparticles as a sacrificial template.[79] The resulting product was amorphous which required thermal annealing to obtain VO_2 nanostructures. The resulting nanostructures showed insulator – to – metal transition around 80 °C. Additional tunability of composition, structure, and the transition temperature could be achieved through dopant addition,

modification of reagent delivery and annealing. Murray and co-workers reported synthesis of VO_x nanocrystals by thermal decomposition of vanadium (V) oxytrichloride ($VOCl_3$) in the presence of oleylamine and octadecanol in a hot-injection method.[58] Upon thermal annealing, VO_2 nanocrystals were obtained which showed temperature driven insulator – to – metal phase transition which could be further tuned by tungsten doping.

Despite significant interest in the underlying physics and applications of the nanostructured vanadium oxides as phase transition materials, no direct colloidal synthesis of vanadium dioxide has been reported yet. Furthermore, different synthetic routes often result in nanocrystals with different size distributions which makes it difficult to attribute the nanocrystal properties to a certain size range.[78, 80] This often creates discrepancy in experimentally observed properties. For example, a magnetic phase transition at 80 K was observed in V_2O_3 nanocrystals[80] with diameters of 10–50 nm but V_2O_3 nanocrystals with a diameter of 10.4 ± 1.8 nm did not exhibit such transition. Therefore, it is important to explore the colloidal synthetic routes to obtain vanadium oxide nanocrystals to corroborate the experimental findings in the literature.

1.6 Dissertation Overview

This work focuses on advancement of hot-injection method and heat-up method for the synthesis of vanadium oxide nanocrystals and investigation on the impact of synthetic parameters on nanocrystal size and composition. More specifically, we evaluated the effect of parameters such as choice of precursor, precursor-to-ligand ratio, and solvent on the final product in the syntheses. Additionally, the optical properties of the nanocrystals were characterized using spectroscopy and ellipsometry.

In chapter 2, a valence-state controlled synthesis of vanadium oxide nanocrystals is described by tuning the vanadium precursor-to-reactant ratio. The inherent polyvalence of metals,

particularly the remarkable stability of vanadium(II)–(V), has traditionally hindered achieving the desired oxidation state in vanadium oxide nanocrystal syntheses. However, in our system, polyvalence facilitated the formation of various oxide nanocrystals in a parameter-controlled manner, including anosovite V_3O_5 (V^{4+} + $2V^{3+}$) and corundum V_2O_3 (V^{3+}). Anosovite V_3O_5 is known for its difficulty of formation due to the narrow allowances in the vanadium-to-oxygen ratio. In this work, pre anosovite V_3O_5 was obtained for the first time as nanocrystals ─ a rare phase discovered only recently in bulk form. The time course of the nanocrystal formation revealed a slow seeded growth process, separated from a subsequent fast growth via Ostwald ripening. The reaction intermediates were characterized using ATR-FTIR spectroscopy to assess the reaction pathways in the formation of the nanocrystals. The phase stability of V_3O_5 nanocrystals were evaluated at elevated temperatures which confirmed superior stability compared to the bulk counterpart. This chapter was published as: M. Tarannum, W. P. Heidtmann, J. M. Dixon, S. Egusa. Valence State-Controlled Synthesis of Vanadium Oxide Nanocrystals. J. Phys. Chem. C 2023, 127, 1, 490–498. Copyright 2022 American Chemical Society.

Chapter 3 describes an alcohol mediated valence-state controlled synthesis of vanadium oxide nanocrystals. Pure corundum V_2O_3 was obtained in the presence of a tertiary alcohol while V_3O_5 was obtained in the presence of a primary alcohol. Diffuse reflectance spectroscopy measurements of the V_2O_3 nanocrystals indicated different optical properties when compared to that of the bulk V_2O_3. Complex dielectric functions, complex indices of refraction, and optical conductivities of both V_2O_3 and V_3O_5 nanocrystal thin films were determined using spectroscopic ellipsometry. This chapter was published as: M. Tarannum, S. Egusa. Optical Properties of Correlated Metallic V_2O_3 and Anosovite V_3O_5 Nanocrystals and Nanocrystal Films. J. Phys. Chem. C 2024, 128, 10, 4215–4223. Copyright 2024 The Authors.

In chapter 4, a heat-up method for synthesizing colloidal VO_x nanocrystals is introduced. High size-uniformity VO_x nanocrystals were achieved through the thermal decomposition of vanadyl acetylacetonate in the presence of oleylamine and benzyl ether. FTIR analysis of reaction intermediates indicated the formation of a complex between the acetylacetonate precursor and oleylamine, as well as the production of an imine byproduct. The feasibility of other solvents, such as octyl ether and heptadecane, was also explored. Seed-mediated growth was attempted to obtain nanocrystals with a discernible crystal structure, but these attempts were unsuccessful. Introducing oleic acid as an additional ligand led to the formation of anosovite V_3O_5 nanocrystals.

Finally, in Chapter 5, future work is suggested, including IR ellipsometry of V_2O_3 and V_3O_5 nanocrystal films, evaluating doping effect in optical properties of V_2O_3, and strategies to explore other colloidal synthetic routes to obtain vanadium oxide nanocrystals.

REFERENCES

1. Alivisatos, A. P., Semiconductor clusters, nanocrystals, and quantum dots. *science* **1996,** *271*, 933-937.

2. Murray, C. B.; Kagan, C. R.; Bawendi, M. G., Synthesis and characterization of monodisperse nanocrystals and close-packed nanocrystal assemblies. *Annual review of materials science* **2000,** *30*, 545-610.

3. Burda, C.; Chen, X.; Narayanan, R.; El-Sayed, M. A., Chemistry and properties of nanocrystals of different shapes. *Chem Rev* **2005,** *105*, 1025-102.

4. Kovalenko, M. V.; Manna, L.; Cabot, A.; Hens, Z.; Talapin, D. V.; Kagan, C. R.; Klimov, V. I.; Rogach, A. L.; Reiss, P.; Milliron, D. J.; Guyot-Sionnnest, P.; Konstantatos, G.; Parak, W. J.; Hyeon, T.; Korgel, B. A.; Murray, C. B.; Heiss, W., Prospects of nanoscience with nanocrystals. *ACS Nano* **2015,** *9*, 1012-57.

5. Uvarov, N. F.; Boldyrev, V. V., Size effects in chemistry of heterogeneous systems. *Russian Chemical Reviews* **2001,** *70*, 265-284.

6. Alivisatos, A. P., Nanocrystals: building blocks for modern materials design. *Endeavour* **1997,** *21*, 56-60.

7. Yin, Y.; Alivisatos, A. P., Colloidal nanocrystal synthesis and the organic-inorganic interface. *Nature* **2005,** *437*, 664.

8. Nag, J.; Haglund Jr, R. F., Synthesis of vanadium dioxide thin films and nanoparticles. *Journal of Physics: Condensed Matter* **2008,** *20*, 264016.

9. Blasco, T.; Nieto, J. M. L., Oxidative dyhydrogenation of short chain alkanes on supported vanadium oxide catalysts. *Applied Catalysis A: General* **1997,** *157*, 117-142.

10. Talledo, A.; Granqvist, C. G., Electrochromic vanadium–pentoxide–based films: Structural, electrochemical, and optical properties. *J. Appl. Phys.* **1995,** *77*, 4655-4666.

11. Cotton, F. A.; Wilkinson, G.; Murillo, C. A.; Bochmann, M., *Advanced Inorganic Chemistry*. 1999.

12. Rehder, D., The future of/for vanadium. *Dalton Trans* **2013,** *42*, 11749-61.

13. Wu, C. Z.; Xie, Y., Promising vanadium oxide and hydroxide nanostructures: from energy storage to energy saving. *Energ Environ Sci* **2010,** *3*, 1191-1206.

14. Liu, M.; Su, B.; Tang, Y.; Jiang, X.; Yu, A., Recent Advances in Nanostructured Vanadium Oxides and Composites for Energy Conversion. *Adv. Energy Mater.* **2017,** *7*, 1700885.

15. Wei, J.; Ji, H.; Guo, W.; Nevidomskyy, A. H.; Natelson, D., Hydrogen Stabilization of Metallic Vanadium Dioxide in Single-Crystal Nanobeams. *Nat. Nanotechnol.* **2012,** *7*, 357.

16. Jang, H. W.; Felker, D. A.; Bark, C. W.; Wang, Y.; Niranjan, M. K.; Nelson, C. T.; Zhang, Y.; Su, D.; Folkman, C. M.; Baek, S. H., Metallic and Insulating Oxide Interfaces Controlled by Electronic Correlations. *Science* **2011,** *331*, 886.

17. Lee, J. H.; Kim, J. M.; Kim, J. H.; Jang, Y. R.; Kim, J. A.; Yeon, S. H.; Lee, S. Y., Energy Storage: Toward Ultrahigh-Capacity V2O5 Lithium-Ion Battery Cathodes via One-Pot Synthetic Route from Precursors to Electrode Sheets. *Adv. Mater. Interfaces* **2016,** *3*, 1600173.

18. Cao, A. M.; Hu, J. S.; Liang, H. P.; Wan, L. J., Self-Assembled Vanadium Pentoxide (V2O5) Hollow Microspheres from Nanorods and Their Application in Lithium-Ion Batteries. *Angew. Chem., Int. Ed.* **2005,** *44*, 4391.

19. Liu, G.; Yu, J. C.; Lu, G. Q.; Cheng, H. M., Crystal Facet Engineering of Semiconductor Photocatalysts: Motivations, Advances and Unique Properties. *Chem. Commun.* **2011,** *47*, 6763.

20. Xu, X.; Xiong, F.; Meng, J.; Wang, X.; Niu, C.; An, Q.; Mai, L., Vanadium-Based Nanomaterials: A Promising Family for Emerging Metal-Ion Batteries. *Adv. Funct. Mater.* **2020,** *30*, 1904398.

21. Gonçalves, J. M.; Ireno da Silva, M.; Angnes, L.; Araki, K., Vanadium-Containing Electro and Photocatalysts for the Oxygen Evolution Reaction: a Review. *J. Mater. Chem. A* **2020,** *8*, 2171.

22. Ke, Y.; Chen, J.; Lin, G.; Wang, S.; Zhou, Y.; Yin, J.; Lee, P. S.; Long, Y., Smart Windows: Electro-, Thermo-, Mechano-, Photochromics, and Beyond. *Adv. Energy Mater.* **2019,** *9*, 1902066.

23. Chen, D.; Li, J.; Wu, Q., Review of V2O5-Based Nanomaterials as Electrode for Supercapacitor. *J. Nanopart. Res.* **2019,** *21*, 201.

24. Mounasamy, V.; Mani, G. K.; Madanagurusamy, S., Vanadium Oxide Nanostructures for Chemiresistive Gas and Vapour Sensing: a Review on State of the Art. *Microchim. Acta* **2020,** *187*, 253.

25. Morin, F. J., Oxides Which Show a Metal-to-Insulator Transition at the Neel Temperature. *Phys. Rev. Lett.* **1959,** *3*, 34-36.

26. Zylbersztejn, A.; Mott, N. F., Metal-insulator transition in vanadium dioxide. *Phys. Rev. B* **1975,** *11*, 4383.

27. Nadkarni, G. S.; Shirodkar, V. S., Experiment and Theory for Switching in Al/V2O5/Al Devices. *Thin Solid Films* **1983,** *105*, 115.

28. Mott, N. F., Metal-Insulator Transition. *Reviews of Modern Physics* **1968,** *40*, 677-683.

29. Tokura, Y., Correlated-Electron Physics in Transition-Metal Oxides. *Physics Today* **2003,** *56*, 50-55.

30. Cao, J.; Ertekin, E.; Srinivasan, V.; Fan, W.; Huang, S.; Zheng, H.; Yim, J. W.; Khanal, D. R.; Ogletree, D. F.; Grossman, J. C.; Wu, J., Strain engineering and one-dimensional organization of metal-insulator domains in single-crystal vanadium dioxide beams. *Nat Nanotechnol* **2009,** *4*, 732-7.

31. Ruzmetov, D.; Gopalakrishnan, G.; Deng, J.; Narayanamurti, V.; Ramanathan, S., Electrical triggering of metal-insulator transition in nanoscale vanadium oxide junctions. *J. Appl. Phys.* **2009,** *106*.

32. Ruzmetov, D.; Gopalakrishnan, G.; Ko, C.; Narayanamurti, V.; Ramanathan, S., Three-terminal field effect devices utilizing thin film vanadium oxide as the channel layer. *J. Appl. Phys.* **2010,** *107*.

33. Briggs, R. M.; Pryce, I. M.; Atwater, H. A., Compact silicon photonic waveguide modulator based on the vanadium dioxide metal-insulator phase transition. *Opt Express* **2010,** *18*, 11192-201.

34. Gu, Q.; Falk, A.; Wu, J.; Ouyang, L.; Park, H., Current-driven phase oscillation and domain-wall propagation in $W_xV_{1-x}O_2$ nanobeams. *Nano Lett* **2007,** *7*, 363-6.

35. Dicken, M. J.; Aydin, K.; Pryce, I. M.; Sweatlock, L. A.; Boyd, E. M.; Walavalkar, S.; Ma, J.; Atwater, H. A., Frequency tunable near-infrared metamaterials based on VO_2 phase transition. *Optics Express* **2009,** *17*, 18330-9.

36. Driscoll, T.; Kim, H. T.; Chae, B. G.; Di Ventra, M.; Basov, D. N., Phase-transition driven memristive system. *Appl. Phys. Lett.* **2009,** *95*.

37. Kim, B.-J.; Lee, Y. W.; Chae, B.-G.; Yun, S. J.; Oh, S.-Y.; Kim, H.-T.; Lim, Y.-S., Temperature dependence of the first-order metal-insulator transition in VO_2 and programmable critical temperature sensor. *Appl. Phys. Lett.* **2007,** *90*.

38. Strelcov, E.; Lilach, Y.; Kolmakov, A., Gas sensor based on metal-insulator transition in VO_2 nanowire thermistor. *Nano Lett* **2009,** *9*, 2322-6.

39. Hood, P. J.; Denatale, J. F., Millimeter-Wave Dielectric-Properties of Epitaxial Vanadium Dioxide Thin-Films. *J. Appl. Phys.* **1991,** *70*, 376-381.

40. Ruzmetov, D.; Zawilski, K. T.; Narayanamurti, V.; Ramanathan, S., Structure-functional property relationships in rf-sputtered vanadium dioxide thin films. *J. Appl. Phys.* **2007,** *102*, 113715.

41. Maruyama, T.; Ikuta, Y., Vanadium Dioxide Thin-Films Prepared by Chemical-Vapor-Deposition from Vanadium(III) Acetylacetonate. *Journal of Materials Science* **1993,** *28*, 5073-5078.

42. Kim, D. H.; Kwok, H. S., Pulsed laser deposition of VO_2 thin films. *Appl. Phys. Lett.* **1994,** *65*, 3188-3190.

43. Yang, Z.; Ko, C.; Ramanathan, S., Oxide Electronics Utilizing Ultrafast Metal-Insulator Transitions. *Annual Review of Materials Research* **2011,** *41*, 337-367.

44. Andersson, G., Studies on vanadium oxides. 1. Phase analysis. *Acta Chem. Scand.* **1954,** *8*, 1599-1606.

45. McWhan, D. B.; Marezio, M.; Remeika, J. P.; Dernier, P. D., X-ray diffraction study of metallic VO_2. *Phys. Rev. B.* **1974,** *10*, 490-495.

46. Oka, Y.; Sato, S.; Yao, T.; Yamamoto, N., Crystal Structures and Transition Mechanism of VO_2(A). *J. Solid State Chem.* **1998,** *141*, 594-598.

47. Popuri, S. R.; Miclau, M.; Artemenko, A.; Labrugere, C.; Villesuzanne, A.; Pollet, M., Rapid hydrothermal synthesis of VO_2 (B) and its conversion to thermochromic VO_2 (M1). *Inorg Chem* **2013,** *52*, 4780-5.

48. Hagrman, D.; Zubieta, J.; Warren, C. J.; Meyer, L. M.; Treacy, M. M.; Haushalter, R. C., A new polymorph of VO_2 prepared by soft chemical methods. *J. Solid State Chem.* **1998,** *138*, 178-182.

49. Liu, L.; Cao, F.; Yao, T.; Xu, Y.; Zhou, M.; Qu, B.; Pan, B.; Wu, C.; Wei, S.; Xie, Y., New-phase VO_2 micro/nanostructures: investigation of phase transformation and magnetic property. *New Journal of Chemistry* **2012,** *36*, 619-625.

50. Wu, C.; Hu, Z.; Wang, W.; Zhang, M.; Yang, J.; Xie, Y., Synthetic paramontroseite VO_2 with good aqueous lithium-ion battery performance. *Chemical Communications* **2008**, 3891-3.

51. Bahlawane, N.; Lenoble, D., Vanadium Oxide Compounds: Structure, Properties, and Growth from the Gas Phase. *Chem Vapor Depos* **2014,** *20*, 299-311.

52. Schwingenschlögl, U.; Eyert, V., The vanadium Magnéli phases V_nO_{2n-1}. *Ann. Phys.* **2004,** *13*, 475-510.

53. Katzke, H.; Tolédano, P.; Depmeier, W., Theory of morphotropic transformations in vanadium oxides. *Phys. Rev. B.* **2003,** *68*.

54. Lopez, R.; Boatner, L. A.; Haynes, T. E.; Feldman, L. C.; Haglund, R. F., Synthesis and characterization of size-controlled vanadium dioxide nanocrystals in a fused silica matrix. *J. Appl. Phys.* **2002,** *92*, 4031-4036.

55. Guiton, B. S.; Gu, Q.; Prieto, A. L.; Gudiksen, M. S.; Park, H., Single-crystalline vanadium dioxide nanowires with rectangular cross sections. *J. Am. Chem. Soc.* **2005,** *127*, 498-9.

56. Stewart, M. K.; Brownstead, D.; Wang, S.; West, K. G.; Ramirez, J. G.; Qazilbash, M. M.; Perkins, N. B.; Schuller, I. K.; Basov, D. N., Insulator-to-metal transition and correlated metallic state of V_2O_3 investigated by optical spectroscopy. *Phys. Rev. B* **2012,** *85*, 205113.

57. Qazilbash, M. M.; Schafgans, A. A.; Burch, K. S.; Yun, S. J.; Chae, B. G.; Kim, B. J.; Kim, H. T.; Basov, D. N., Electrodynamics of the vanadium oxides VO_2 and V_2O_3. *Phys. Rev. B* **2008,** *77*, 115121.

58. Paik, T.; Hong, S.-H.; Gaulding, E. A.; Caglayan, H.; Gordon, T. R.; Engheta, N.; Kagan, C. R.; Murray, C. B., Solution-processed phase-change VO_2 metamaterials from colloidal vanadium oxide (VO_x) nanocrystals. *ACS Nano* **2014,** *8*, 797-806.

59. Murray, C. B.; Sun, S.; Gaschler, W.; Doyle, H.; Betley, T. A.; Kagan, C. R., Colloidal synthesis of nanocrystals and nanocrystal superlattices. *IBM Journal of Research and Development* **2001,** *45*, 47-56.

60. LaMer, V. K.; Dinegar, R. H., Theory, Production and Mechanism of Formation of Monodispersed Hydrosols. *J. Am. Chem. Soc.* **1950,** *72*, 4847.

61. Thanh, N. T.; Maclean, N.; Mahiddine, S., Mechanisms of nucleation and growth of nanoparticles in solution. *Chem Rev* **2014,** *114*, 7610-30.

62. van Embden, J.; Chesman, A. S. R.; Jasieniak, J. J., The heat-up synthesis of colloidal nanocrystals. *Chem. Mater.* **2015,** *27*, 2246-2285.

63. Plummer, L. K.; Crockett, B. M.; Pennel, M. L.; Jansons, A. W.; Koskela, K. M.; Hutchison, J. E., Influence of monomer flux and temperature on morphology of indium oxide nanocrystals during a continuous growth synthesis. *Chem. Mater.* **2019,** *31*, 7638-7649.

64. Gu, H.; Soucek, M. D., Preparation and Characterization of Monodisperse Cerium Oxide Nanoparticles in Hydrocarbon Solvents. *Chem. Mater.* **2007,** *19*, 1103-1110.

65. Gordon, T. R.; Cargnello, M.; Paik, T.; Mangolini, F.; Weber, R. T.; Fornasiero, P.; Murray, C. B., Nonaqueous synthesis of TiO_2 nanocrystals using TiF_4 to engineer morphology, oxygen vacancy concentration, and photocatalytic activity. *J. Am. Chem. Soc.* **2012,** *134*, 6751-61.

66. Sun, S., Monodisperse MFe2O4 (M = Fe, Co, Mn) Nanoparticles. *J. Am. Chem. Soc.* **2004,** *126*, 273.

67. Martinez de la Torre, C.; Grossman, J. H.; Bobko, A. A.; Bennewitz, M. F., Tuning the size and composition of manganese oxide nanoparticles through varying temperature ramp and aging time. *PLOS One* **2020,** *15*, e0239034.

68. Qiao, L.; Swihart, M. T., Solution-phase synthesis of transition metal oxide nanocrystals: Morphologies, formulae, and mechanisms. *Adv Colloid Interface Sci* **2017,** *244*, 199-266.

69. Sun, S.; Zeng, H., Size-controlled synthesis of magnetite nanoparticles. *J. Am. Chem. Soc.* **2002,** *124*, 8204-5.

70. Buonsanti, R.; Grillo, V.; Carlino, E.; Giannini, C.; Kipp, T.; Cingolani, R.; Cozzoli, P. D., Nonhydrolytic synthesis of high-quality anisotropically shaped brookite TiO_2 nanocrystals. *J. Am. Chem. Soc.* **2008,** *130*, 11223-33.

71. Sun, S.; Zeng, H.; Robinson, D. B.; Raoux, S.; Rice, P. M.; Wang, S. X.; Li, G., Monodisperse MFe_2O_4 (M = Fe, Co, Mn) nanoparticles. *J. Am. Chem. Soc.* **2004,** *126*, 273-9.

72. Bergerud, A.; Buonsanti, R.; Jordan-Sweet, J. L.; Milliron, D. J., Synthesis and phase stability of metastable bixbyite V_2O_3 colloidal nanocrystals. *Chem. Mater.* **2013,** *25*, 3172-3179.

73. Owen, J., The coordination chemistry of nanocrystal surfaces. *Science* **2015,** *347*, 615-6.

74. Mourdikoudis, S.; Liz-Marzan, L. M., Oleylamine in nanoparticle synthesis. *Chem. Mater.* **2013,** *25*, 1465-1476.

75. Mourdikoudis, S.; Menelaou, M.; Fiuza-Maneiro, N.; Zheng, G.; Wei, S.; Perez-Juste, J.; Polavarapu, L.; Sofer, Z., Oleic acid/oleylamine ligand pair: a versatile combination in the synthesis of colloidal nanoparticles. *Nanoscale Horiz.* **2022,** *7*, 941-1015.

76. De Roo, J.; Zhou, Z.; Wang, J.; Deblock, L.; Crosby, A. J.; Owen, J. S.; Nonnenmann, S. S., Synthesis of phosphonic acid ligands for nanocrystal surface functionalization and solution processed memristors. *Chem. Mater.* **2018,** *30*, 8034-8039.

77. Seo, J. W.; Jun, Y. W.; Ko, S. J.; Cheon, J., In situ one-pot synthesis of 1-dimensional transition metal oxide nanocrystals. *J. Phys. Chem. B* **2005,** *109*, 5389-91.

78. Ishiwata, Y.; Shiraishi, T.; Ito, N.; Suehiro, S.; Kida, T.; Ishii, H.; Tezuka, Y.; Inagaki, Y.; Kawae, T.; Oosato, H.; Watanabe, E.; Tsuya, D.; Nantoh, M.; Ishibashi, K., Metal-insulator transition sustained by Cr-doping in V_2O_3 nanocrystals. *Appl. Phys. Lett.* **2012,** *100*, 043103.

79. Li, X.; Schaak, R. E., ZnO-templated synthesis and metal-insulator transition of VO_2 nanostructures. *Chem. Mater.* **2019,** *31*, 2088-2096.

80. Blagojevic, V. A.; Carlo, J. P.; Brus, L. E.; Steigerwald, M. L.; Uemura, Y.; Billinge, S. J. L.; Zhou, W.; Stephens, P. W.; Aczel, A. A.; Luke, G. M., Magnetic phase transition in V_2O_3 nanocrystals. *Phys. Rev. B* **2010,** *82*, 094453.

CHAPTER 2 : A VALENCE STATE-CONTROLLED SYNTHESIS OF VANADIUM OXIDE NANOCRYSTALS

2.1 Introduction

Vanadium oxides have attracted significant attention for their reversible insulator – to – metal transitions (IMTs) in the past several decades.[1] IMTs are induced at specific critical temperatures, which can additionally be triggered by pressure,[2] mechanical strain,[3] optical[4-6] and electric fields[7, 8] – and are indicative of strong electron correlations. While many promising applications[9-12] advanced in thermochromic devices, optoelectronics, and neuromorphic computing, the mechanism of IMT in these complex systems remains under debate.[13-16]

It is highly challenging to prepare vanadium oxides in a desired oxidation state. Vanadium oxides can be prepared utilizing metallurgy techniques, followed by precise post-synthesis annealing processes, both at high-temperatures and in carefully controlled oxygen pressures.[17-20] The elimination of the high-temperature annealing would facilitate the integrations of the IMT materials with electronic device elements. Particularly, IMT nanocrystals dispersible in solutions should significantly increase the processability into devices, such as conformal coating of surfaces for optical and optoelectronic applications.

Generally, in the synthesis of metal oxide nanoparticles, parameters such as the choice of precursor,[21] precursor-to-ligand ratio,[22] solvent,[23] reaction time,[24] temperature,[25] and heating rate[26-28] play important roles. It is valuable to systematically understand the roles of these parameters to establish a well-controlled synthesis.

In addition to VO_2, V_2O_3, and V_2O_5 as popularly investigated IMT materials,[29-31] there are non-stoichiometric oxides[32] known as Magnéli phase (V_nO_{2n-1}, n = 3 – 9) and Wadsley phase (V_nO_{2n+1}).[33, 34] V_3O_5 (or $V^{4+}V^{3+}{}_2O_5$) is a Magnéli phase between the stoichiometric VO_2 and V_2O_3,

and is among the three vanadium oxides that can exhibit IMT above room temperature (VO_2: T_c ~ 340 K; V_3O_5: T_c ~ 430 K; V_2O_5: T_c ~ 530 K).[35]

The success of V_3O_5 synthesis has been limited because of its narrow allowances in vanadium-to-oxygen ratio (1.666 – 1.668 ± 0.002).[36] The existence of V_3O_5 was first reported by Andersson.[37] Very recently, a previously unknown phase of V_3O_5 in anosovite structure was discovered in bulk form.[38] The physical properties of anosovite V_3O_5 remain uncharacterized due to the material rarity and the non-trivial preparation.

In this chapter, we describe a facile synthesis of pure anosovite V_3O_5 nanocrystals via the controlled reduction of a readily available V^{5+} precursor. Additionally, we identify the roles of the vanadium precursor-to-alcohol-to-ligand ratios. We show that the valence state of vanadium can be controlled straightforwardly by these parameters, unlike in typical metal oxide nanoparticle syntheses.[39] Specifically, we demonstrate formations of V_2O_3 nanocrystals ($V^{5+} \rightarrow V^{3+}$), in addition to the partial but precise reduction to V_3O_5 ($3V^{5+} \rightarrow V^{4+} + 2V^{3+}$).

2.2 Materials and Methods

Chemicals. All chemicals were used as received without any further purification. Vanadium(V) oxytrichloride (99%), toluene, hexane, ethanol, octyl ether (99%), squalene, and oleylamine (technical grade, 70%) were purchased from Sigma-Aldrich. 1-octadecanol (97%) was purchased from Alfa Aesar. Heptadecane (99%) was purchased from Sigma-Aldrich or Acros Organics.

Synthesis of Anosovite V_3O_5 nanocrystals. In a 100 mL tri-neck flask, 7.92 g 1-octadecanol, 4.2 mL oleylamine and 25.8 mL heptadecane were mixed and degassed at 125 °C for 1 h by bubbling Ar and vigorous stirring. Then, 0.4 mL of vanadium oxytrichloride was quickly injected into the reaction mixture. Immediately after the injection, the flask was opened to ambient air and

heated at a rate of 5 °C/min to 250 °C. The temperature was maintained at 250 °C for 20 min. 5 mL of crude sample was purified by adding 5 mL toluene and 40 mL ethanol, followed by centrifugation at 2500 rpm for 5 min. The light brown supernatant was discarded, and the resulting pellet was sonicated to redisperse in ethanol and centrifuged at 4000 rpm for 10 min. This step was repeated until a clear supernatant was achieved to obtain the final purified product.

Synthesis of V_2O_3 nanocrystals. The synthetic procedure is the same as the method used for V_3O_5 nanocrystals, except that 2.8 ml of oleylamine was used instead of 4.2 mL. In addition, the reaction temperature was maintained at 250 °C for 90 minutes instead of 20 min.

Characterization techniques. Transmission electron microscopy (TEM) was used to determine the size and morphology of the nanocrystals. Nanocrystals dispersed in toluene were deposited onto a 200-mesh copper grid covered with formvar carbon film and allowed to dry. Images were acquired using a JEOL-2100 microscope with a LaB_6 filament operating at 200 kV and equipped with a Gatan digital camera. The images were further analyzed using the open-source software ImageJ.

Powder X-ray diffraction (XRD) patterns were acquired using X-ray diffractometer (PANalytical X'Pert Pro/MRD) with a Cu/Kα radiation (λ=1.5418 Å) source. Phase identification and analysis were performed using the Sieve+ program in the PDF4+ software. Rietveld structure refinement was performed using the GSAS-EXPGUI package[40] on data collected at room temperature with a step size of 0.02°. Peak profiles were fitted with a pseudo-Voigt function and the background was fitted with an 8-term shifted Chebyshev polynomial.

To assess the phase stability, anosovite V_3O_5 nanocrystal samples were purified, dried under vacuum, and placed in glass vials. The samples were annealed in a muffle furnace (Nabertherm

GmbH LT 3/12/B410). For annealing in air at 170 °C and 300 °C, the samples were heated at a rate of 250 °C/h to the desired temperatures. For annealing in inert atmosphere at 500 °C, the sample was heated at a rate of 500 °C/h with 5 SLPM argon flow rate. The annealed samples were characterized with powder XRD.

ATR-FTIR spectra of the reaction intermediates were obtained with PerkinElmer Spectrum 100 FTIR with Universal ATR Sampling Accessory.

2.3 Results and Discussion

2.3.1 Formation of Anosovite V_3O_5 Nanocrystals

V_3O_5 nanocrystals were obtained in the orthorhombic anosovite-type structure for the first time. Vanadium(V) oxytrichloride ($VOCl_3$) was quickly injected ("hot injection" method)[41] into a mixture of oleylamine (OAm, 3 equiv.), 1-octadecanol (ODE, 7 equiv.), and heptadecane (HD, 19 equiv.; bp = 302 °C). The mixture was kept at 125 °C at the time of injection, then heated immediately at a rate of 5 °C/min until reaching 250 °C.

With V:OAm = 1:3, a dark brown colloidal solution was obtained, which became a highly viscous wax (due to ODE, bp = 59 °C) upon cooling to room temperature. The nanocrystals were purified, then dried in vacuum to obtain a black powder to be characterized using X-ray diffraction (XRD). The powder was stably redispersed in hexane or toluene for high-resolution transmission electron microscopy (HRTEM).

The XRD pattern and Rietveld refinement validated the anosovite phase of V_3O_5 (Figure 2.1A and Table A.1), with space group *Bbmm* and lattice parameters of a = 9.665 Å, b = 9.905 Å, c = 3.706 Å, $\beta = 90°$. The quality of the refinement was evaluated by the weighted residual error (R_{wp} = 4.50%) and goodness-of-fit indicator (χ^2 = 1.46).

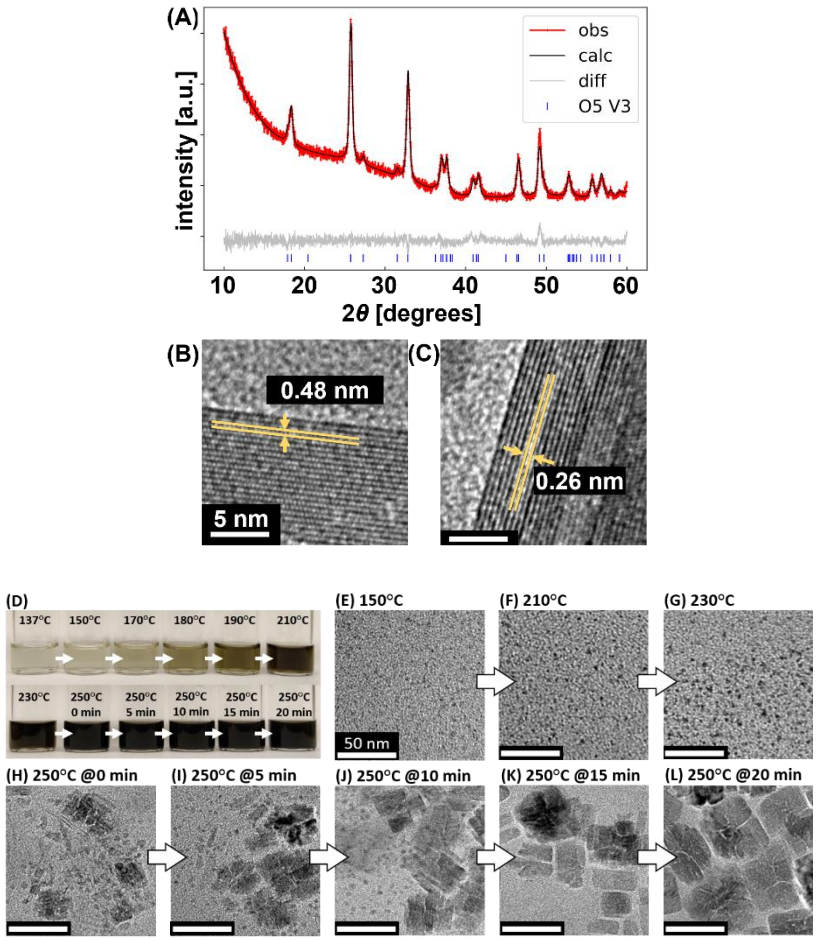

Figure 2.1. (A) XRD pattern of anosovite V_3O_5 nanocrystals. Raw data ("data") is shown with red. Fit after Rietveld refinement is shown with black line ("calc"). Gray line ("diff") is the difference between the two. Calculated peak locations are indicated by the blue marks; (B, C) HRTEM images of anosovite V_3O_5 nanocrystals showing lattice spacing of (200) and (230) planes as 0.48 and 0.26 nm, respectively. (Scale bar = 5 nm for HRTEM) (D) Evolution in the color of reaction solution heated upon $VOCl_3$ injection. (E) TEM image of the aliquot taken at 150 °C, (F) 210 °C and (G) 230 °C showing slow nucleation. (H) TEM image of the aliquot taken upon reaching 250 °C at 0 min, and (I) maintaining 250 °C at 5 min, (J) at 10 min, (K) at 15 min, and (L) 20 min, showing subsequent fast growth of nanocrystals by Ostwald Ripening. (Scale bar = 50 nm)

The calculated lattice volume for nanocrystalline anosovite V_3O_5 was 354.77×10^6 pm^3, which was slightly smaller than 357.37×10^6 pm^3 for bulk.[38] Lattice contraction in nanocrystalline metal oxides is unusual as most of them exhibit lattice expansion.[42-45] However, for anatase TiO_2 nanoparticles, lattice contraction occurs because of positive pressure due to surface hydration.[46]

Lattice contraction is also observed in bixbyite V_2O_3 nanoparticles, which is another rare crystalline phase[47] and was first reported by Milliron and co-workers.[48]

Bulk anosovite V_3O_5 was first discovered by Lerch and co-workers using $V_2F_6 \cdot 4H_2O$ as the precursor,[38] which was synthesized by reacting metallic vanadium powder with hexafluorosilicic acid.[49] We note that our nanocrystalline anosovite V_3O_5 was obtained from readily available chemicals. HRTEM images exhibited the lattice fringe spacings of 0.48 and 0.26 nm, which matched with the (200) and (230) planes of bulk anosovite V_3O_5 phase,[38] respectively (Figure 2.1B,C).

2.3.2 Kinetics of Nanocrystal Growth

Immediately following the injection of $VOCl_3$ at 125 °C, the temperature of the solution increased to 137 °C, indicating an exothermic reaction. As the temperature was ramped to 250 °C (5 °C/min), the color of the solution gradually changed from faint yellow to dark brown (Figure 2.1D). TEM images of the aliquots drawn at temperatures from 150 °C to 230 °C showed a slow nucleation process with small (~1 nm) nuclei (Figure 2.1E – G). Each aliquot was quenched immediately with a hexane:ethanol = 1:1 mixture, and the total amount drawn did not exceed 5% of the volume of the solution in order not to affect the reaction.

As the temperature reached 250 °C, larger (~25 – 50 nm) nanocrystals emerged coexisting with smaller particles. While maintaining 250 °C, the population of large plate-like nanocrystals increased and that of small particles decreased (Figure 2.1H – K), suggesting the crystal growth at the expense of smaller particles through Ostwald ripening.[50] Finally after 20 min at 250 °C, the nanocrystals reached their terminal size of ~50 nm (Figure 2.1L). No further changes were observed subsequently over 2h at 250 °C.

While controlling the nucleation step in nanocrystal syntheses helps to ensure particle monodispersity and reproducibility,[51] the difficulty may persist in practice. The precursor injection initiates a complex series of events:[51] e.g. the exo- or endothermicity of the reaction associated with injection can cause transient deviations from the desired reaction conditions. For large-scale syntheses, the temperature of the reaction mixture and the concentration of the reactants may be non-uniform until a complete mixing is achieved. Slow nucleation and delayed growth such as the one in the present system allow for a separation from the injection, thereby aid the reproducibility.

2.3.3 Effect of Precursor-to-Alcohol Ratio in Anosovite V_3O_5 Nanocrystal Formation

In non-hydrothermal syntheses of metal oxide nanoparticles, formation of metal alkoxide from the reaction between metal halide and alcohol is known as a necessary step.[52] To investigate the effects of alcohol further, V:ODE ratio was varied around 1:7, while keeping the V:OAm (precursor-to-ligand) ratio at 1:3. We confirmed that, in the absence of alcohol (ODE) in the present system, no nanocrystals formed. However, the threshold V:ODE ratio for nanocrystal formation has not been explored in the literature.

As the V:ODE ratio (ODE/V) was increased from 1 to 7, the nanoparticle size increased and attained square plate-like morphology (Figure 2.2A – D). TEM analysis indicated the nanocrystal size of 23.6 ± 6.4 nm (for V:ODE = 1:1); 20.3 ± 4.9 nm (for 1:3); 24.5 ± 6.8 nm (for 1:5); and 43.6 ± 9.6 nm (for 1:7) (Figure 2.2E). All these were pure anosovite V_3O_5 nanocrystals (Figure 2.2F), with required minimum V:ODE ratio of less than 1:1.

On the other hand, excess alcohol affected the nanocrystal formation negatively. For V:ODE ratios 1:11 and 1:15, a brown (instead of black) compound resulted upon purification, and the nanoparticle yield was poor (Figure A.1 A,B). The XRD pattern showed an intense peak at 2θ =

47.90° (indicated by *), which could not be indexed to any known vanadium compounds (Figure A.1 C). We assign this peak to a reaction intermediate between $VOCl_3$ and ODE – reaction in the absence of OAm (V:ODE:OAm = 1:7:0) resulted in a brown compound with no nanoparticles, with XRD peaks of ODE and at $2\theta = 47.90°$ (Figure A.1 D,E).

Choice of alcohol also impacted the nanocrystal formation. With $VOCl_3$: Hexadecanediol (HDD): OAm=1:3.5:3, there was no nanocrystal formation. In this case, the final product was a brown solution, and no precipitate could be obtained with toluene:ethanol = 1:10 mixture.

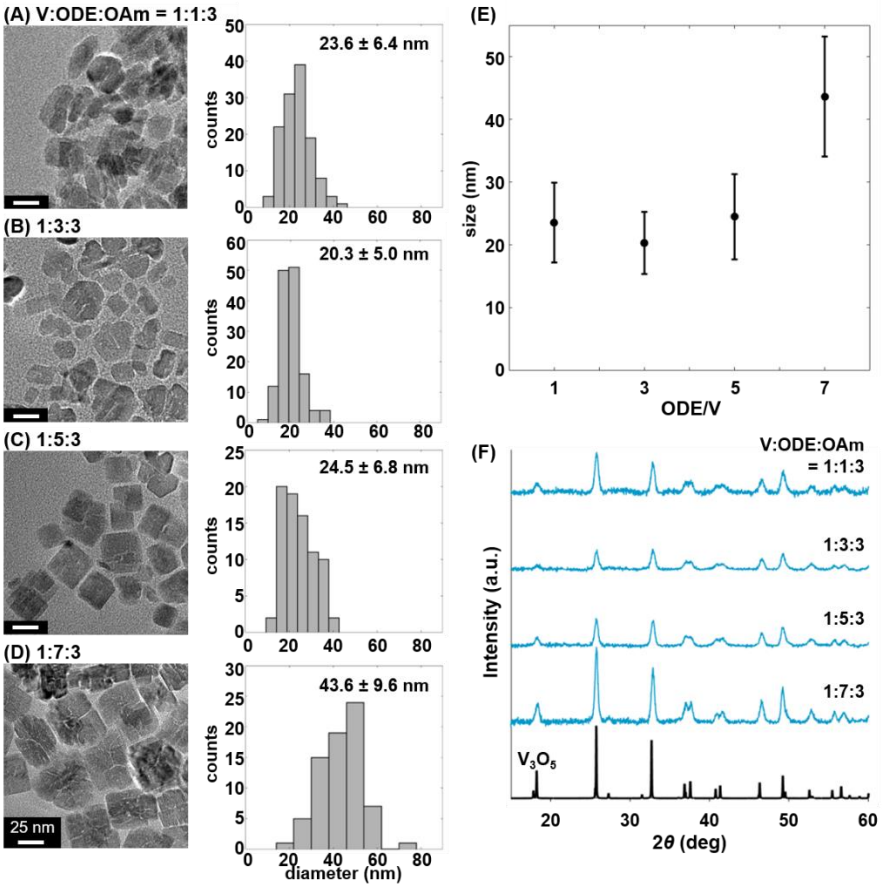

Figure 2.2. Anosovite V_3O_5 nanocrystals synthesized with V:ODE:OAm ratios of (A) 1:1:3, (B) 1:3:3, (C) 1:5:3, and (D) 1:7:3. TEM images (Scale bar = 25 nm) and histograms indicated an increase in nanocrystal size with increasing V:ODE ratios. (E) A plot of average nanocrystal size with respect to V:ODE ratios (ODE/V = 1 – 7). (F) XRD patterns confirmed pure anosovite V_3O_5 phase. (Reference spectrum: ICDD#04-019-7352)

2.3.4 Controlled Oxidation States in Anosovite V_3O_5 and Rhombohedral V_2O_3 Nanocrystal Formations

In the present system, V:OAm ratios manifested an unusually dramatic effect. Specifically, it allowed control of the vanadium oxidation states in addition to nanocrystal size and morphology (Figures 2.3).

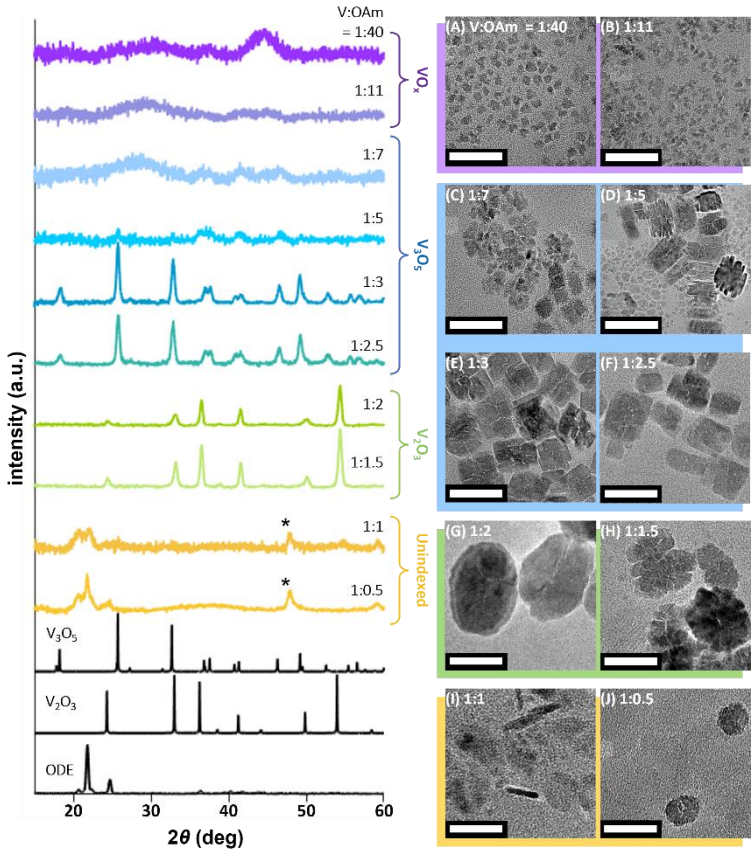

Figure 2.3. XRD patterns of nanocrystals with varied V:OAm ratios, keeping V:ODE = 7. Reference spectra: 1-octadecanol (ODE, measured), V_3O_5 (ICDD#04-019-7352), and V_2O_3 (ICDD#01-071-0280). The unindexed (reaction intermediate) peak of 2θ = 47.90° is indicated with (*). V:OAm ratios of 1:40 – 11 were amorphous VO_x; 1:7 – 2.5 were V_3O_5 nanocrystals; 1:2 – 1.5 were V_2O_3 nanocrystals; 1:1 – 0.5 comprised the unindexed peak of 2θ = 47.90° (*) and excess ODE. In terms of nanoparticle morphology, V:OAm ratio of (A) 1:40 and (B) 1:11 were sub-10 nm particles. (C) 1:7 and (D) 1:5 were mixtures of plate-like particles and smaller irregular shaped particles. (E) 1:3 and (F) 1:2.5 resulted in square plate-like particles. (G) 1:2 were ellipsoidal nanoparticles and (H) 1:1.5 yielded "nano-flower" particles. (I) 1:1 and (J) 1:0.5 had insignificant nanoparticle yield. (Scale bar = 50 nm)

Amines are known to react with metal alkoxides to produce metal oxide nanocrystals.[52] We varied the V:OAm ratio in a wide range around 1:3, while keeping V:ODE = 1:7. To keep the reaction volume constant, the amount of HD was adjusted. With V:OAm ratios of 1:40 (no HD was used) and 1:11 (HD = 11 equiv.), the products were small sub-10 nm nanoparticles (Figures 2.3 A,B and A.2). The XRD patterns showed broad low-intensity peaks (particularly the "hump" around $2\theta \sim 25 - 35°$),[53, 54] due to an amorphous structure (VO_x). These findings were consistent with the pioneering work by Murray and co-workers.[55]

For a range of V:OAm = 1:7 – 3, pure anosovite V_3O_5 nanocrystals were obtained (XRD peaks: 2θ = 18.41°, 25.75°, 27.35°, 32.87°, 37.07°, 37.69°, 41.01°, 41.55°, 46.49°, 49.21°, 52.79°, 55.75°, 56.91°, and 57.97°). For 1:7 and 1:5, XRD pattern showed low-intensity peaks, presumably due to the small size of nanocrystals.[54] We observed plate-like particles (~20 – 25 nm in size) along with irregular shaped nanoparticles for 1:7 (Figure 2.3 C), and a bimodal mixture of particles (~5 – 10 nm) and plates (~25 – 35 nm) for 1:5 (Figure 2.3 D). The ratios of 1:3 and 1:2.5 resulted in more uniform ~50 nm square plate-like nanocrystals (Figure 2.3 E,F).

When V:OAm ratio was lowered to 1:2 and 1:1.5, the nanocrystal phase dramatically transitioned to V_2O_3 (XRD peaks: 2θ = 24.43°, 33.09°, 36.39°, 38.55°, 41.43°, 44.25°, 49.99°, 54.15°, and 58.69°). For these ratios, the reaction was kept at 250 °C for 90 min to yield pure V_2O_3 nanocrystals. The morphology for these ratios were ~100 nm ellipsoids and ~50 nm flower-like, or "nano-flowers,"[56, 57] respectively (Figure 2.3 G,H).

For V:OAm ratios of 1:1 and 1:0.5, large amounts of organic impurities were present with very low nanoparticle yield (Figure 2.3 I,J). XRD showed presence of only the unreacted ODE (2θ =

20.65°, 21.77° and 24.71°) and the reaction intermediate peak of 2θ = 47.90° (*) with these insufficient amounts of OAm.

Oleylamine has been known to enable size-controlled metal oxide nanoparticle synthesis.[58, 59] However, the degree of control elucidated herein was striking – namely the precise control of oxidation state of vanadium between $V^{4+}V^{3+}{}_2O_5$ ($3V^{5+} \rightarrow V^{4+} + 2V^{3+}$) and $V^{3+}{}_2O_3$ ($V^{5+} \rightarrow V^{3+}$). To our knowledge, this is the first demonstration of oxidation state-controlled non-hydrolytic synthesis of vanadium oxide nanocrystals.

2.3.5 Phase Diagram of Vanadium Oxide Nanocrystal Formations

We additionally investigated the role of alcohol in the formation of V_2O_3 nanocrystals, by varying the V:ODE ratio around 1:7, while keeping the V:OAm ratio at 1:2 (Figure 2.4). V:ODE = 1:9 produced nano-flowers with the diameter of 41.8 ± 13.6 nm, together with large amounts of non-crystalline substances (Figure 2.4 A). The ratio of 1:7 solely produced nano-flowers of ~100±27 nm (Figure 2.4 B). The ratio of 1:5 resulted in a mixture of nano-flowers and plate-like nanocrystals with an average size of 40.9 ± 13.1 nm (Figure 2.4 C). The ratio of 1:3 yielded rod-shaped and irregular plate-like nanocrystals (Figure 2.4 D).

While XRD patterns for V:ODE = 1:9 and 1:7 were indexed to rhombohedral V_2O_3 phase, outside this parameter space resulted in the formation of V_3O_5 phase. Particularly, V_2O_3 and V_3O_5 coexisted with similar amounts for 1:5. In contrast to the V_3O_5 formations with relatively large margins in V:ODE:OAm ratios, V_2O_3 was obtained within a much smaller parameter space. The ratio of 1:9 showed an additional unindexed (reaction intermediate) peak at 2θ = 47.90° (*), which was consistently present for reactions with excess ODE (Figure A.1 C). An approximate phase diagram of the vanadium oxide nanocrystal formations is summarized in Figure 2.5.

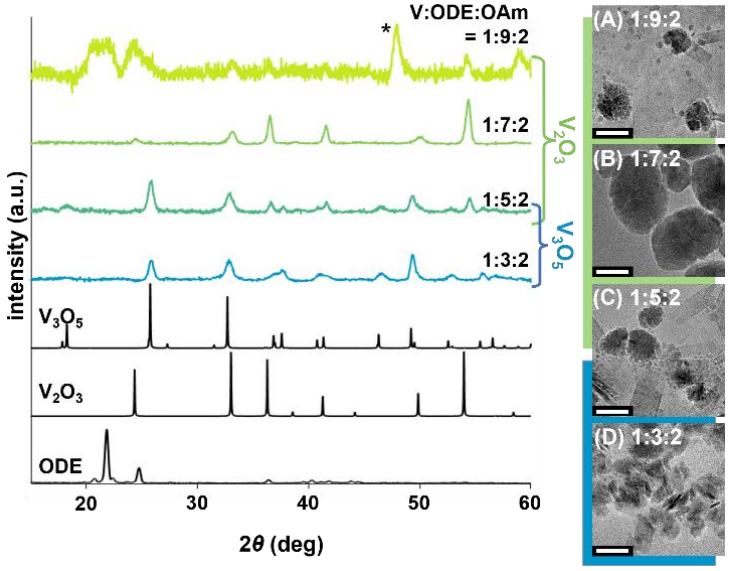

Figure 2.4. XRD patterns and TEM images (Scale bar = 50 nm) of nanocrystals synthesized with V:ODE:OAm ratios of (A) 1:9:2, (B) 1:7:2, (C) 1:5:2 and (D) 1:3:2. Reference spectra: ODE (measured), V_2O_3 (ICDD#01-071-0280) and V_3O_5 (ICDD#04-019-7352). The unindexed (reaction intermediate) peak at 2θ = 47.90° is marked with (*).

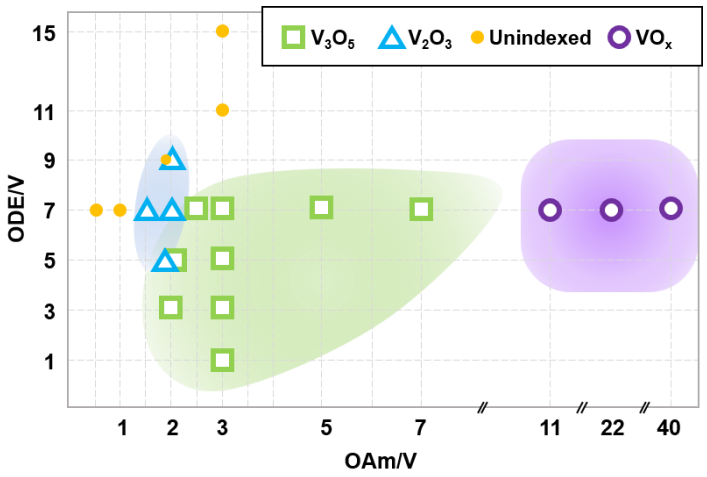

Figure 2.5. Phase diagram of vanadium oxide formations, with respect to V:ODE:OAm as the parameter and plotted for ODE/V and OAm/V.

2.3.6 Plausible Reaction Mechanisms

The first step in the present syntheses is the dissolution of the $VOCl_3$ precursor in the presence of 1-octadecanol and oleylamine. Alcohol is known to react directly with metal halide (MX) to form metal alkoxide (eq. 1).[52, 60] The metal alkoxide formed in situ further reacts with metal halide to form M−O−M bond, essential for metal oxide nanoparticle formation (eq. 2). Another reaction pathway is the aminolysis of the metal alkoxide and formation of metal hydroxyl (eq. 3),[61] followed by the formation of M−O−M bond (eq. 4). The metal hydroxyl can also condensate with the unreacted metal halide to form M−O−M bond (eq. 5). In situ formed water in eq.4 can further result in hydrolysis of the metal alkoxide.

Additionally, metal halide can react with ether to form metal alkoxide (eq. 6). This leads to the formation of M−O−M bond upon condensation with the metal halide according to (eq. 2).

Halide Elimination Pathway:

$$MX + ROH \rightarrow R–O–M + HX \quad (1)$$

$$MX + R–O–M \rightarrow M–O–M + RX \quad (2)$$

Aminolysis Pathway:

$$M–O–R + R'–NH_2 \rightarrow M–OH + R'–NH_2–R \quad (3)$$

$$M–OH + M–OH \rightarrow M–O–M + H_2O \quad (4)$$

$$MX + M–OH \rightarrow M–O–M + HX \quad (5)$$

Etherolysis Pathway:

$$MX + R–O–R \rightarrow R–O–M + RX \quad (6)$$

Regarding eq.6, using an ether as the solvent instead of heptadecane (a straight-chain alkane) indeed altered the reaction pathway. Octyl ether (bp = 292 °C) is a commonly used solvent in metal oxide nanoparticle syntheses.[62] The morphology of the resulting nanocrystals appeared unchanged, with an average size of ~50 nm for V:ODE:OAm ratio = 1:7:3 (Figure A.3 A). However, the XRD pattern showed the unindexed peak at $2\theta \sim 47.90°$ (*) in addition to pure anosovite V_3O_5 nanocrystals (Figure A.3 B). It is evidenced that the cascaded reactions through etherolysis (eq. 6) altered the kinetics of M−O−M formations. On the other hand, substitution of solvent by squalene (bp = 421 °C), which is also used in metal oxide nanoparticle syntheses,[48] resulted in a light brown product containing nanoparticles with excessive organic impurities (Figure A.3 C). The nanoparticles could not be precipitated, and further characterizations were not possible.

The reaction pathways enabling the selective formations of V_3O_5 and V_2O_3 nanocrystals can be assessed by analyzing the intermediates using Fourier transform infrared (FTIR) spectroscopy (Figure 2.6) together with time-course TEM (Figures 2.2 and A.4). Immediately after $VOCl_3$ injection, the FTIR spectra of both V:ODE:OAm=1:7:3 (V_3O_5 synthesis) and 1:7:2 (V_2O_3 synthesis) showed new peaks at ~640 cm^{-1}, ~660 cm^{-1}, ~1608 and ~1510 cm^{-1} (Figure A.5).

The peaks at ~640 cm^{-1} and ~660 cm^{-1} were present in the FT-IR spectra when $VOCl_3$ was reacted with ODE at a ratio of 1:7 (Figure A.6). These peaks were assigned to the V−OR stretching vibration of the alkoxo chloro oxovanadium compound ($VOCl_{x-y}(OR)_y$)[63-65] and the C−Cl stretching vibration of an alkyl halide byproduct[66] respectively. This indicates that when $VOCl_3$ and ODE are reacted, an alkyl halide elimination reaction takes place.[39] The peaks at ~1608 and ~1510 cm^{-1} appeared in the FTIR spectra when $VOCl_3$ was reacted with OAm at a ratio of 1:3 (Figure A.7). These peaks correspond to the amine-hydrochloride byproduct in the reaction.[67]

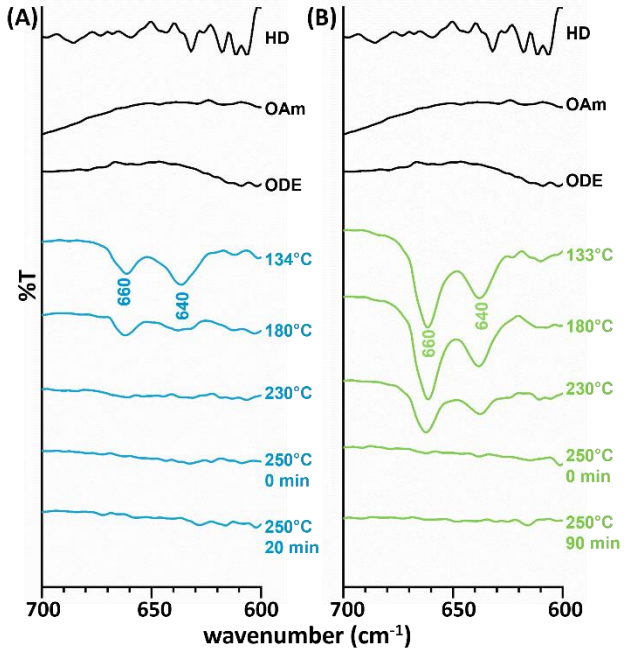

Figure 2.6. Time-course FTIR spectra comparing the reaction intermediates for V_3O_5 and V_2O_3 nanocrystal syntheses. Control spectra for heptadecane (HD), oleylamine (OAm) and 1-octadecanol (ODE) are also shown. Peaks at ~660 cm^{-1} and ~640 cm^{-1} are assigned to alkyl halide by-product and ($VOCl_{x-y}(OR)_y$) species, respectively.

The distinction between the two syntheses is that the ~640 cm^{-1} peak disappeared sooner in V_3O_5 synthesis (230 °C) than V_2O_3 synthesis (250 °C) (Figure 2.6). The reason behind this discrepancy could be a faster aminolysis of alkoxo chloro oxovanadium ($VOCl_{x-y}(OR)_y$) by excess oleylamine in V_3O_5 synthesis (V:ODE:OAm=1:7:3) compared to V_2O_3 synthesis (V:ODE:OAm=1:7:2). The byproduct of this aminolysis reaction is a secondary amine[61] which has characteristics N−H stretch peak at ~3300 cm^{-1} that overlaps with the O−H stretch of ODE.[68] The N−H bend of secondary amines[66] falls between 700 – 750 cm^{-1} which again overlaps with the in-plane O−H deformation of ODE.[69] Therefore, it is difficult to ascertain the aminolysis pathway solely from the FT-IR spectra. However, no nanocrystals formed in the absence of oleylamine, which further supports the presence of an aminolysis pathway. The TEM image of the sample did not show presence of

any nanocrystal (Figure A.8) and the corresponding XRD pattern could not be indexed to any known vanadium oxide (Figure A.1 D).

It should be noted that V−O−V stretching vibration peaks were absent in all the FTIR spectra in these studies. The reason for this could be - i) location of V−O−V peaks below 600 cm^{-1} in the spectrum.[70, 71] or ii) lower proportion of vanadium oxide in the aliquots compared to the higher concentration of organic reactants (ODE and OAm).[72]

2.3.7 Phase stability of Anosovite V_3O_5 Nanocrystals

For bulk anosovite V_3O_5, Lerch and co-workers reported:[38] (1) oxidation to pure V_2O_5 under synthetic air at 170 °C and above; (2) transformation to VO_2(R) at 280 °C in Ar atmosphere; (3) oxidization to vanadium dioxide after six weeks in ambient condition.

The phase stability of nanomaterials can be different from bulk, due to the high surface-to-volume ratio and the presence of surface ligand. Anosovite V_3O_5 nanocrystals showed superb stability against prolonged annealing in air, at 170 °C for 3h, 12h, and 24 h (Figure 2.7 A).

Annealing at 300 °C for 3h resulted in full oxidization to pure orthorhombic V_2O_5 (Figure 2.7 B), which was also indicated by the color change to yellow (Figure 2.7 C). To understand this phase transformation, we additionally evaluated the characteristics of the oleylamine ligand annealed at 170 °C, 250 °C and 300 °C. As oleylamine was heated to higher temperatures, faster evaporation took place accompanied by the color change to dark brown at 300 °C (Figure A.9). This implies the loss of ligand from the nanocrystal surfaces at 300 °C, leading to particle sintering as seen in the TEM image (Figure 2.7 D).

Upon annealing at 500 °C under Ar for 3 h, anosovite V_3O_5 nanocrystals transformed into V_2O_5 (Figure 2.7 E). However, at room temperature under Ar, the purified and dried anosovite V_3O_5

nanocrystals remained stable for more than 5 months with no phase transformation (Figure 2.7 E). The surface effects in nanomaterials can enhance the stability of metastable phases compared to bulk,[73-75] in agreement with our observations.

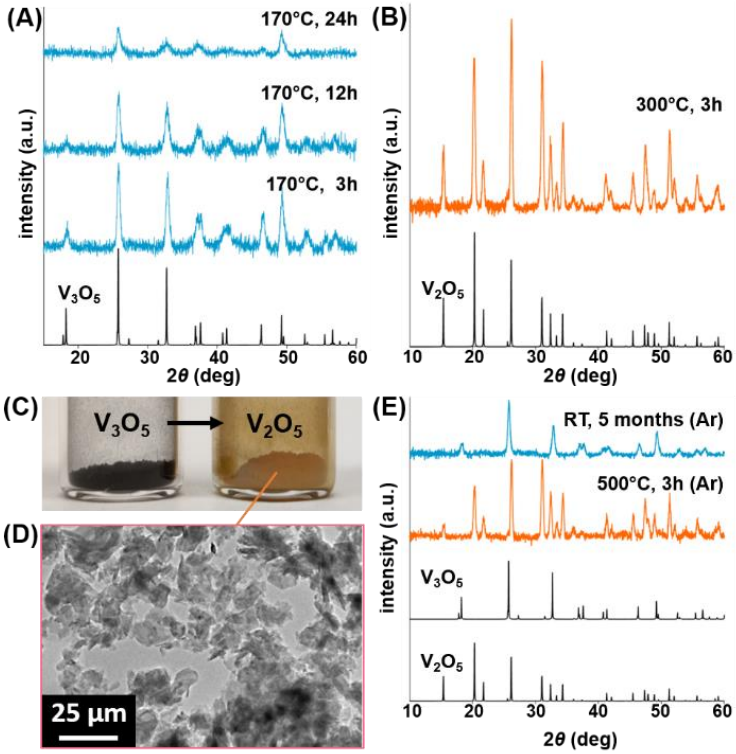

Figure 2.7. (A) Anosovite V_3O_5 nanocrystals remained stable after annealing in air at 170 °C for up to 24h. (B - D) After annealing in air at 300 °C for 3h, transformation of anosovite V_3O_5 nanocrystals (black powder) into orthorhombic V_2O_5 (yellow powder) occurred. (E) Anosovite V_3O_5 was stable under Ar for 5 months. After annealing at 500 °C under Ar, transformation into orthorhombic V_2O_5 occurred. Reference spectra: V_3O_5 (ICDD#04-019-7352) and V_2O_5 (ICDD#04-007-0398).

2.4 Conclusion

In summary, we described the synthesis of anosovite V_3O_5 nanocrystals for the first time. Furthermore, we observed the valence state-controlled formations of vanadium oxide nanocrystals by adjusting the precursor-to-alcohol-to-ligand ratios. Correlations between the V:ODE:OAm ratios and the resulting nanocrystalline phases, as well as particle sizes and morphologies, were evaluated. Anosovite V_3O_5 nanocrystals resulted from a relatively large allowance in V:ODE:OAm

= 1:[1−7]:[2−7] in the parameter space. Formation of rhombohedral V_2O_3 phase required a much narrower margin of V:ODE:OAm = 1:[7−9]:[1.5−2] in the present system. The ATR-FTIR studies of the reaction mixtures at different intervals of the syntheses indicate the presence of alkyl halide elimination and aminolysis pathway.

We highlight the controlled reductions of $3V^{5+} \rightarrow V^{4+} + 2V^{3+}$ and $V^{5+} \rightarrow V^{3+}$ in a facile manner in the present study. We think that the reductions of vanadium by cascaded form formations of alkoxide and hydroxyl species are the key intermediate processes controlling the present reaction. We speculate, in principle, that the controlled reduction of $V^{5+} \rightarrow V^{4+}$, or formation of VO_2, is possible.

It is empirically known in metal oxide nanoparticle syntheses that the temperature ramping rate significantly affects the resulting nanoparticle size and uniformity.[26-28] However, we did not investigate the effects of different ramping rates in the present study. The time course kinetics involved a fast growth via Ostwald ripening, separated from the initial slow nucleation. It is expected that the heating rate would significantly influence Ostwald ripening compared to the slower nucleation process, but further studies are needed. Halide in the precursor, for example, bromide or fluoride may alter the reaction kinetics, such as the release of structure directing agent HF when fluoride precursor is involved.[21] The facile synthesis of the nanocrystals motivates further investigation of the physical and/or optical properties of anosovite V_3O_5.

REFERENCES

1. Morin, F. J., Oxides Which Show a Metal-to-Insulator Transition at the Neel Temperature. *Phys. Rev. Lett.* **1959,** *3*, 34-36.

2. Ding, Y.; Chen, C. C.; Zeng, Q.; Kim, H. S.; Han, M. J.; Balasubramanian, M.; Gordon, R.; Li, F.; Bai, L.; Popov, D.; Heald, S. M.; Gog, T.; Mao, H. K.; van Veenendaal, M., Novel high-pressure monoclinic metallic phase of V_2O_3. *Phys. Rev. Lett.* **2014,** *112*, 056401.

3. Cao, J.; Ertekin, E.; Srinivasan, V.; Fan, W.; Huang, S.; Zheng, H.; Yim, J. W.; Khanal, D. R.; Ogletree, D. F.; Grossman, J. C.; Wu, J., Strain engineering and one-dimensional organization of metal-insulator domains in single-crystal vanadium dioxide beams. *Nat. Nanotechnol.* **2009,** *4*, 732-7.

4. Miller, C.; Triplett, M.; Lammatao, J.; Shuh, J.; Fu, D.; Wu, J.; Yu, D., Unusually long free carrier lifetime and metal-insulator band offset in vanadium dioxide. *Phys. Rev. B* **2021,** *85*, 085111.

5. Morrison, V. R.; Chatelain, R. P.; Tiwari, K. L.; Hendaoui, A.; Bruhacs, A.; Chaker, M.; Siwick, B. J., A photoinduced metal-like phase of monoclinic VO_2 revealed by ultrafast electron diffraction. *Science* **2014,** *346*, 445-8.

6. Appavoo, K.; Wang, B.; Brady, N. F.; Seo, M.; Nag, J.; Prasankumar, R. P.; Hilton, D. J.; Pantelides, S. T.; Haglund, R. F., Jr., Ultrafast phase transition via catastrophic phonon collapse driven by plasmonic hot-electron injection. *Nano Lett.* **2014,** *14*, 1127-33.

7. He, X.; Xu, J.; Xu, X.; Gu, C.; Chen, F.; Wu, B.; Wang, C.; Xing, H.; Chen, X.; Chu, J., Negative capacitance switching via VO_2 band gap engineering driven by electric field. *Appl. Phys. Lett.* **2015,** *106*, 093106.

8. Kim, H.-T.; Chae, B.-G.; Youn, D.-H.; Kim, G.; Kang, K.-Y.; Lee, S.-J.; Kim, K.; Lim, Y.-S., Raman study of electric-field-induced first-order metal-insulator transition in VO_2-based devices. *Appl. Phys. Lett.* **2005,** *86*, 242101.

9. Parkin, I. P.; Maning, T. D., Intelligent thermochromic windows. *J. Chem. Educ.* **2006,** *83*, 393-400.

10. Muster, J.; Kim, G. T.; Krstić, V.; Park, J. G.; Park, Y. W.; Roth, S.; Burghard, M., Electrical transport through individual vanadium pentoxide nanowires. *Adv. Mater.* **2000,** *12*, 420-424.

11. Yi, W.; Tsang, K. K.; Lam, S. K.; Bai, X.; Crowell, J. A.; Flores, E. A., Biological plausibility and stochasticity in scalable VO_2 active memristor neurons. *Nat. Commun.* **2018,** *9*, 4661.

12. Zhao, B.; Ravichandran, J., Low-power microwave relaxation oscillators based on phase-change oxides for neuromorphic computing. *Phys. Rev. Appl.* **2019,** *11*.

13. Shao, Z.; Cao, X.; Luo, H.; Jin, P., Recent progress in the phase-transition mechanism and modulation of vanadium dioxide materials. *NPG Asia Mater.* **2018,** *10*, 581-605.

14. Wentzcovitch, R. M.; Schulz, W. W.; Allen, P. B., VO_2: Peierls or Mott-Hubbard? A view from band theory. *Phys. Rev. Lett.* **1994,** *72*, 3389-3392.

15. Zylbersztejn, A.; Mott, N. F., Metal-insulator transition in vanadium dioxide. *Phys. Rev. B.* **1975,** *11*, 4383-4395.

16. Goodenough, J. B., The two components of the crystallographic transition in VO_2. *J. Solid State Chem.* **1971,** *3*, 490-500.

17. Ruzmetov, D.; Zawilski, K. T.; Narayanamurti, V.; Ramanathan, S., Structure-functional property relationships in RF-sputtered vanadium dioxide thin films. *J. Appl. Phys.* **2007,** *102*, 113715.

18. Guiton, B. S.; Gu, Q.; Prieto, A. L.; Gudiksen, M. S.; Park, H., Single-crystalline vanadium dioxide nanowires with rectangular cross sections. *J. Am. Chem. Soc.* **2005,** *127*, 498-9.

19. Lopez, R.; Boatner, L. A.; Haynes, T. E.; Feldman, L. C.; Haglund, R. F., Synthesis and characterization of size-controlled vanadium dioxide nanocrystals in a fused silica matrix. *J. Appl. Phys.* **2002,** *92*, 4031-4036.

20. Kim, D. H.; Kwok, H. S., Pulsed laser deposition of VO_2 thin films. *Appl. Phys. Lett.* **1994,** *65*, 3188-3190.

21. Gordon, T. R.; Cargnello, M.; Paik, T.; Mangolini, F.; Weber, R. T.; Fornasiero, P.; Murray, C. B., Nonaqueous synthesis of TiO_2 nanocrystals using TiF_4 to engineer morphology, oxygen vacancy concentration, and photocatalytic activity. *J. Am. Chem. Soc.* **2012,** *134*, 6751-61.

22. Seo, W. S.; Shim, J. H.; Oh, S. J.; Lee, E. K.; Hur, N. H.; Park, J. T., Phase- and size-controlled synthesis of hexagonal and cubic CoO nanocrystals. *J. Am. Chem. Soc.* **2005,** *127*, 6188-9.

23. Polleux, J.; Antonietti, M.; Niederberger, M., Ligand and solvent effects in the nonaqueous synthesis of highly ordered anisotropic tungsten oxide nanostructures. *J. Mater. Chem.* **2006,** *16*, 3969-3975.

24. Martinez de la Torre, C.; Grossman, J. H.; Bobko, A. A.; Bennewitz, M. F., Tuning the size and composition of manganese oxide nanoparticles through varying temperature ramp and aging time. *PLOS One* **2020,** *15*, e0239034.

25. Sun, S.; Zeng, H., Size-controlled synthesis of magnetite nanoparticles. *J. Am. Chem. Soc.* **2002,** *124*, 8204-5.

26. Lassenberger, A.; Grunewald, T. A.; van Oostrum, P. D. J.; Rennhofer, H.; Amenitsch, H.; Zirbs, R.; Lichtenegger, H. C.; Reimhult, E., Monodisperse iron oxide nanoparticles by thermal decomposition: Elucidating particle formation by second-resolved in situ small-angle X-ray scattering. *Chem. Mater.* **2017,** *29*, 4511-4522.

27. Guardia, P.; Perez-Juste, J.; Labarta, A.; Batlle, X.; Liz-Marzan, L. M., Heating rate influence on the synthesis of iron oxide nanoparticles: the case of decanoic acid. *ChemComm* **2010,** *46*, 6108-10.

28. Schladt, T. D.; Graf, T.; Tremel, W., Synthesis and characterization of monodisperse manganese oxide nanoparticles-evaluation of the nucleation and growth mechanism. *Chem. Mater.* **2009,** *21*, 3183-3190.

29. Blagojevic, V. A.; Carlo, J. P.; Brus, L. E.; Steigerwald, M. L.; Uemura, Y. J.; Billinge, S. J. L.; Zhou, W.; Stephens, P. W.; Aczel, A. A.; Luke, G. M., Magnetic phase transition in V_2O_3 nanocrystals. *Phys. Rev. B* **2010,** *82*, 094453.

30. Qazilbash, M. M.; Brehm, M.; Chae, B. G.; Ho, P. C.; Andreev, G. O.; Kim, B. J.; Yun, S. J.; Balatsky, A. V.; Maple, M. B.; Keilmann, F.; Kim, H. T.; Basov, D. N., Mott transition in VO_2 revealed by infrared spectroscopy and nano-imaging. *Science* **2007,** *318*, 1750-3.

31. Chain, E. E., Optical properties of vanadium dioxide and vanadium pentoxide thin films. *Appl. Opt.* **1991,** *30*, 2782-7.

32. Bahlawane, N.; Lenoble, D., Vanadium oxide compounds: Structure, properties, and growth from the gas phase. *Chem. Vap. Deposition* **2014,** *20*, 299-311.

33. Schwingenschlögl, U.; Eyert, V., The vanadium Magnéli phases V_nO_{2n-1}. *Ann. Phys.* **2004,** *13*, 475-510.

34. Katzke, H.; Tolédano, P.; Depmeier, W., Theory of morphotropic transformations in vanadium oxides. *Phys. Rev. B.* **2003,** *68*.

35. Rao, C. N. R.; Gopalakrishnan, J., *New Directions in Solid State Chemistry*. 2 ed.; Cambridge University Press: Cambridge, 1997.

36. Terukov, E. I.; Chudnovskii, F. A.; Reichelt, W.; Oppermann, H.; Brückner, W.; Brückner, H. P.; Moldenhauer, W., Investigation of the physical properties of V_3O_5 at phase transition with consideration of its range of homogeneity. *Phys. Status Solidi A* **1976,** *37*, 541-546.

37. Andersson, G.; Paju, J.; Lang, W.; Berndt, W., Studies on vanadium oxides. I. Phase analysis. *Acta Chem. Scand.* **1954,** *8*, 1599-1606.

38. Weber, D.; Wessel, C.; Reimann, C.; Schwickert, C.; Muller, A.; Ressler, T.; Pottgen, R.; Bredow, T.; Dronskowski, R.; Lerch, M., Anosovite-type V_3O_5: a new binary oxide of vanadium. *Inorg. Chem.* **2012,** *51*, 8524-9.

39. Niederberger, M.; Pinna, N., *Metal Oxide Nanoparticles in Organic Solvents: Synthesis, Formation, Assembly and Application*. Springer: London, 2009.

40. Toby, B. H.; Von Dreele, R. B., GSAS-II: the genesis of a modern open-source all purpose crystallography software package. *J Appl Crystallogr* **2013,** *46*, 544-549.

41. Murray, C. B.; Norris, D. J.; Bawendi, M. G., Synthesis and characterization of nearly monodisperse CdE (E = sulfur, selenium, tellurium) semiconductor nanocrystallites. *J. Am. Chem. Soc.* **2002,** *115*, 8706-8715.

42. Li, G.; Boerio-Goates, J.; Woodfield, B. F.; Li, L., Evidence of linear lattice expansion and covalency enhancement in rutile TiO_2 nanocrystals. *Appl. Phys. Lett.* **2004,** *85*, 2059-2061.

43. Tsunekawa, S.; Ishikawa, K.; Li, Z.; Kawazoe, Y.; Kasuya, A., Origin of anomalous lattice expansion in oxide nanoparticles. *Phys. Rev. Lett.* **2000,** *85*, 3440-3.

44. Ayyub, P.; Palkar, V. R.; Chattopadhyay, S.; Multani, M., Effect of crystal size reduction on lattice symmetry and cooperative properties. *Phys. Rev. B. Condens. Mater. Phys.* **1995,** *51*, 6135-6138.

45. Cimino, A.; Porta, P.; Valigi, M., Dependence of lattice parameter of magnesium oxide on crystallite size. *J. Am. Ceram. Soc.* **1966,** *49*, 152-156.

46. Li, G.; Li, L.; Boerio-Goates, J.; Woodfield, B. F., High purity anatase TiO_2 nanocrystals: near room-temperature synthesis, grain growth kinetics, and surface hydration chemistry. *J. Am. Chem. Soc.* **2005,** *127*, 8659-66.

47. Weber, D.; Stork, A.; Nakhal, S.; Wessel, C.; Reimann, C.; Hermes, W.; Muller, A.; Ressler, T.; Pottgen, R.; Bredow, T.; Dronskowski, R.; Lerch, M., Bixbyite-type V_2O_3--a metastable polymorph of vanadium sesquioxide. *Inorg. Chem.* **2011,** *50*, 6762-6.

48. Bergerud, A.; Buonsanti, R.; Jordan-Sweet, J. L.; Milliron, D. J., Synthesis and phase stability of metastable bixbyite V_2O_3 colloidal nanocrystals. *Chem. Mater.* **2013,** *25*, 3172-3179.

49. Nakhal, S.; Weber, D.; Irran, E.; Lerch, M.; Schwarz, B.; Ehrenberg, H., Synthesis, crystal structure, and magnetic properties of a new vanadium fluoride hydrate $V_2F_6.4H_2O$. *Z. Kristaloogr. -Cryst. Mater.* **2013,** *228*, 347-350.

50. Kwon, S. G.; Piao, Y.; Park, J.; Angappane, S.; Jo, Y.; Hwang, N. M.; Park, J. G.; Hyeon, T., Kinetics of monodisperse iron oxide nanocrystal formation by "heating-up" process. *J. Am. Chem. Soc.* **2007,** *129*, 12571-84.

51. Casula, M. F.; Jun, Y. W.; Zaziski, D. J.; Chan, E. M.; Corrias, A.; Alivisatos, A. P., The concept of delayed nucleation in nanocrystal growth demonstrated for the case of iron oxide nanodisks. *J. Am. Chem. Soc.* **2006,** *128*, 1675-82.

52. Deshmukh, R.; Niederberger, M., Mechanistic aspects in the formation, growth and surface functionalization of metal oxide nanoparticles in organic solvents. *Chem.–Eur. J.* **2017,** *23*, 8542-8570.

53. Cullity, B. D.; Stock, S. R., *Elements of X-Ray Diffraction*. Prentice Hall: Upper Saddle River, 2001.

54. Holder, C. F.; Schaak, R. E., Tutorial on powder x-ray diffraction for characterizing nanoscale materials. *ACS Nano* **2019,** *13*, 7359-7365.

55. Paik, T.; Hong, S. H.; Gaulding, E. A.; Caglayan, H.; Gordon, T. R.; Engheta, N.; Kagan, C. R.; Murray, C. B., Solution-processed phase-change VO_2 metamaterials from colloidal vanadium oxide (VO_x) nanocrystals. *ACS Nano* **2014,** *8*, 797-806.

56. Yin, J.; Wang, J.; Li, M.; Jin, C.; Zhang, T., Iodine Ions mediated formation of monomorphic single-crystalline platinum nanoflowers. *Chem. Mater.* **2012,** *24*, 2645-2654.

57. Narayanaswamy, A.; Xu, H.; Pradhan, N.; Kim, M.; Peng, X., Formation of nearly monodisperse In_2O_3 nanodots and oriented-attached nanoflowers: hydrolysis and alcoholysis vs pyrolysis. *J. Am. Chem. Soc.* **2006,** *128*, 10310-9.

58. Mourdikoudis, S.; Liz-Marzan, L. M., Oleylamine in nanoparticle synthesis. *Chem. Mater.* **2013,** *25*, 1465-1476.

59. Xu, Z.; Shen, C.; Hou, Y.; Gao, H.; Sun, S., Oleylamine as both reducing agent and stabilizer in a facile synthesis of magnetite nanoparticles. *Chem. Mater.* **2009,** *21*, 1778-1780.

60. Arnal, P.; Corriu, R. J. P.; Leclercq, D.; Mutin, P. H.; Vioux, A., Preparation of anatase, brookite and rutile at low temperature by non-hydrolytic sol–gel methods. *J. Mater. Chem.* **1996,** *6*, 1925-1932.

61. Liang, X.; Bai, S.; Wang, X.; Dai, X.; Gao, F.; Sun, B.; Ning, Z.; Ye, Z.; Jin, Y., Colloidal metal oxide nanocrystals as charge transporting layers for solution-processed light-emitting diodes and solar cells. *Chem. Soc. Rev.* **2017,** *46*, 1730-1759.

62. Hyeon, T.; Lee, S. S.; Park, J.; Chung, Y.; Na, H. B., Synthesis of highly crystalline and monodisperse maghemite nanocrystallites without a size-selection process. *J. Am. Chem. Soc.* **2001,** *123*, 12798-801.

63. Crans, D. C.; Chen, H.; Felty, R. A., Synthesis and reactivity of oxovanadium(V) trialkoxides of bulky and chiral alcohols. *Journal of the American Chemical Society* **1992,** *114*, 4543-4550.

64. Rosenthal, E. C.; Cui, H.; Koch, J.; Escarpa Gaede, P.; Hummert, M.; Dechert, S., Chloride-bridged oxovanadium(V) complexes with alkoxyalkoxide ligands. Synthesis, structure, electrochemistry and reactivities. *Dalton Trans* **2005**, 3108-17.

65. Miles, S. J.; Wilkins, J. D., Coordination Chemistry of Methoxydichlorooxovanadium(V). *J. Inorg. Nucl. Chem.* **1975,** *37*, 2271-2276.

66. Smith, B. C., *Infrared Spectral Interpretation: A Systematic Approach*. CRC Press: 2018.

67. Nakanishi, K.; Goto, T.; Ohashi, M., Infrared Spectra of Organic Ammonium Compounds. *B Chem Soc Jpn* **1957,** *30*, 403-408.

68. Andrushchenko, V.; Pohle, W., Influence of the hydrophobic domain on the self-assembly and hydrogen bonding of hydroxy-amphiphiles. *Phys Chem Chem Phys* **2019,** *21*, 11242-11258.

69. Gong, S.; Cheng, X.; Li, Y.; Shi, D.; Wang, X.; Zhong, H., Enhancement of ceramic foam modified hierarchical $A_{l2}O_3$@expanded graphite on thermal properties of 1-octadecanol phase change materials. *J Energy Storage* **2019,** *26*.

70. Guo, D.; Ling, C.; Wang, C.; Wang, D.; Li, J.; Zhao, Z.; Wang, Z.; Zhao, Y.; Zhang, J.; Jin, H., Hydrothermal one-step synthesis of highly dispersed m-phase VO_2 nanocrystals and application to flexible thermochromic film. *ACS Appl. Mater. Interfaces* **2018,** *10*, 28627-28634.

71. Botto, I. L.; Vassallo, M. B.; Baran, E. J.; Minelli, G., IR spectra of VO_2 and V_2O_3. *Mater. Chem. Phys.* **1997,** *50*, 267-270.

72. Buonsanti, R.; Grillo, V.; Carlino, E.; Giannini, C.; Kipp, T.; Cingolani, R.; Cozzoli, P. D., Nonhydrolytic synthesis of high-quality anisotropically shaped brookite TiO_2 nanocrystals. *J. Am. Chem. Soc.* **2008,** *130*, 11223-33.

73. Chen, C. C.; Herhold, A. B.; Johnson, C. S.; Alivisatos, A. P., Size dependence of structural metastability in semiconductor nanocrystals. *Science* **1997,** *276*, 398-401.

74. McHale, J. M.; Auroux, A.; Perrotta, A. J.; Navrotsky, A., Surface energies and thermodynamic phase stability in nanocrystalline aluminas. *Science* **1997,** *277*, 788-791.

75. Zhang, H.; Banfield, J. F., Thermodynamic analysis of phase stability of nanocrystalline titania. *J. Mater. Chem.* **1998,** *8*, 2073-2076.

CHAPTER 3 : OPTICAL PROPERTIES OF CORRELATED METALLIC V_2O_3 AND ANOSOVITE V_3O_5 NANOCRYSTAL FILMS

3.1 Introduction

Vanadium sesquioxide (V_2O_3) is widely regarded as an archetypical example of a strongly correlated electron system, which undergoes first-order phase transition from the monoclinic and antiferromagnetic insulating (AFI) state to the corundum paramagnetic metallic (PM) state at a transition temperature of ~150 K.[1] This reversible insulator – to – metal transition is accompanied by the abrupt change in resistivity of more than 7 orders of magnitude,[2] and the transition temperature can be tuned by pressure,[3] doping,[4] or photoexcitation.[5] The mechanism of IMT in these complex systems is not fully understood,[6-9] while many promising applications[10-13] have advanced. Over the past several decades, there have been extensive investigations on the bulk and thin film V_2O_3 to elucidate the physics of correlated electrons.[14-24] However, the investigations of the size dependent physical properties of nanostructured V_2O_3 have been limited.[25, 26]

Synthesis of vanadium oxides in the required composition and crystal structure is challenging due to multivalence and stable polymorphisms. Thus, the elucidated valence state- and crystal-phase-controlled preparations are highly desired. Besides the four commonly observed stoichiometric vanadium oxides (VO, V_2O_3, VO_2, and V_2O_5), there are nonstoichiometric stable oxides known as the Magnéli phase (V_nO_{2n-1}, n =3−9) and the Wadsley phase (V_nO_{2n+1}).[27, 28] V_3O_5 (or $V^{4+}V^{3+}{}_2O_5$) is obtained either in monoclinic (oxyvanite)[29] or orthorhombic (anosovite)[30] crystal structure at room temperature. The existence of anosovite bulk[30] or nanocrystalline[31] V_3O_5 has been discovered only recently because of its narrow allowances in vanadium-to-oxygen ratio[32] (1.666−1.668 ± 0.002) and higher Gibbs free energy compared to the monoclinic structure.[30] Consequently, the physical property of anosovite V_3O_5, in either bulk or nanocrystalline form, has remained unknown.

We characterized the optical properties of corundum structured V_2O_3 and anosovite V_3O_5 nanocrystals. Bulk materials have a domain structure that could affect and obscure the fundamental properties of the homogeneous material. Nanoscale materials, on the contrary, can be smaller than the characteristic domain size, allowing for the investigations of these fundamental properties. For bulk and thin film V_2O_3, dependence on the preparation methods, such as the effects of crystal mismatch and strain at substrate interface and high-temperature annealing, may pose challenges as variations in experimental data.[15, 16] Nanocrystals that are synthesized directly, without necessitating a substrate and high-temperature annealing, may alleviate some of these challenges.

Here, we obtained corundum structured V_2O_3 and anosovite V_3O_5 nanocrystals directly via a valence state-controlled synthesis and determined their optical constants. A clear difference was observed between the bulk and nanocrystalline V_2O_3 in the diffuse reflectance ensemble measurements. Spectroscopic ellipsometry[33] is a nondestructive method to determine the thickness and the optical constants of thin films and has been previously applied to films of plasmonic nanocrystals,[34, 35] semiconductor quantum dots, [36, 37] and metal oxide nanoparticles. [38, 39] We determined the complex dielectric functions, refractive indices, and optical conductivities of V_2O_3 and V_3O_5 nanocrystals as thin films by spectroscopic ellipsometry with parametrized multilayer models.

3.2 Materials and Methods

Chemicals and Materials. All chemicals were used as received without any further purification. Vanadium(V) oxytrichloride (99%), toluene, hexane, ethanol, benzyl alcohol (BnOH, anhydrous, 99.8%), V_2O_3 powder, oleylamine (OAm. technical grade, 70%) and heptadecane (HD) (99%) were purchased from Sigma-Aldrich. 1-octadecanol (ODE, 97%) was purchased from Thermo Scientific. One side polished Si wafers with SiO_2 layer were purchased from MTI Corp.

Synthesis of V_2O_3 and V_3O_5 Nanocrystals. For V_2O_3 nanocrystals, 3.1 mL of benzyl alcohol (BnOH), 4.2 mL of oleylamine (OAm), and 33 mL of heptadecane were mixed in a 100 mL tri-neck flask and degassed at 125 °C for 1 h by bubbling Ar and vigorous stirring. Then, 0.4 mL of vanadium oxytrichloride was quickly injected into the reaction mixture. The molar ratio was V:BnOH:OAm = 1:7:3. Immediately after the injection, the flask was opened to ambient air and heated at a rate of 5 °C/min to 250 °C. The temperature was maintained at 250 °C for 90 min. For V_3O_5 nanocrystals, 7.92 g of 1-octadecanol (ODE) was used in place of benzyl alcohol in the above, following a previously reported protocol,[31] with the molar ratio V:ODE:OAm = 1:7:3.

For purification of nanocrystals, 5 mL of toluene and 40 mL of ethanol was added to 5 mL of crude sample, followed by centrifugation at 4000 rpm for 5 min. The supernatant was discarded, and the resulting pellet was sonicated to redisperse in ethanol and centrifuged at 2500 rpm for 10 min. This step was repeated until a clear supernatant was achieved to obtain the final purified product.

Characterizations of Nanocrystals. Fourier transform infrared (FTIR) spectra of the reaction intermediates were obtained using a PerkinElmer Spectrum 100 FTIR with Universal ATR Sampling Accessory.

Powder X-ray diffraction (XRD) patterns were acquired using an X-ray diffractometer (PANalytical X'Pert Pro/MRD) with a Cu Kα radiation (λ = 1.5418 Å) source. Phase identification was performed using the Sieve+ program in the PDF4+ software.

Transmission electron microscopy (TEM) was used to determine the size and morphology of the nanocrystals. Nanocrystals dispersed in toluene were drop-casted onto a 200-mesh copper grid covered with formvar carbon film and allowed to dry. Images were acquired using a JEOL-2100

microscope with a LaB_6 filament operating at 200 kV and equipped with a Gatan digital camera. The images were further analyzed using the open-source software ImageJ.

To measure the thickness of individual nanocrystals, an atomic force microscope (AFM, Veeco Nanoscope IIIa) operated in tapping mode was used. The open-source software Gwyddion was used for AFM image processing.

Diffuse reflectance measurements were performed using a Shimadzu UV-3600i UV–vis–NIR spectrometer with an integrating sphere operating in the 220 – 2600 nm region at room temperature. $BaSO_4$ was used as the reference of 100% reflectance, and to dilute powder samples for all measurements. Optical absorption spectra of powders were generated by converting reflectance to absorption data using the Kubelka–Munk equation:[40] $\alpha/S = (1-R)^2/(2R)$, where R is the reflectance, and α and S are the absorption and scattering coefficients, respectively.

Sample Preparation for Ellipsometry. Commercially available Si wafers with 300 nm SiO_2 layer (SiO_2/Si) were used as substrates. Prior to the spin-coating of the nanocrystal-films, the substrates were cleaned with warm acetone for 15 min, sonicated in acetone and methanol in sequence for about 5 min each, washed under running deionized water, and dried with compressed Ar gas. 100 µL of the 40 mg/mL nanocrystal dispersion in toluene was spin-coated onto each of the 1.5 cm × 1.5 cm SiO_2/Si substrates at 1000 rpm for 90 s with 100 rpm/s initial acceleration. The deposited films were characterized using scanning electron microscopy (SEM, Raith 150, operating at either 5 or 10 keV). After completion of ellipsometry measurements, the wafer samples were cleaved to obtain cross-sectional SEM images of the nanocrystal films.

Ellipsometry and Fitting. Characterization of the bare SiO_2/Si substrate was performed first, followed by characterization of the nanocrystal film. Spectroscopic ellipsometry measures two main parameters, Ψ and Δ, which are derived from the changes in the polarization state of light as

it interacts with a sample. The change in polarization, ρ, of the s- and p-polarized components of an elliptically polarized source is commonly expressed as[33]:

$$\rho = \frac{r_{\mathrm{p}}}{r_{\mathrm{s}}} = \tan(\Psi)\, e^{i\Delta},$$

where r_{p} and r_{s} are total reflection coefficients for p- and s-polarized light. The parameters Ψ and Δ correspond to the amplitude ratio and phase difference of the reflection coefficients, respectively.

Ψ- and Δ-spectra of the nanocrystal films were obtained at room temperature on a J.A. Woollam V-VASE ellipsometer in the spectral range from 400 nm to 1700 nm with a resolution of 10 nm at three angles of incidence 65°, 70° and 75° from the surface normal. Reflectance data were described with Kramers–Kronig consistent dispersion models using J.A. Woollam WVase32 software. WVase32 software employs the iterative Levenberg-Marquardt fitting algorithm for ellipsometry data fitting. This algorithm minimizes the Mean Squared Error (MSE) by adjusting the model fitting parameters, which is defined as

$$\mathrm{MSE} = \sqrt{\frac{1}{2N - M}\sum_{i=1}^{N}\left[\left(\frac{\Psi_i^{Mod} - \Psi_i^{Exp}}{\sigma_{\Psi,i}^{Exp}}\right)^2 + \left(\frac{\Delta_i^{Mod} - \Delta_i^{Exp}}{\sigma_{\Delta,i}^{Exp}}\right)^2\right]},$$

where N is the number of Ψ and Δ pairs, M is the number of variables in the model and σ is the standard deviation for each experimental data point.

3.3 Results and Discussion

3.3.1 Valence State-controlled Synthesis of Vanadium Oxide Nanocrystals

V_2O_3 and V_3O_5 nanocrystals were obtained using benzyl alcohol and 1-octadecanol, respectively, in a modified hot injection method.[31, 41] Crude dark-brown colloidal solutions were purified and dried to obtain black powders for characterizations by X-ray diffraction (XRD). The

nanocrystals were in pure corundum structured V_2O_3 phase and pure anosovite V_3O_5 phase (Figure 3.1), respectively, without necessitating post-synthesis high-temperature annealing.

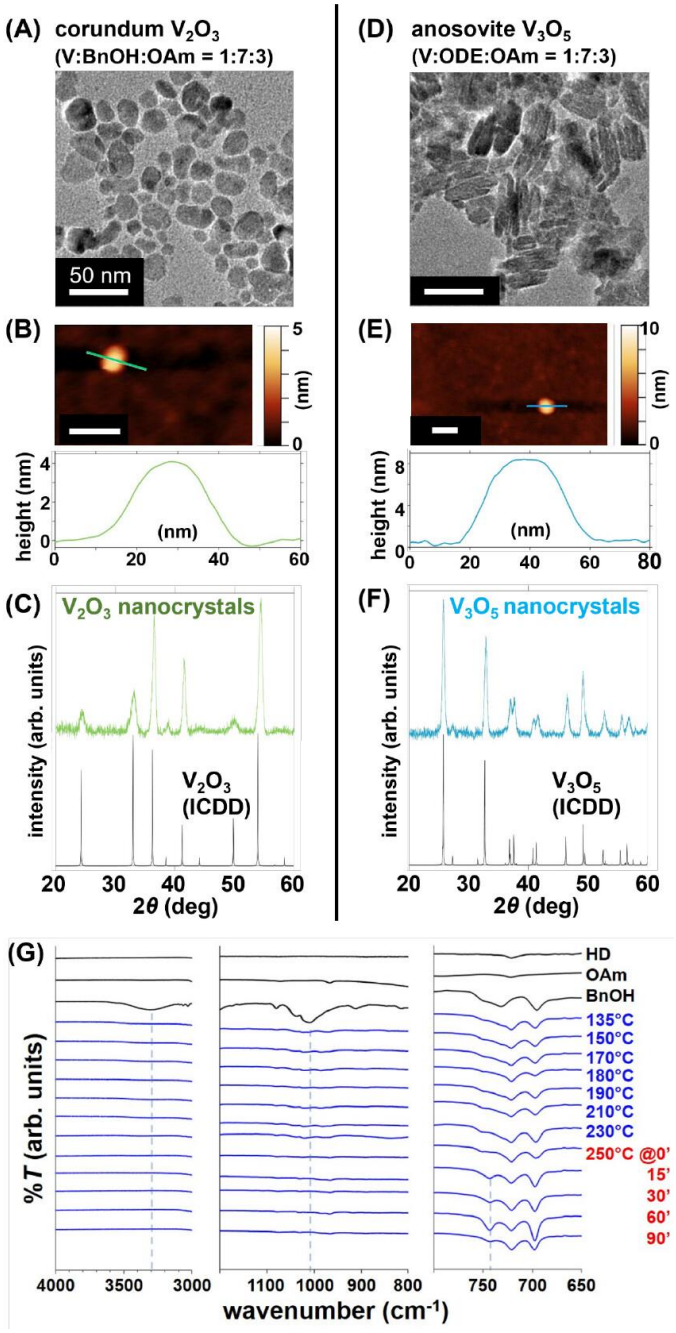

Figure 3.1. (A−C) V_2O_3 nanocrystals synthesized with a V:BnOH: OAm ratio of 1:7:3. Nanocrystal size and height were analyzed using TEM and AFM. XRD pattern indicated pure corundum crystal structure (reference spectrum: ICDD#01-071-0280). (D−F) V_3O_5 nanocrystals synthesized with a V:ODE:OAm ratio of 1:7:3. Nanocrystal size and height were analyzed using TEM and AFM. XRD pattern indicated pure anosovite crystal structure (reference spectrum: ICDD#04-019-7352). Scale bar: 50 nm. (G) Time-course FTIR spectra of the reaction intermediates for V_2O_3 nanocrystal synthesis.

Purified nanocrystals were re-dispersed in hexane or toluene to obtain transmission electron microscopy (TEM) and atomic force microscopy (AFM) images. V_2O_3 nanocrystals had an average diameter of 24.5 ± 9.0 nm by TEM measurements, and a representative thickness of ~4 nm by AFM measurements. Thus, the nanocrystals were in a plate-like morphology. Because the thickness measured by AFM includes the ligand (OAm) layers on top and bottom of the nanoplates, the thickness of the V_2O_3 nanocrystals is estimated to be ~2 nm. Similarly, V_3O_5 nanocrystals had an average diameter of 44.7 ± 7.4 nm by TEM measurements, and a representative thickness of ~8 nm by AFM measurements, with the estimated nanocrystal thickness of ~6 nm.

It is worth noting the significant difference between the syntheses with BnOH and ODE. We previously reported valence state-controlled synthesis of vanadium oxide nanocrystals using ODE, [31] in which V_2O_3 was produced at the higher ODE/V ratios (>7) and V_3O_5 at lower ratios (<5). Interestingly the observed trend in vanadium valence state was reversed by using BnOH instead of ODE.

The difference can be attributed to S_N1 reaction in the presence of an amine and benzyl alcohol.[42] "Benzyl alcohol route" for surfactant free synthesis of metal oxide nanocrystals is well studied and the reaction pathways are well understood.[43, 44] However, the reaction pathways is not well understood in the presence of amines (OAm) such as in the presented synthesis. A plausible reaction mechanism involves breakage of carbon-oxygen bond in benzyl alcohol, leading to formation of a benzyl carbocation and an –OH group. The benzyl carbocation then undergoes nucleophilic substitution with amino groups to form benzylamine. Additionally, a metal hydroxide (M–OH) species forms and co-condenses as the metal oxide. Another possibility is condensation between the metal hydroxide species and unreacted metal halide to form the metal oxide.[43]

The S_N1 reaction pathway for V_2O_3 nanocrystal formation was confirmed by analyzing the reaction intermediates using Fourier transform infrared (FTIR) spectroscopy (Figure 3.1G and B.4). Immediately after $VOCl_3$ injection, the O–H (3300 cm^{-1}) and C–O (1018 cm^{-1}) stretching vibrations of benzyl alcohol diminished (Figure B.5). As the reaction continued at 250 °C, a new peak gradually emerged at 745 cm^{-1}, which is assigned to the formation of benzylamine.[45] The control reaction without amine (V:BnOH:OAm=1:7:0) confirmed the absence of this peak (Figure B.6). On the other hand, use of aliphatic primary alcohol such as ODE favored the alkyl halide elimination and aminolysis pathways and facilitated the formation of V_3O_5 nanocrystals.[31]

3.3.2 Diffuse Reflectance Spectra of Bulk and Nanocrystalline V_2O_3

Commercial and nanocrystalline corundum structured V_2O_3 were characterized using diffuse reflectance spectroscopy at room temperature (Figure 3.2). The spectrum of bulk V_2O_3 was also measured as the control and agreed well with previous studies.[20, 46]

The UV−vis absorbance spectrum $F(R)$ was derived from the diffuse reflectance spectrum according to Kubelka−Munk equation:

$$F(R) = \alpha/S = (1-R)^2/2R,$$

where α is the absorption coefficient, S is the scattering coefficient, and R is the diffuse reflectance.[40] Bulk corundum structured V_2O_3 showed weak absorption peaks (shown in the figure as $a \sim 1.2$ eV, $b \sim 1.7$ eV) and a strong peak at $c \sim 2.4$ eV in the range of 1.0−3.0 eV, as well as a broad feature centered around $d \sim 4$ eV and an onset of absorption at $e \sim 4.9$ eV. For the nanocrystalline V_2O_3, broad absorption features were observed in the range of ∼0.6−3.0 eV and at ∼4.0−5.5 eV.

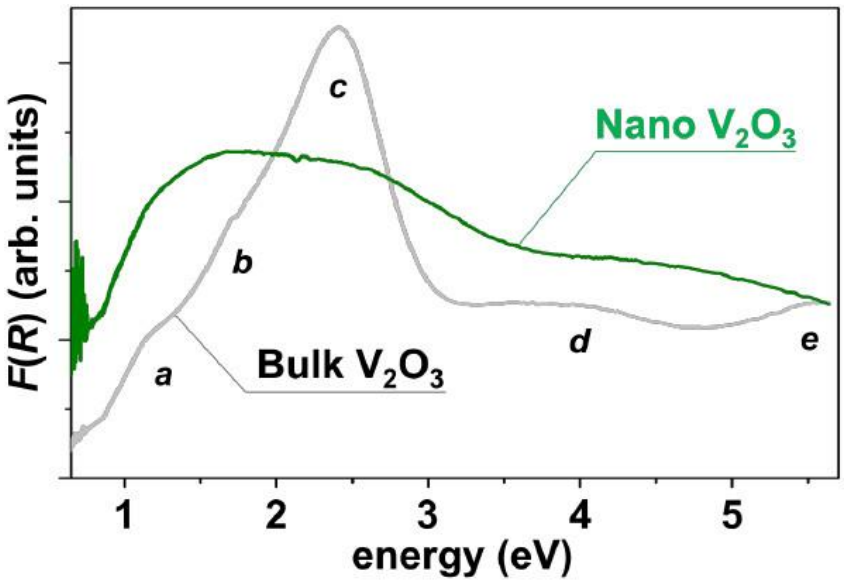

Figure 3.2. Kubelka−Munk function obtained from the diffuse reflectance spectra of bulk V_2O_3 and V_2O_3 nanocrystals, both in the corundum structure.

In bulk corundum structured V_2O_3, each V^{3+} is in $3d^2$ configuration surrounded by an oxygen octahedron, where a trigonal distortion lifts the degeneracy of t_{2g} into the e_g^{π}, a_{1g}, and e_g^{σ} orbitals. The doubly degenerate e_g^{π} orbitals extend in the crystal lattice *ab*-plane, and the nondegenerate a_{1g} orbital is along the *c*-axis. In the PM phase at room temperature,[1] the e_g^{π} and a_{1g} bands overlap and cross the Fermi level E_F, and the e_g^{σ} band is several eV above E_F. The oxygen 2*p* band is situated approximately 3.5−8.5 eV below the Fermi level.[20]

The electron−electron correlation in V_2O_3 is implemented in the single-band Hubbard model treated in mean field theory,[22, 47] which captures the essence of the system albeit omitting degeneracy. In this theory, the vanadium 3*d* band is split into the quasiparticle (QP, correlated) peak formed around E_F and the two incoherent bands called upper and lower Hubbard bands (UHB and LHB) at $E = E_F \pm U/2$, where U is the on-site Coulomb interaction in the Hubbard model. More recently, dynamical mean field theory (LDA + DMFT) calculations revealed detailed density of states for the Hubbard model, with QP/e_g^{π} (i.e., QP of e_g^{π} character), QP/a_{1g}, UHB/ e_g^{π} , UHB/a_{1g}, and LHB/e_g^{π} bands. [16,48]

For bulk V_2O_3, spectral features within the range below 3.0 eV correspond to optical transitions QP/e_g^{π} →QP/a_{1g}, LHB → QP/e_g^{π}, and QP/a_{1g} → UHB/a_{1g}. Additionally, the feature centered around 4 eV can be attributed to transitions originating from the oxygen 2*p* band, while the feature above 4.9 eV is related to transitions between LHB → UHB/e_g^{π}. [16,17]

On the contrary, V_2O_3 nanocrystals exhibited two broad absorption features, and the high energy absorption feature > 4.9 eV was absent. Presence of spontaneous uniaxial crystal lattice strain along the *c*-axis has been described in the V_2O_3 nanocrystals of ~10 nm size previously.[26] Such strain causes broadening of the a_{1g} band and enhanced mixing of the a_{1g} and e_g^{π} bands in the PM phase, which may account for the difference between bulk and nanocrystals observed here.

For highly absorptive regions of a diffuse reflectance spectrum, due to the resulting difference between the ratios of specular reflection and diffuse reflection of a sample, combined with the dependence of scattering coefficient on the particle size, the $F(R)$ deviates from the true absorption. However, the overall line shape, such as the peak positions, is still preserved.[48-50] For a sample with subwavelength size particles, the above dependence on the particle size is suppressed, and $F(R)$ becomes accurate.[51]

3.3.3 Dielectric Function and Optical Conductivity of Nanocrystalline V_2O_3

We characterized thin films of V_2O_3 nanocrystals on SiO_2/Si substrate (commercial, SiO_2 thickness of ~300 nm) using spectroscopic ellipsometry. As the control, bare SiO_2/Si substrate was characterized first. A two-layer model was used to fit the data using the known optical constants. The model fit yielded a SiO_2 thickness of 304.2 nm (Figure B.8).

For the V_2O_3 nanocrystal film, Ψ- and Δ-spectra were obtained at three angles of incidence 65°, 70° and 75°. The data were fitted to Kramers-Kronig consistent oscillator models to obtain the complex dielectric function and the thickness of the nanocrystal film. Scanning electron

microscopy (SEM) imaging was used to confirm the film thickness and uniformity after the ellipsometry measurement.

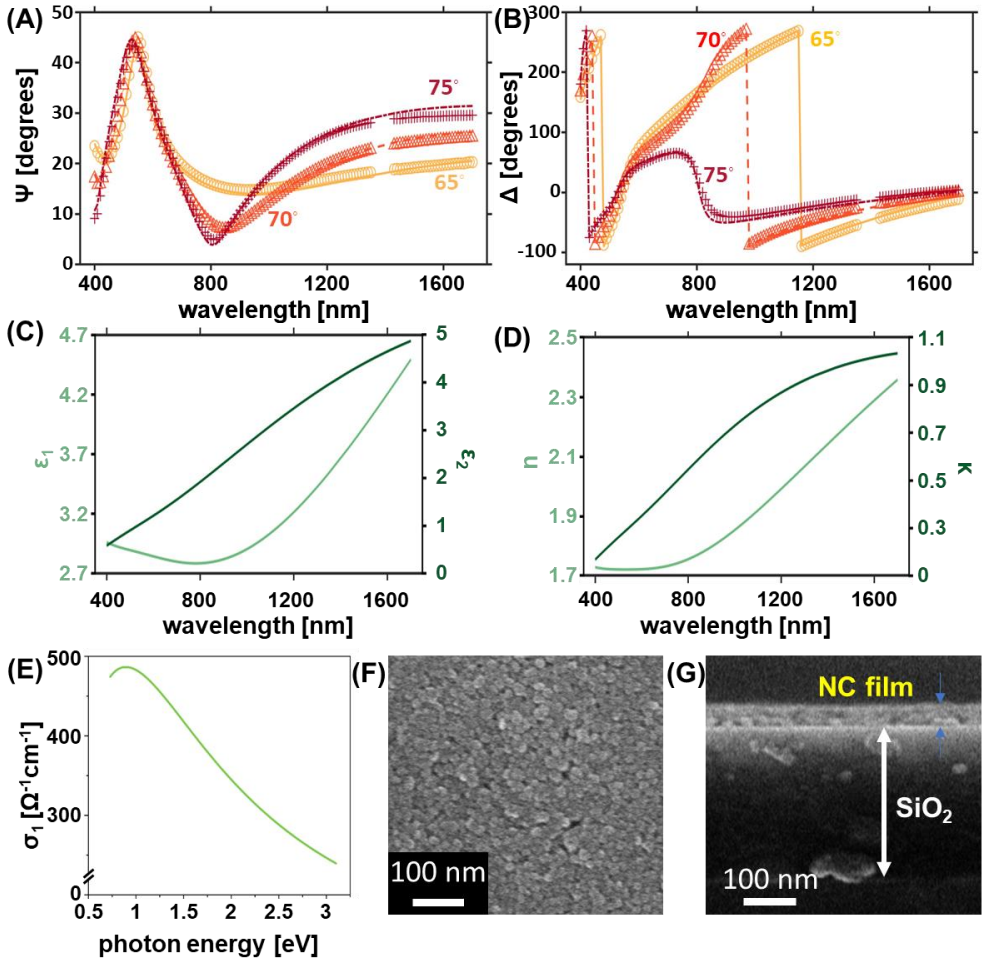

Figure 3.3. (A,B) Spectroscopic ellipsometry measurements of Ψ and Δ for the V_2O_3 nanocrystal (NC) film and the model fit based on a three-layer model comprising nanocrystal film (40.6 nm), SiO_2 layer (304.0 nm), and Si (0.5 mm). (C) Real and imaginary components of the effective complex dielectric function of the V_2O_3 nanocrystal film obtained from the fitted model. (D) Real and imaginary components of the effective complex refractive index of the V_2O_3 nanocrystal film obtained from the fitted model. (E) Real part of optical conductivity σ1 of the V_2O_3 nanocrystal film obtained from the fitted model. (F) Top view and (G) cross-sectional SEM image of V_2O_3 nanocrystals spin coated on the SiO_2/Si substrate. The nanocrystal film thickness determined from cross-sectional SEM was 43.6 ± 3.6 nm.

The spectroscopic ellipsometry data were fitted to a three-layer model consisting of a Si substrate, a SiO_2 layer, and the V_2O_3 nanocrystal film. For this, we assumed the V_2O_3 layer to be homogeneous and isotropic. Crystalline V_2O_3 has a corundum crystal structure, it is inherently anisotropic, and assuming isotropic optical constants a priori is not warranted. Nevertheless, SEM

images did not indicate a preferential orientation of the nanocrystals. Therefore, given the small size of the nanocrystals, an isotropic model is deemed adequate for determining the optical constants. The same assumption was made previously for characterizing ZnO nanoparticle film.[38]

The complex dielectric function of an absorbing film can be modeled by a combination of several Lorentz oscillators accounting for the bound electron response to the incident light.[52] Previously, V_2O_3 thin films prepared via sol-gel method[15, 16] or pulsed laser deposition[24] were modeled using combinations of Drude, Lorentzian and Tauc-Lorentzian oscillators. In case of our V_2O_3 nanocrystal film (Figure 3.3), two Lorentz oscillators were sufficient to fit the obtained Ψ- and Δ-spectra of the V_2O_3 nanocrystal film. The parameterized model dielectric function of the V_2O_3 nanocrystal film can be expressed as

$$\varepsilon = \varepsilon_1 + i\varepsilon_2 = \varepsilon_{1\,\mathrm{offset}} + \sum_{i=1}^{2} Lorentz_i(A, E_0, \Gamma),$$

where $\varepsilon_1$and ε_2 are the real and imaginary parts of the complex dielectric function respectively. The variable parameters for each Lorentz oscillator consisted of an amplitude A, resonance energy E_0, and broadening parameter Γ. Another parameter, $\varepsilon_{1\,offset}$, was introduced to provide an energy-independent contribution to ε_1 due to contributions from features outside the measured spectral range.[52] No interface or roughness layer was used in the model because it did not notably improve the quality of the fit. Instead, a thickness non-uniformity parameter was used to account for the variations in film thickness across the sample.

For this dispersion model, the resulting mean-squared error (MSE) of the standard deviation between the measured and generated reflectivity data was MSE = 12.18 (Table B.1). Additional Lorentz oscillator in the model did not significantly improve the MSE. In the present study, ellipsometry data were collected at three different angles of incidence (65, 70, and 75 deg). The

inclusion of an additional angle measurement (60 deg) did not result in a notable reduction in the MSE value (Table B.2).

Real and imaginary parts of the best-model effective dielectric function for the V_2O_3 nanocrystal film. The real part of the effective dielectric function ε_1 for the V_2O_3 nanocrystal film varied between 2.76 and 4.41 in the wavelength range of 400 – 1700 nm, with a minimum at around 780 nm. The imaginary part ε_2 varied between 0.58 and 4.88 with no major features in the line shape. The real part of the effective refractive index n varied between 1.72 and 2.36 in the wavelength range of 400 – 1700 nm, with a minimum at around 520 nm. The imaginary part κ varied between 0.17 and 1.03 with no major features.

Because of the conductivity change induced by IMT, the real part of optical conductivity has been analyzed extensively for V_2O_3 thin films in the literature.[14-24] Two distinct peaks have been reported in the ~1 – 3 eV range for the paramagnetic metallic phase, corresponding to transitions from the e_g^{π} LHB to the QP and from the QP to the a_{1g}, respectively. In contrast, the real part of the optical conductivity of V_2O_3 nanocrystal film showed a transition at ~0.92 eV.

Spectroscopic ellipsometry poses several challenges when characterizing vanadium oxide nanocrystal films. For materials with unknown optical constants, a practical approach is to employ the Cauchy or Sellmeier model to fit the film thickness using the transparent region of the ellipsometry spectra.[52-54] It is evident from the diffuse reflectance spectra that V_2O_3 nanocrystals are absorbing in the detector window (400 – 1700 nm) for the ellipsometer used in this study. Consequently, we relied on the initial thickness estimation derived from scanning electron microscopy (SEM) data to perform the ellipsometry data fitting.

Another issue is that absorbing films like vanadium oxides suffer from correlation between film thickness and the optical constants.[55] One simple method to break the correlation is the

"interference enhancement" method, where a thick dielectric layer introduced between the substrate and the absorbing film modifies the path length of light interacting with the absorbing film.[53, 56, 57] As a result, when the sample is probed at multiple angles of incidence, the measured data oscillations from the underlying dielectric film are suppressed by the absorbing film. With the knowledge of correct absorbing layer thickness and underlying dielectric layer thickness, the model can fit the measured data without strong parameter correlation. In the present study, to avoid parameter correlation, Si wafers with thick 300 nm SiO_2 layer (300 nm) were used.

Ellipsometry measurements require films to be homogenous and uniform over the illuminated area of several mm^2. The top-view SEM images confirmed a homogenous nanocrystal coverage across the substrate. The thickness of the nanocrystal film, as determined from the cross-sectional SEM image, was 43.6±3.6 nm.

It should be noted that the measured complex dielectric function ($\varepsilon_1 + i\varepsilon_2$), complex refractive index $n + i\kappa$, and real part of optical conductivity (σ_1) are those of the composite film, comprising the nanocrystals surrounded by ligands and interparticle voids. Knowledge of inorganic fill fraction and incorporation of effective medium approximation (EMA) in the optical model is required to extract the intrinsic optical constants of the nanocrystals.[36]

3.3.4 Optical Properties of Anosovite V_3O_5 Nanocrystals

The physical property of anosovite V_3O_5 has been unknown due to the rarity of the material and the lack of theoretical investigations. Here, we present the first physical characterization of this material using the nanocrystalline V_3O_5 via spectroscopic ellipsometry and diffuse reflectance spectroscopy.

Spectroscopic ellipsometry measurement for the anosovite V_3O_5 nanocrystal film is shown in Figure 3.4. One Lorentz oscillator and one gaussian oscillator were used to fit the Ψ- and Δ-spectra.

Similar to the modeling discussed above, A, E_0, Γ, as well as $\varepsilon_{1\,offset}$ were used as parameters for each Lorentz and Gaussian oscillator. Additionally, a pole oscillator was included in the model to account for the index effects due to absorption occurring at higher energies outside the spectral region being modeled.[58, 59] Pole oscillators are defined as zero width Lorentz oscillators with two variable parameters: the position (Pos) and the magnitude (Mag). The parameterized model dielectric function of the V_3O_5 nanocrystal film can be expressed as

$$\varepsilon = \varepsilon_{1\,\text{offset}} + \textit{Pole}\ (\text{Pos, Mag}) + \textit{Lorentz}\ (\text{A, E}_0, \Gamma) + \textit{Gaussian}\ (\text{A, E, }\Gamma),$$

For this dispersion model, the resulting mean-squared error between the measured and generated reflectivity data was MSE = 7.19. The thickness of the nanocrystal film derived from the model was 83.0 nm, and that of SiO_2 was 277.8 nm (Table B.3).

The real and imaginary parts of the best-model effective dielectric function for the V_3O_5 nanocrystal film are shown in figure 3.4C. The real part ε_1 in the wavelength range of 400 – 1700 nm varied between 3.21 and 3.87 with a minimum at around 650 nm, and the imaginary part ε_2 between 0.43 and 0.85 with a maximum at around 1170 nm. The real part of the effective refractive index n varied between 1.80 and 2.36, with a minimum at 620 nm. Imaginary part κ varied between 0.12 and 0.22, with a maximum at 1100 nm.

The real part of the optical conductivity σ1 of the V_3O_5 nanocrystal film at room temperature was calculated from the fitted model. We found a transition between ∼1 and 1.7 eV, accompanied by a weak transition between ∼2 and ∼3 eV.

The top-view SEM image confirmed uniform coverage over the nanocrystals over the Si wafer. Analysis of the cross-sectional SEM image of a V_3O_5 nanocrystal film indicates a thickness of 85.7 ± 2.9 nm, in good agreement with the model along with the SiO_2 thickness.

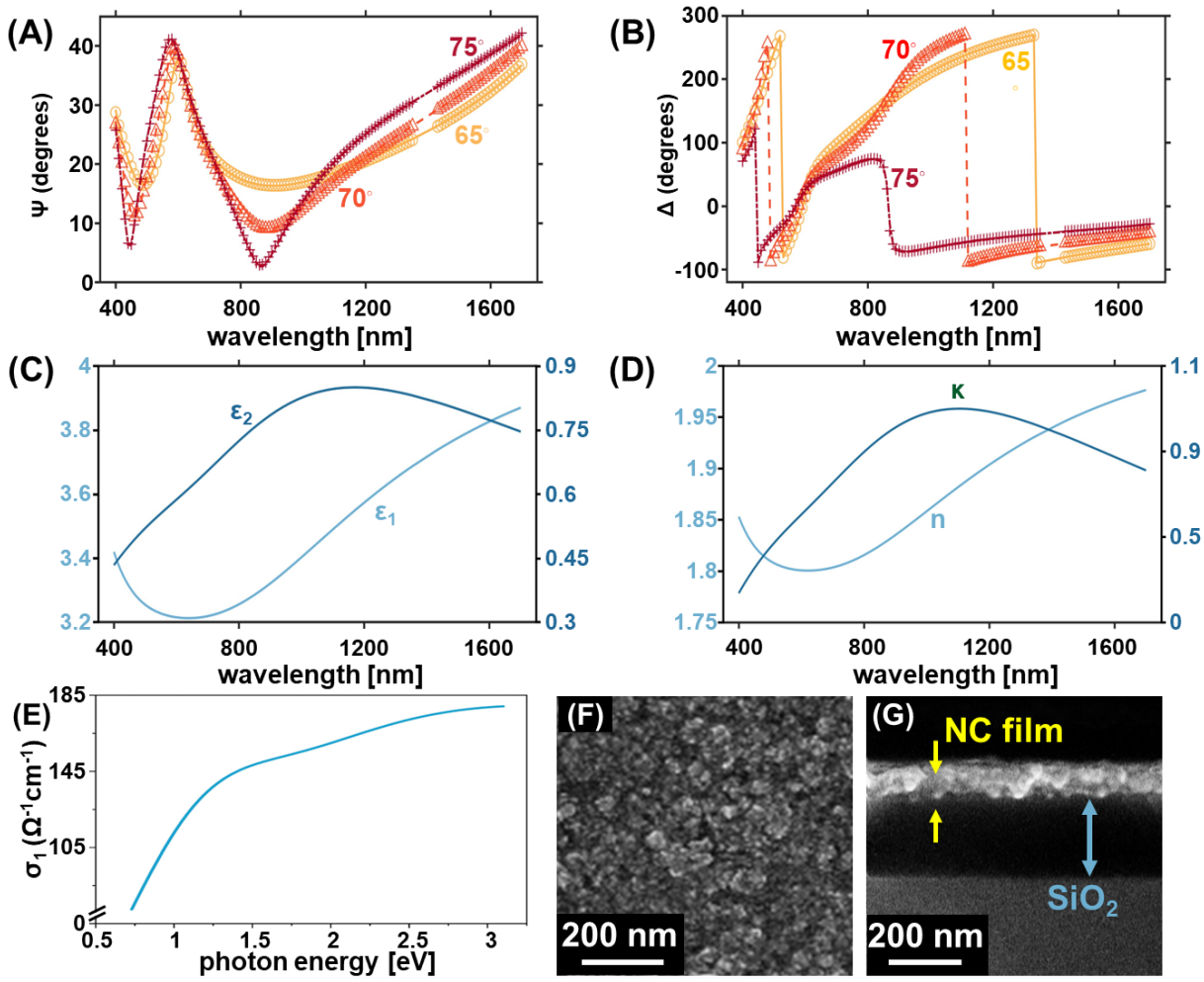

Figure 3.4. (A,B) Spectroscopic ellipsometry measurements of Ψ and Δ for the V_3O_5 nanocrystal (NC) film and the model fit based on a three-layer model comprising nanocrystal film (83.0 nm), SiO_2 layer (277.8 nm), and Si (0.5 mm). (C) Real and imaginary components of the effective complex dielectric function of the V_3O_5 nanocrystal film obtained from the fitted model. (D) Real and imaginary components of the effective complex refractive index of the V_3O_5 nanocrystal film obtained from the fitted model. (E) Real part of optical conductivity σ_1 of the V_3O_5 nanocrystal film obtained from the fitted model. (F) Top view and (G) cross-sectional SEM image of V_3O_5 nanocrystals spin coated on the SiO_2/Si substrate. The nanocrystal film thickness determined from cross-sectional SEM was 85.7 ± 2.9 nm.

In addition to ellipsometry, nanocrystalline V_3O_5 was characterized using diffuse reflectance spectroscopy (Figure 3.5). The UV−vis absorbance spectrum $F(R)$ was derived from the diffuse reflectance spectrum according to Kubelka−Munk equation:

$$F(R) = \alpha/S = (1-R)^2/2R,$$

where α is the absorption coefficient, S is the scattering coefficient, and R is the diffuse reflectance.[40] Kubelka-Munk function $F(R)$ is proportional to absorption coefficient α, and is calculated from the diffuse reflectance R. We consider Tauc equation:

$$(\alpha \cdot h\nu)^{\frac{1}{\gamma}} = A(h\nu - E_g),$$

which is then used for the band gap analysis, where h is the Planck constant, ν is the frequency, E_g is the band gap energy, A is a constant, respectively. Direct or indirect allowed band transitions correspond to $\gamma = 1/2$ or $\gamma = 2$. Here, if direct transition was assumed, the band gap energy of E_g = 2.0 eV was deduced by extrapolation of the linear region of the Tauc plot.[40] For nanocrystalline V_3O_5 this analysis yielded an absorption edge for direct allowed transition. No linear region could be extrapolated from the Tauc plot of $(F(R) \cdot h\nu)^{1/\gamma}$ and $h\nu$ assuming indirect transition with $\gamma = 2$.

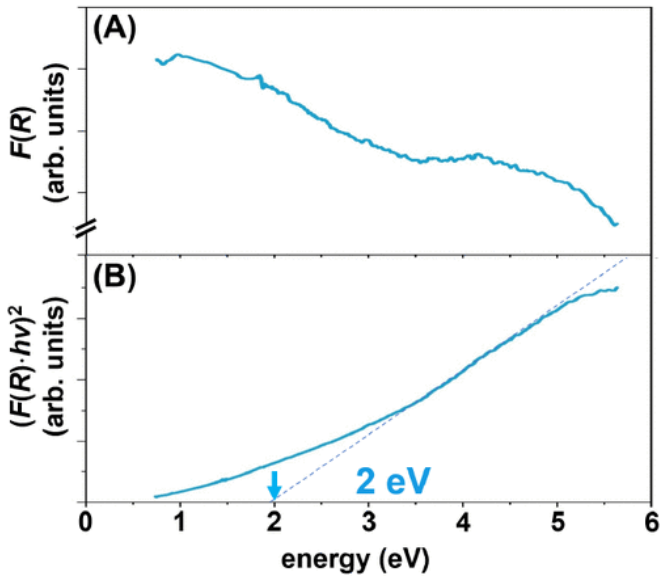

Figure 3.5. (A) Kubelka–Munk function obtained from diffuse reflectance spectra of anosovite V_3O_5 nanocrystals. (B) Tauc plot analysis for the direct allowed (γ = 1/2) transition.

3.4 Conclusion

In summary, we presented optical characterizations of pure corundum structured V_2O_3 and anosovite V_3O_5 nanocrystals that were produced selectively by a facile nonhydrothermal synthesis. The choice of alcohol dictated the precise reduction of the V^{5+} precursor and the reaction route in the selective synthesis. Vanadium oxides can be typically prepared by metallurgy techniques, followed by post-synthesis annealing at both high temperatures (~500 °C) and carefully controlled oxygen pressures. The elimination of the annealing process, such as that presented here, can reduce the variability in sample preparations.

Diffuse reflectance spectroscopy was used for the ensemble measurement of the nanocrystals, and spectroscopic ellipsometry was employed to measure the properties of the nanocrystal films including complex dielectric constants and optical conductivity. V_2O_3 nanocrystals exhibited clear deviations from the bulk electronic behavior, both in ensemble measurements and optical conductivity of the nanocrystal film. We speculate that broadening of the a_{1g} band in nanocrystalline V_2O_3 contributed to the deviation in the absorption features from those of bulk V_2O_3. The expanded range of wavelength for the optical conductivity, particularly in the low energy region, will allow analysis of the spectral weight[60] for the Drude-like behavior and a detailed comparison with the existing data.

Due to the nontriviality of preparation, anosovite V_3O_5 was discovered only recently as bulk and then as nanocrystals. We characterized the properties of anosovite V_3O_5 nanocrystals, indicating a semiconducting behavior at room temperature. For reference, another phase of V_3O_5, monoclinic oxyvanite (bulk), is known to be semiconducting at room temperature, with IMT at ~430 K.

REFERENCES

1. Imada, M.; Fujimori, A.; Tokura, Y., Metal-insulator transitions. *Rev. Mod. Phys.* **1998,** *70*, 1039-1263.

2. Rao, C. N. R.; Gopalakrishnan, J., *New Directions in Solid State Chemistry*. 1997.

3. Ding, Y.; Chen, C. C.; Zeng, Q.; Kim, H. S.; Han, M. J.; Balasubramanian, M.; Gordon, R.; Li, F.; Bai, L.; Popov, D.; Heald, S. M.; Gog, T.; Mao, H. K.; van Veenendaal, M., Novel high-pressure monoclinic metallic phase of V_2O_3. *Phys. Rev. Lett.* **2014,** *112*, 056401.

4. McWhan, D. B.; Rice, T. M.; Remeika, J. P., Mott transition in Cr-doped V_2O_3. *Phys. Rev. Lett.* **1969,** *23*, 1384-1387.

5. Liu, M. K.; Pardo, B.; Zhang, J.; Qazilbash, M. M.; Yun, S. J.; Fei, Z.; Shin, J. H.; Kim, H. T.; Basov, D. N.; Averitt, R. D., Photoinduced phase transitions by time-resolved far-infrared spectroscopy in V_2O_3. *Phys. Rev. Lett.* **2011,** *107*, 066403.

6. Goodenough, J. B., The two components of the crystallographic transition in VO_2. *J. Solid State Chem.* **1971,** *3*, 490.

7. Shao, Z.; Cao, X.; Luo, H.; Jin, P., Recent progress in the phase-transition mechanism and modulation of vanadium dioxide materials. *NPG Asia Mater.* **2018,** *10*, 581.

8. Wentzcovitch, R. M.; Schulz, W. W.; Allen, P. B., VO_2: Peierls or Mott-Hubbard? A view from band theory. *Phys. Rev. Lett.* **1994,** *72*, 3389-3392.

9. Zylbersztejn, A.; Mott, N. F., Metal-insulator transition in vanadium dioxide. *Phys. Rev. B* **1975,** *11*, 4383.

10. Parkin, I. P.; Manning, T. D., Intelligent thermochromic windows. *J. Chem. Educ.* **2006,** *83*, 393.

11. Muster, J.; Kim, G. T.; Krstić, V.; Park, J. G.; Park, Y. W.; Roth, S.; Burghard, M., Electrical transport through individual vanadium pentoxide nanowires. *Adv. Mater.* **2000,** *12*, 420.

12. Yi, W.; Tsang, K. K.; Lam, S. K.; Bai, X.; Crowell, J. A.; Flores, E. A., Biological plausibility and stochasticity in scalable VO_2 active memristor neurons. *Nat. Commun.* **2018,** *9*, 4661.

13. Zhao, B.; Ravichandran, J., Low-power microwave relaxation oscillators based on phase-change oxides for neuromorphic computing. *Phys. Rev. Appl.* **2019,** *11*, 014020.

14. Basov, D. N.; Averitt, R. D.; van der Marel, D.; Dressel, M.; Haule, K., Electrodynamics of correlated electron materials. *Rev. Mod. Phys.* **2011,** *83*, 471-541.

15. Qazilbash, M. M.; Schafgans, A. A.; Burch, K. S.; Yun, S. J.; Chae, B. G.; Kim, B. J.; Kim, H. T.; Basov, D. N., Electrodynamics of the vanadium oxides VO_2 and V_2O_3. *Phys. Rev. B* **2008,** *77*, 115121.

16. Stewart, M. K.; Brownstead, D.; Wang, S.; West, K. G.; Ramirez, J. G.; Qazilbash, M. M.; Perkins, N. B.; Schuller, I. K.; Basov, D. N., Insulator-to-metal transition and correlated metallic state of V_2O_3 investigated by optical spectroscopy. *Phys. Rev. B* **2012,** *85*, 205113.

17. Homm, P.; Menghini, M.; Seo, J. W.; Peters, S.; Locquet, J. P., Room temperature Mott metal–insulator transition in V_2O_3 compounds induced via strain-engineering. *APL Mater.* **2021,** *9*, 021116.

18. Baldassarre, L.; Perucchi, A.; Nicoletti, D.; Toschi, A.; Sangiovanni, G.; Held, K.; Capone, M.; Ortolani, M.; Malavasi, L.; Marsi, M., Quasiparticle evolution and pseudogap formation in V2O3: An infrared spectroscopy study. *Phys. Rev. B* **2008,** *77*, 113107.

19. Lo Vecchio, I.; Baldassarre, L.; D'Apuzzo, F.; Limaj, O.; Nicoletti, D.; Perucchi, A.; Fan, L.; Metcalf, P.; Marsi, M.; Lupi, S., Optical properties of V_2O_3 in its whole phase diagram. *Phys. Rev. B* **2015,** *91*, 155133.

20. Shin, S.; Suga, S.; Taniguchi, M.; Fujisawa, M.; Kanzaki, H.; Fujimori, A.; Daimon, H.; Ueda, Y.; Kosuge, K.; Kachi, S., Vacuum-ultraviolet reflectance and photoemission study of the metal-insulator phase transitions in VO_2, V_6O_{13}, and V_2O_3. *Phys. Rev. B* **1990,** *41*, 4993-5009.

21. Thomas, G. A.; Rapkine, D. H.; Carter, S. A.; Millis, A. J.; Rosenbaum, T. F.; Metcalf, P.; Honig, J. M., Observation of the gap and kinetic energy in a correlated insulator. *Phys. Rev. Lett.* **1994,** *73*, 1529-1532.

22. Rozenberg, M. J.; Kotliar, G.; Kajueter, H.; Thomas, G. A.; Rapkine, D. H.; Honig, J. M.; Metcalf, P., Optical conductivity in Mott-Hubbard systems. *Phys. Rev. Lett.* **1995,** *75*, 105-108.

23. McLeod, A. S.; van Heumen, E.; Ramirez, J. G.; Wang, S.; Saerbeck, T.; Guenon, S.; Goldflam, M.; Anderegg, L.; Kelly, P.; Mueller, A., Nanotextured phase coexistence in the correlated insulator V_2O_3. *Nat. Phys.* **2017,** *13*, 80.

24. Hu, L.; Zhao, M. L.; Liang, S.; Song, D. P.; Wei, R. H.; Tang, X. W.; Song, W. H.; Dai, J. M.; He, G.; Zhang, C. J., Exploring high-performance p-type transparent conducting oxides based on electron correlation in V_2O_3 thin films. *Phys. Rev. Appl.* **2019,** *12*, 044035.

25. Blagojevic, V. A.; Carlo, J. P.; Brus, L. E.; Steigerwald, M. L.; Uemura, Y.; Billinge, S. J. L.; Zhou, W.; Stephens, P. W.; Aczel, A. A.; Luke, G. M., Magnetic phase transition in V_2O_3 nanocrystals. *Phys. Rev. B* **2010,** *82*, 094453.

26. Ishiwata, Y.; Suehiro, S.; Kida, T.; Ishii, H.; Tezuka, Y.; Oosato, H.; Watanabe, E.; Tsuya, D.; Inagaki, Y.; Kawae, T., Spontaneous uniaxial strain and disappearance of the metal-insulator transition in monodisperse V_2O_3 nanocrystals. *Phys. Rev. B* **2012,** *86*, 035449.

27. Schwingenschlögl, U.; Eyert, V., The vanadium Magnéli phases V_nO_{2n-1}. *Ann. Phys.* **2004,** *13*, 475-510.

28. Katzke, H.; Tolédano, P.; Depmeier, W., Theory of morphotropic transformations in vanadium oxides. *Phys. Rev. B.* **2003,** *68*.

29. Andersson, G., Studies on vanadium oxides. 1. Phase analysis. *Acta Chem. Scand.* **1954,** *8*, 1599-1606.

30. Weber, D.; Wessel, C.; Reimann, C.; Schwickert, C.; Muller, A.; Ressler, T.; Pottgen, R.; Bredow, T.; Dronskowski, R.; Lerch, M., Anosovite-type V_3O_5: a new binary oxide of vanadium. *Inorg. Chem.* **2012,** *51*, 8524-8529.

31. Tarannum, M.; Heidtmann, W. P.; Dixon, J. M.; Egusa, S., Valence state-controlled synthesis of vanadium oxide nanocrystals. *J. Phys. Chem. C* **2022,** *127*, 490-498.

32. Terukov, E. I.; Chudnovskii, F. A.; Reichelt, W.; Oppermann, H.; Brückner, W.; Brückner, H. P.; Moldenhauer, W., Investigation of the physical properties of V_3O_5 at phase transition with consideration of its range of homogeneity. *Phys. Status Solidi A* **1976,** *37*, 541-546.

33. Tompkins, H. G.; McGahan, W. A., *Spectroscopic Ellipsometry and Reflectometry: A User's Guide*. 1999.

34. Fafarman, A. T.; Hong, S. H.; Caglayan, H.; Ye, X.; Diroll, B. T.; Paik, T.; Engheta, N.; Murray, C. B.; Kagan, C. R., Chemically tailored dielectric-to-metal transition for the design of metamaterials from nanoimprinted colloidal nanocrystals. *Nano Lett.* **2013,** *13*, 350-7.

35. Gordon, T. R.; Paik, T.; Klein, D. R.; Naik, G. V.; Caglayan, H.; Boltasseva, A.; Murray, C. B., Shape-dependent plasmonic response and directed self-assembly in a new semiconductor building block, indium-doped cadmium oxide (ICO). *Nano Lett* **2013,** *13*, 2857-63.

36. Diroll, B. T.; Gaulding, E. A.; Kagan, C. R.; Murray, C. B., Spectrally-resolved dielectric functions of solution-cast quantum dot thin films. *Chem. Mater.* **2015,** *27*, 6463-6469.

37. Dement, D. B.; Puri, M.; Ferry, V. E., Determining the Complex Refractive Index of Neat CdSe/CdS Quantum Dot Films. *J. Phys. Chem. C* **2018,** *122*, 21557-21568.

38. Lakhwani, G.; Roijmans, R. F. H.; Kronemeijer, A. J.; Gilot, J.; Janssen, R. A. J.; Meskers, S. C. J., Probing charge carrier density in a layer of photodoped ZnO nanoparticles by spectroscopic ellipsometry. *J. Phys. Chem. C* **2010,** *114*, 14804-14810.

39. De Trizio, L.; Buonsanti, R.; Schimpf, A. M.; Llordes, A.; Gamelin, D. R.; Simonutti, R.; Milliron, D. J., Nb-doped colloidal TiO_2 nanocrystals with tunable infrared absorption. *Chem. Mater.* **2013,** *25*, 3383-3390.

40. Makula, P.; Pacia, M.; Macyk, W., How to correctly determine the band gap energy of modified semiconductor photocatalysts based on UV-Vis spectra. *J. Phys. Chem. Lett.* **2018,** *9*, 6814-6817.

41. Paik, T.; Hong, S.-H.; Gaulding, E. A.; Caglayan, H.; Gordon, T. R.; Engheta, N.; Kagan, C. R.; Murray, C. B., Solution-processed phase-change VO_2 metamaterials from colloidal vanadium oxide (VO_x) nanocrystals. *ACS Nano* **2014,** *8*, 797-806.

42. Hu, M.; Xu, J.; Gao, J.; Yang, S.; Wong, J. S. P.; Li, R. K. Y., Benzyl alcohol-based synthesis of oxidenanoparticles: the perspective of S_N1 reaction mechanism. *Dalton Trans.* **2013,** *42*, 9777-9784.

43. Deshmukh, R.; Niederberger, M., Mechanistic aspects in the formation, growth and surface functionalization of metal oxide nanoparticles in organic solvents. *Chem.-Eur. J.* **2017,** *23*, 8542-8570.

44. Niederberger, M.; Bartl, M. H.; Stucky, G. D., Benzyl alcohol and transition metal chlorides as a versatile reaction system for the nonaqueous and low-temperature synthesis of crystalline nano-objects with controlled dimensionality. *J. Am. Chem. Soc.* **2002,** *124*, 13642-13643.

45. Smith, B. C., *Infrared Spectral Interpretation: A Systematic Approach*. CRC Press: 2018.

46. Botto, I. L.; Vassallo, M. B.; Baran, E. J.; Minelli, G., IR spectra of VO_2 and V_2O_3. *Mater. Chem. Phys.* **1997,** *50*, 267.

47. Poteryaev, A. I.; Tomczak, J. M.; Biermann, S.; Georges, A.; Lichtenstein, A. I.; Rubtsov, A. N.; Saha-Dasgupta, T.; Andersen, O. K., Enhanced crystal-field splitting and orbital-selective coherence induced by strong correlations in V_2O_3. *Phys. Rev. B* **2007,** *76*, 085127.

48. Companion, A. L.; Davis, E. N., *Developments in Applied Spectroscopy*. 1965; Vol. 4, p 221.

49. Johnson, P. D., Absolute optical absorption from diffuse reflectance. *J. Opt. Soc. Am.* **1957,** *42*, 978.

50. Boudreaux, E. A.; Englert, J. P.; Wendlandt, W. W., *Modern Aspects of Reflectance Spectroscopy*. 1968; p 47.

51. Warnken, M.; Lázárb, K.; Wark, M., Redox behaviour of SnO_2 nanoparticles encapsulated in the pores of zeolites towards reductive gas atmospheres studied by in situ diffuse reflectance UV/Vis and Mössbauer spectroscopy. *Phys. Chem. Chem. Phys.* **2001,** *3*, 1870.

52. Fujiwara, H., *Spectroscopic ellipsometry: principles and applications*. John Wiley & Sons: 2007.

53. Hilfiker, J. N.; Singh, N.; Tiwald, T.; Convey, D.; Smith, S. M.; Baker, J. H.; Tompkins, H. G., Survey of methods to characterize thin absorbing films with spectroscopic ellipsometry. *Thin Solid Films* **2008,** *516*, 7979-7989.

54. Synowicki, R. A., Spectroscopic ellipsometry characterization of indium tin oxide film microstructure and optical constants. *Thin Solid Films* **1998,** *313-314*, 394-397.

55. Sun, J.; Pribil, G. K., Analyzing optical properties of thin vanadium oxide films through semiconductor-to-metal phase transition using spectroscopic ellipsometry. *Appl. Surf. Sci.* **2017,** *421*, 819-823.

56. Hilfiker, J. N.; Linford, M. R., Using artifact minimization to model thin metallic films in spectroscopic ellipsometry. *Vac. Technol. Coat* **2022**, 28-32.

57. Hilfiker, J. N.; Linford, M. R., Using interference enhancement to increase the information content of spectroscopic ellipsometry measurements. *Vac. Technol. Coat* **2022**, 30-32.

58. *Guide to Using WVASE 32: Spectroscopic Ellipsometry Data Acquisition and Analysis Software*. J.A. Woollam Company, Incorporated: 2008.

59. Munkhbat, B.; Wrobel, P.; Antosiewicz, T. J.; Shegai, T. O., Optical constants of several multilayer transition metal dichalcogenides measured by spectroscopic ellipsometry in the 300-1700 nm range: high index, anisotropy, and hyperbolicity. *ACS Photonics* **2022,** *9*, 2398-2407.

60. Dressel, M.; Grüner, G., *Electrodynamics of Solids: Optical Properties of Electrons in Matter*. Cambridge University Press: Cambridge: 2010.

CHAPTER 4 : HEAT – UP SYNTHESIS OF VANADIUM OXIDE NANOCRYSTALS USING VANADYL ACETYLACETONATE AS THE PRECURSOR

4.1 Introduction

Up to this point, the discussion in this dissertation has focused on nanocrystals synthesized in a hot-injection method, which involves the rapid injection of precursor materials into a hot solvent.[1, 2] In this chapter, we turn our attention to an alternative synthesis technique: the heat-up method for nanocrystal synthesis. The heat-up method, also known as the non-injection or one-pot method, involves heating a mixture of precursors and solvents gradually to induce nucleation and growth of nanocrystals.[3]

Over the past decade, research in the nanocrystal field has expanded from focusing solely on the synthesis to implementation of these nanocrystals for various applications.[4] This shift, combined with the fact that most applications require large quantities of high-quality nanomaterials, has led to an increasing need to develop methods for reliable and large-scale production of these materials. Unfortunately, the well-established hot-injection method for synthesis cannot be readily scaled due to several inherent drawbacks.[3] First, the method requires rapid and homogeneous mixing of reagents at high temperatures to achieve controlled nucleation, but mixing time becomes slower and less predictable with increased batch volume. Second, the practicality of injecting large volumes becomes less viable, as typical injection volumes are around 25−50% of the mother solution volume. Finally, variability in injection times between users and batches results in small differences in initial reaction kinetics, therefore hindering the reproducibility. These factors collectively cause significant variation in reaction conditions between different batch sizes, making it difficult to reproduce high-quality nanocrystal synthesis on a large scale.

An alternative approach is the heat-up method (or "non-injection" method), which circumvents the above-mentioned drawbacks and offers a controllable and scalable synthetic route. In a heat-up method for the synthesis of metal oxide nanocrystals, a metal precursor, the stabilizing ligand, and the solvent are heated at a controlled rate to the desired reaction temperature, and held at this temperature for a specific amount of time.[3] This method has been successfully utilized for both small and large-scale syntheses of binary semiconductor nanocrystals,[5, 6] ternary and quaternary metal chalcogenide nanocrystals,[7] metallic nanocrystals[8, 9] as well as metal oxide nanocrystals.[10]

Commonly used precursors for metal oxide nanocrystal syntheses include metal alkoxides and metal halides.[11] However, these precursors suffer from notable drawbacks. The rapid reactivity of metal alkoxides often results in the formation of amorphous, non-uniform shaped particles. Metal halides, frequently used as precursors for metal oxide nanocrystals, pose challenges due to the halide impurities in the final products, which are difficult to remove.[12] Additionally, both metal alkoxides and metal halides are sensitive to moisture and air, requiring stringent handling conditions during the synthesis.

On the other hand, metal acetylacetonates offer several advantages as precursors for metal oxide nanocrystal synthesis. These compounds are relatively non-toxic and less moisture sensitive compared to many organometallic compounds, such as metal carbonyls.[13, 14] Metal acetylacetonates are coordination complexes derived from the acetylacetonate anion and metal ions.[15] The acetylacetonate ligand, abbreviated as "acac", coordinates strongly to the metal center, providing more controlled reaction rates compared to monodentate ligands in the synthesis of metal oxide nanocrystals.[16] There are a plethora of reports on the synthesis of metal oxide nanocrystals from thermal decomposition of their corresponding acetylacetonate precursor, such as, iron oxides,[10, 17] cobalt oxide,[18, 19] zinc oxide,[20] manganese oxide,[21, 22] and indium oxide.[23]

However, there has been only one report on the synthesis of vanadium oxide nanocrystals from an acetylacetonate precursor. Milliron and co-workers reported a colloidal synthesis where vanadyl acetylacetonate, oleic acid, and oleylamine in squalene were heated to yield metastable bixbyite V_2O_3 nanocrystals.[24] Synthetic conditions such as reaction temperature and duration were adjusted to regulate the size and morphology of the nanocrystals. An aminolysis reaction pathway was inferred from FTIR spectra of the reaction intermediates.

The following sections will delve into the heat-up synthesis of vanadium oxide (VO_x) nanocrystals using vanadyl (IV) acetylacetonate ($VO(acac)_2$) as the precursor in the presence of oleylamine and benzyl ether, with an analysis of the reaction pathway conducted via ATR-FTIR spectroscopy. Different seed-mediated growth techniques attempted to achieve size-control of nanocrystals will also be discussed. Effect of oleic acid/oleylamine ligand pair will be examined.

4.2 Materials and Methods

Chemicals

All chemicals were used as received without any further purification. Vanadyl(IV) acetylacetonate, toluene, hexane, ethanol, benzyl ether, octyl ether (99%), Heptadecane (HD) (99%), and oleylamine (technical grade, 70%) were purchased from Sigma-Aldrich.

Synthesis of VO_x nanocrystals

In a 100 mL tri-neck flask, 800 mg $VO(acac)_2$, 3 mL Oleylamine and 27 mL Benzyl Ether were mixed and degassed at 110 °C for 1 hour by bubbling Ar and vigorous stirring. Then, the reaction temperature was increased to 300 °C (in 20 min) under Ar. Then, the flask was opened to ambient air and the temperature was maintained at 300 °C for 60 min. 5 mL of crude sample was purified by adding 5 mL of toluene and 40 mL of ethanol, followed by centrifugation at 2500 rpm for 5

min. The light-brown supernatant was discarded, and the resulting pellet was sonicated to redisperse in ethanol and centrifuged at 4000 rpm for 10 min. This step was repeated until a clear supernatant was achieved to obtain the final purified product.

Seeded growth approach 1

Briefly, $VO(acac)_2$ (3 mmol), 3 mL oleylamine (9 mmol) and 37 mL Benzyl Ether (87 mmol) were heated to 110 °C in a 100 mL tri-neck flask. The mixture was degassed under bubbling N_2 for 1 hour at with stirring speed of 750 r.p.m. 10 mL reaction mixture was taken out of the flask with a gas tight syringe. Then the temperature was increased to 275 °C (in 30 min) under N_2, and maintained the temperature for 30 min. Then the 10 mL stock precursor solution was added back to the flask at a rate of 0.3 mL / min with the syringe pump. After that, the reaction was allowed to continue for 60 minutes.

Seeded growth approach 2

800 mg $VO(acac)_2$, 3 mL Oleylamine and 27 mL Benzyl Ether was heated to 110 °C in a 100 mL tri-neck flask. The mixture was degassed under bubbling Ar for 1 hour at 110 °C with stirring speed of 750 r.p.m. Then, previously synthesized VO_x nanocrystals (80 mg, redispersed in 4 mL Hexane) were added to the reaction mixture. The reaction mixture was degassed for 30 more minutes to evaporate hexane. Then the temperature was increased to 295 °C (in 25 min) under Ar, then opened to air and maintained the temperature for 60 min.

4.3 Results and Discussion

4.3.1 Formation of VO_x Nanocrystals

VO_x nanocrystals were prepared by thermal decomposition of vanadyl (IV) acetylacetonate as the vanadium precursor in the presence of oleylamine as a reducing agent and benzyl ether (bp =

295 °C) as the solvent. Purification of the crude reaction mixture resulted in a black powder upon drying. The powder XRD pattern of the purified nanocrystals indicated the formation of vanadium monoxide in cubic structure (Figure 4.1 A). Size analysis of the TEM images of the nanocrystals indicated particles with a diameter of 5.16 ± 1.12 nm. It is noteworthy that such small nanocrystals are expected to exhibit broad XRD patterns, preventing crystal structure identification. However, in this case, we speculate that the particles sintered during purification and sample preparation steps, resulting in discernible sharp XRD peaks.

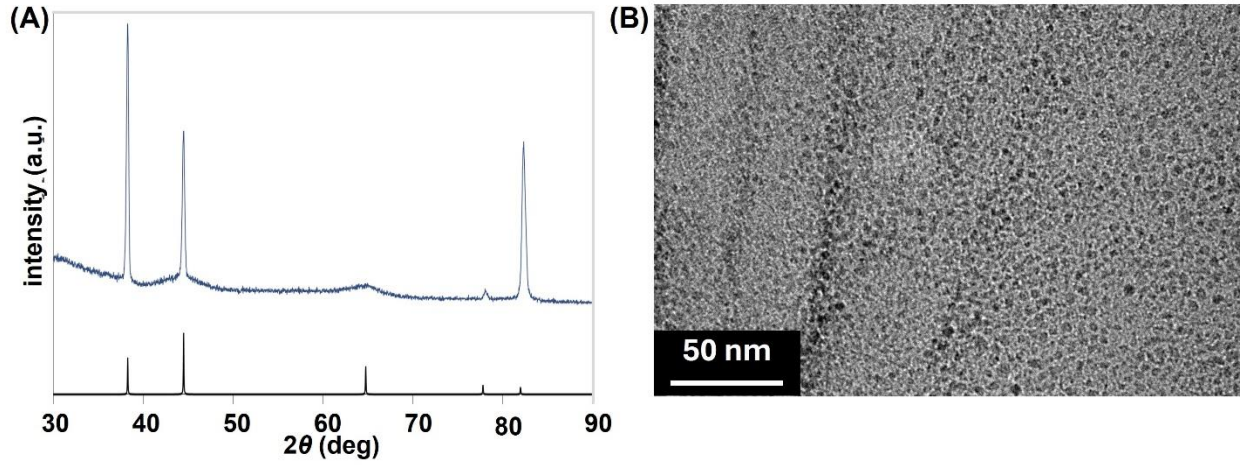

Figure 4.1. (A) XRD pattern and (B) TEM image of VO_x nanocrystals. XRD pattern of the nanocrystals confirm their crystal structure to be cubic vanadium monoxide (VO) (ICDD reference spectra #04-004-8995)

Vanadium monoxide is a highly non-stoichiometric metastable phase of vanadium oxide with a cubic crystal structure, existing in the range $VO_{0.8} - VO_{1.3}$.[25] Experimental investigations of VO_x are hindered due to challenges associated with controlling stoichiometry and the complex defect structure spread over a large composition range. Bulk VO_x typically exhibits a significant presence of both anion and cation vacancies, reaching up to 15% at x = 1.[26] These vacancies subsequently influence the resistivity and various electronic and transport properties. Interestingly, resistivity in bulk VO_x shows a varying dependence on temperature depending on the relative stoichiometry.[26]

For $x < 1$, resistivity remains relatively constant even with significant temperature changes up to 300 K.[26] However, for x values close to or greater than 1, the resistivity can change by a factor of 10^8 over the same temperature range.[26] This change, however, does not denote a phase transition but rather signifies a gradual transition from metallic to semiconducting behavior primarily governed by the variation in stoichiometry. A metal-to-semiconducting phase transition was reported at a critical temperature of 125 K,[27] although later studies suggested this transition was due to the presence of V_2O_3.[28] The VO_x nanocrystals synthesized in the present study warrants further investigation into the properties of this material in nanoscale.

4.3.2 Possible Reaction Mechanism

To understand the reaction pathway, small aliquots were taken at intermediate intervals during the synthesis and analyzed using ATR-FTIR spectroscopy (Figure 4.2). After degassing the reaction mixture for 1 hour at 110 °C, the FTIR spectra showed two peaks at 1610 and 1576 cm^{-1}. The appearance of these two peaks indicates a complex formation between vanadyl acetylacetonate ($VO(acac)_2$) and oleylamine during the degassing step in the synthesis.[24] As the reaction temperature was increased from 110 °C to 275 °C, the intensity of the peaks at 1610 and 1576 cm^{-1} decreased. Concurrently, a peak at 1646 cm^{-1} appeared which can be assigned to the C=N stretching vibration of an imine.[29, 30] We propose that oleylamine acts as a reducing agent, being oxidized to form an imine as a reaction by-product.[31] Upon analyzing the ATR-FTIR spectra of the reaction intermediates, we propose a combined solvolysis-condensation mechanism for nanocrystal formation.[30] This mechanism involves nucleophilic attack of oleylamine on one of the carbonyl groups of the metal acetylacetonate precursor, resulting in C−C bond cleavage. This process leads to the formation of an enolate ligand coordinated to the metal center. Subsequently, oleylamine undergoes nucleophilic attack on the electrophilic carbon of the enolate, resulting in

an imine and the generation of metal-hydroxyl (M−OH) species. These M−OH species further condense to form M−O−M bonds, which gives rise to the oxidic nanocrystals.

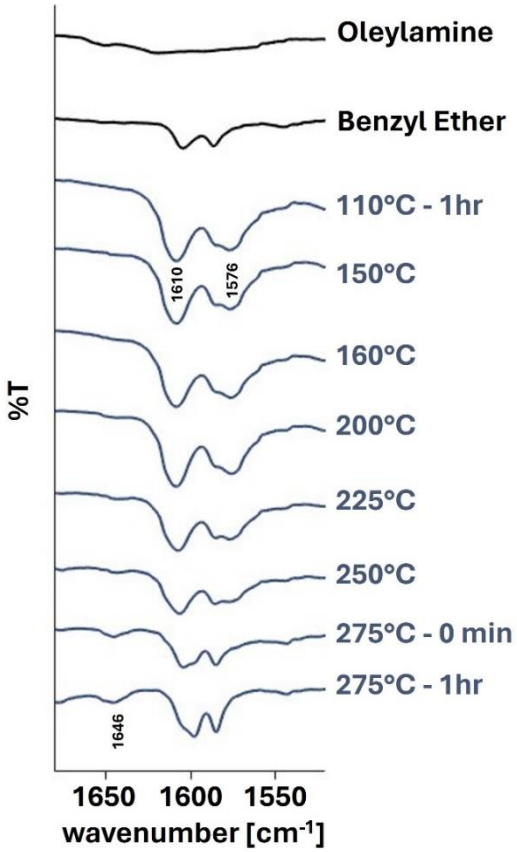

Figure 4.2. Time-course ATR-FTIR spectra of the reaction intermediates for VO_x nanocrystal synthesis. Control spectra for oleylamine (OAm) and benzyl ether (BE) are also shown. Peaks at ~1610 and ~1576 cm^{-1} are assigned to an intermediate complex formation by reacting $VO(acac)_2$ and oleylamine.

4.3.3 Assessing Nanocrystal Formation in Different Solvents

The choice of solvent plays a significant role in nanocrystal formation. For example, in chapter 3, it was demonstrated that vanadium oxide nanocrystals could be obtained in heptadecane, whereas reaction in squalene did not produce any nanocrystals.[32] Here, we assessed nanocrystal formation in solvents with high boiling points: octyl ether (bp = 292 °C) and heptadecane (bp = 302 °C) to investigate if product yields, shape, morphology or size distribution changed with different solvents. Nanocrystals formed in both solvents with similar size distribution, as observed

in the TEM images. However, due to smaller crystallite domains, their crystal structure could not be identified. The XRD pattern of VO_x nanocrystals obtained in heptadecane is shown as an example (Figure 4.3C). To obtain larger nanocrystals with discernible crystal structure indicated by sharp peaks in the XRD pattern, several approaches were followed, which are discussed in the following sections.

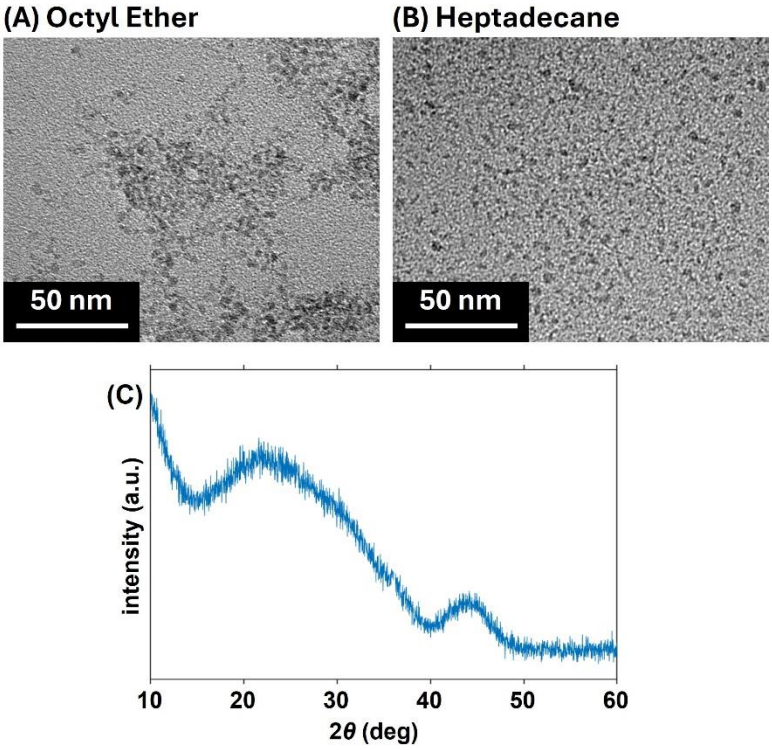

Figure 4.3. TEM image of VO_x nanocrystals synthesized in (A) octyl ether and (B) heptadecane, respectively. (C) XRD pattern of the nanocrystals synthesized in heptadecane could not be assigned to any known crystal structure of vanadium oxides.

4.3.4 Seeded Growth

In a seed-mediated growth, pre-formed nanocrystals are added into the reaction to act as nucleation sites and promote crystal growth.[33-36] In order to obtain larger nanocrystals, two approaches for seed mediated growth were attempted. However, neither method yielded the desired growth in nanocrystals.

The general methodology for synthesizing metal oxide nanocrystals via seeded growth involves preparing a precursor solution, degassing it under an inert atmosphere, heating it to a high temperature, and utilizing nanocrystal seeds to promote further growth.[10, 36] The primary differences between the two approaches attempted in this work lie in the source and handling of the seed materials. Approach 1 employed an internal seeding technique, where a portion of the reaction mixture was removed after the degassing step to be used as the stock precursor solution. The stock solution was then re-introduced into the reaction mixture after the seed nanocrystals formed at elevated temperature. The resulting nanocrystals did not attain the desired control over size as expected from seeded growth and the XRD pattern could not be indexed to any known vanadium oxide crystal structure due to broad peaks (Figure 4.4).

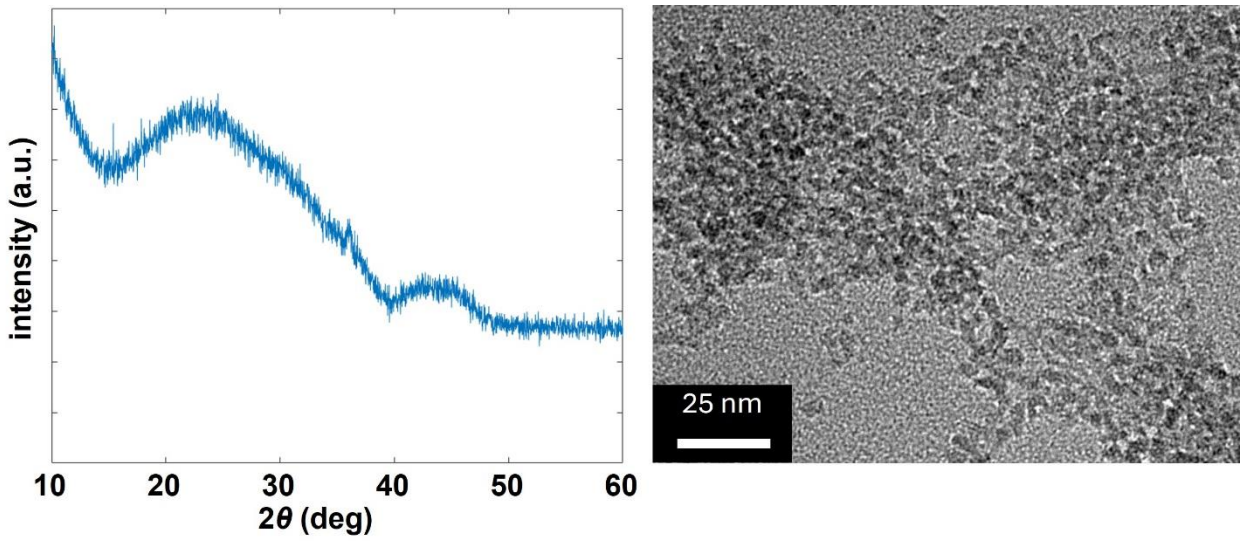

Figure 4.4. XRD pattern and TEM image of vanadium oxide nanocrystals resulted from internal seeding technique.

On the other hand, in approach 2, pre-made nanocrystal seeds were introduced into the reaction after the degassing step followed by a 60-minute reaction at elevated temperature. The TEM images of the seed nanocrystal (3.8 ± 1.12 nm) and final nanocrystal (4.55 ± 1.13 nm) obtained

from the synthesis showed very little discrepancy in the size of the resulting nanocrystals (Figure 4.5).

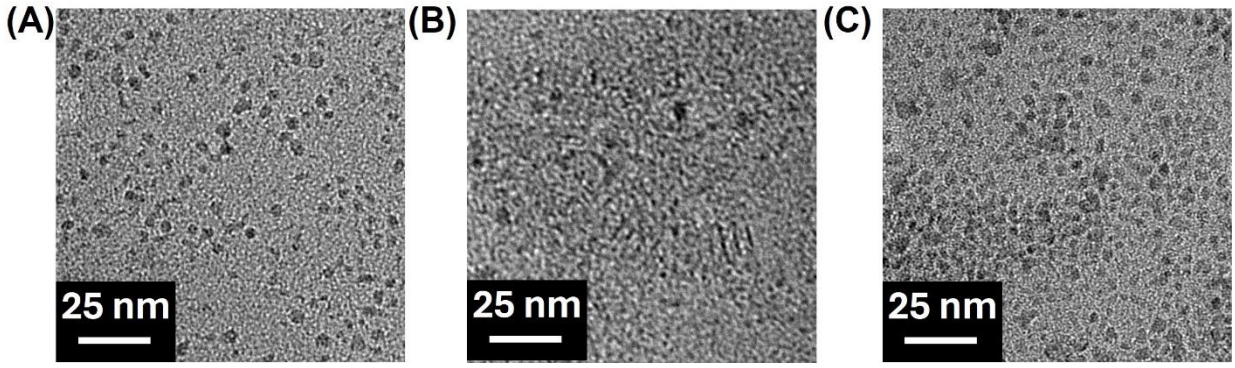

Figure 4.5. TEM images of (A) seed VO_x nanocrystals, (B) sample after addition of seed nanocrystals and degassing at 110 °C and (C) the resulting nanocrystals after reaction at 275 °C showing final size of nanocrystals remained unaffected.

4.3.5 Effect of Oleic Acid/Oleylamine Ligand Pair in the Synthesis

A common strategy to control the size and shape of nanocrystals is combined usage of oleylamine (OAm) and oleic acid (OAc) as capping agents.[37] It is known that oleylamine and oleic acid can exhibit preferential binding to different facets of the nanocrystals. This phenomenon can lead to favorable crystal growth along certain directions while blocking growth in other directions. As a result, the final size and morphology of the nanocrystals can be controlled by tuning the oleylamine/oleic acid ratio. In the present study, when nanocrystals were synthesized in the presence of oleic acid, with V:OAm:OAc=1:3:3, a mixture of small (~5 nm) spherical nanoparticles and large (~100 nm) plate-like nanocrystals were obtained. The XRD pattern showed

a broad feature indicating presence of amorphous phase superimposed with peaks corresponding to anosovite V_3O_5 phase.

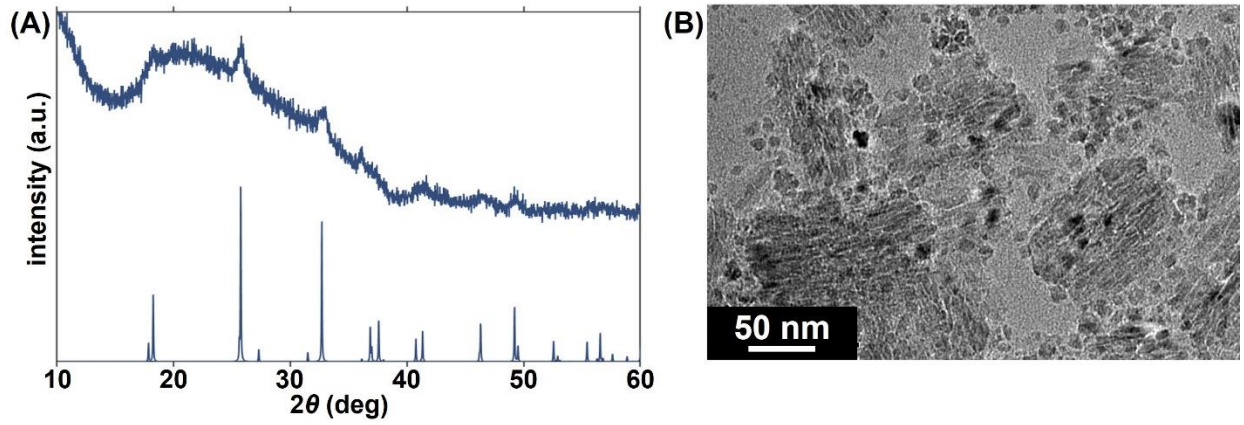

Figure 4.6. (A) XRD pattern and (B) TEM image of vanadium oxide nanocrystals synthesized with V:OAm:OAc ratio of 1:3:3. XRD peaks indicated formation of anosovite V_3O_5 (ICDD reference spectra # 04-019-7352).

4.4 Conclusion

In this chapter, a heat-up method to synthesize colloidal VOx nanocrystals was introduced. VOx nanocrystals with high size-uniformity were obtained by thermal decomposition of vanadyl acetylacetonate in the presence of oleylamine and benzyl ether. FTIR analysis of reaction intermediates indicated a complex formation between the acetylacetonate precursor and oleylamine and formation of an imine byproduct. Feasibility of other solvents such as octyl ether and heptadecane was also explored. Seed mediated growth was attempted to obtain nanocrystals with discernible crystal structure. However, the attempts were unsuccessful.

In a previous study, Milliron and coworkers reported synthesis of bixbyite V_2O_3 nanocrystals via thermal decomposition of $VO(acac)_2$ in the presence of oleylamine, oleic acid and squalene.[24] They speculated that oleylamine reduced the vanadium oxidation state from +4 in the precursor ($VO(acac)_2$) to the final +3 state in the V_2O_3. In the present study, thermal decomposition of

$VO(acac)_2$ in the presence of oleylamine, oleic acid and benzyl ether resulted in formation of anosovite V_3O_5 ($V4^{+}$+V^{3+}) nanocrystals. It is fascinating how change in reaction solvents as well as the stoichiometry of the reactants can affect the composition of the resulting nanocrystals. These results motivate future investigations into the effect of different solvents and reagent stoichiometries in nanocrystal syntheses.

Introduction of oleic acid as an additional ligand resulted in formation of anosovite V_3O_5 nanocrystals. Oleic acid and oleylamine can individually form intermediate complexes with the metal ions of the precursors. These metal-ligand complexes are then thermally decomposed or reduced, leading to nanocrystal formation. The underlying chemistry behind the formation of these metal-ligand complexes and their decomposition is complicated, making it very difficult to understand the outcome of the synthesis. Further studies are required to understand if these metal-ligand complex formations proceed in parallel or if these reactions continually compete.

REFERENCES

1. Murray, C. B.; Norris, D. J.; Bawendi, M. G., Synthesis and characterization of nearly monodisperse CdE (E = sulfur, selenium, tellurium) semiconductor nanocrystallites. *J. Am. Chem. Soc.* **2002,** *115*, 8706-8715.

2. Kwon, S. G.; Hyeon, T., Formation mechanisms of uniform nanocrystals via hot-injection and heat-up methods. *Small* **2011,** *7*, 2685-702.

3. van Embden, J.; Chesman, A. S. R.; Jasieniak, J. J., The heat-up synthesis of colloidal nanocrystals. *Chem. Mater.* **2015,** *27*, 2246-2285.

4. Kovalenko, M. V.; Manna, L.; Cabot, A.; Hens, Z.; Talapin, D. V.; Kagan, C. R.; Klimov, V. I.; Rogach, A. L.; Reiss, P.; Milliron, D. J.; Guyot-Sionnnest, P.; Konstantatos, G.; Parak, W. J.; Hyeon, T.; Korgel, B. A.; Murray, C. B.; Heiss, W., Prospects of nanoscience with nanocrystals. *ACS Nano* **2015,** *9*, 1012-57.

5. Larsen, T. H.; Sigman, M.; Ghezelbash, A.; Doty, R. C.; Korgel, B. A., Solventless synthesis of copper sulfide nanorods by thermolysis of a single source thiolate-derived precursor. *J. Am. Chem. Soc.* **2003,** *125*, 5638-9.

6. Zhang, H. T.; Wu, G.; Chen, X. H., Large-scale synthesis and self-assembly of monodisperse hexagon Cu_2S nanoplates. *Langmuir* **2005,** *21*, 4281-2.

7. Ouyang, J., Noninjection, one-pot synthesis of photoluminescent colloidal homogeneously alloyed CdSeS quantum dots. *J. Phys. Chem. C* **2009,** *113*, 5193.

8. Carenco, S., Controlled design of size-tunable monodisperse nickel nanoparticles. *Chem. Mater.* **2010,** *22*, 1340.

9. Park, J.; Kwon, S. G.; Jun, S. W.; Kim, B. H.; Hyeon, T., Large-scale synthesis of ultra-small-sized silver nanoparticles. *ChemPhysChem* **2012,** *13*, 2540-3.

10. Sun, S.; Zeng, H., Size-controlled synthesis of magnetite nanoparticles. *J. Am. Chem. Soc.* **2002,** *124*, 8204-5.

11. Deshmukh, R.; Niederberger, M., Mechanistic aspects in the formation, growth and surface functionalization of metal oxide nanoparticles in organic solvents. *Chem.-Eur. J.* **2017,** *23*, 8542-8570.

12. Niederberger, M.; Garnweitner, G., Organic reaction pathways in the nonaqueous synthesis of metal oxide nanoparticles. *Chem. – Eur. J.* **2006,** *12*, 7282.

13. Hyeon, T., Synthesis of highly crystalline and monodisperse maghemite nanocrystallites without a size-selection process. *J. Am. Chem. Soc.* **2001,** *123*, 12798.

14. Brief, R. S.; Ajemian, R. S.; Confer, R. G., Iron pentacarbonyl: its toxicity, detection, and potential for formation. *Am. Ind. Hyg. Assoc. J.* **1967,** *28*, 21-30.

15. Sodhi, R. K.; Paul, S., An overview of metal acetylacetonates: Developing areas/routes to new materials and applications in organic syntheses. *Catal. Surv. Asia* **2017,** *22*, 31-62.

16. Tsuchiya, T.; Watanabe, A.; Imai, Y.; Niino, H.; Yamaguchi, I.; Manabe, T.; Kumagai, T.; Mizuta, S., Direct conversion of metal acetylacetonates and metal organic acid salts into metal oxides thin films using coating photolysis process with an ArF excimer laser. *Japanese Journal of Applied Physics* **1999,** *38*, L1112.

17. Sun, S., Monodisperse MFe2O4 (M = Fe, Co, Mn) Nanoparticles. *J. Am. Chem. Soc.* **2004,** *126*, 273.

18. Seo, W. S.; Shim, J. H.; Oh, S. J.; Lee, E. K.; Hur, N. H.; Park, J. T., Phase- and size-controlled synthesis of hexagonal and cubic CoO nanocrystals. *J. Am. Chem. Soc.* **2005,** *127*, 6188-9.

19. Nam, K. M.; Shim, J. H.; Ki, H.; Choi, S. I.; Lee, G.; Jang, J. K.; Jo, Y.; Jung, M. H.; Song, H.; Park, J. T., Single-crystalline hollow face-centered-cubic cobalt nanoparticles from solid face-centered-cubic cobalt oxide nanoparticles. *Angew Chem Int Ed Engl* **2008,** *47*, 9504-8.

20. Liu, X.; Swihart, M. T., A general single-pot heating method for morphology, size and luminescence-controllable synthesis of colloidal ZnO nanocrystals. *Nanoscale* **2013,** *5*, 8029.

21. Li, Y.; Afzaal, M.; O'Brien, P., The synthesis of amine-capped magnetic (Fe, Mn, Co, Ni) oxide nanocrystals and their surface modification for aqueous dispersibility. *J. Mater. Chem.* **2006,** *16*, 2175.

22. Seo, W. S.; Jo, H. H.; Lee, K.; Kim, B.; Oh, S. J.; Park, J. T., Size-dependent magnetic properties of colloidal Mn_3O_4 and MnO nanoparticles. *Angew Chem Int Ed Engl* **2004,** *43*, 1115-7.

23. Seo, W. S.; Jo, H. H.; Lee, K.; Park, J. T., Preparation and optical properties of highly crystalline, colloidal, and size-controlled indium oxide nanoparticles. *Adv. Mater.* **2003,** *15*, 795-797.

24. Bergerud, A.; Buonsanti, R.; Jordan-Sweet, J. L.; Milliron, D. J., Synthesis and phase stability of metastable bixbyite V_2O_3 colloidal nanocrystals. *Chem. Mater.* **2013,** *25*, 3172-3179.

25. Davydov, D. A.; Rempel, A. A., Refinement of the V-O Phase Diagram in the Range 25–50 at% Oxygen. *Inorg. Mater.* **2009,** *45*, 47.

26. Banus, M. D.; Reed, T. B.; Strauss, A. J., Electrical and Magnetic Properties of TiO and VO. *Phys. Rev. B.* **1972,** *5*, 2775-2784.

27. Morin, F. J., Oxides which show a metal-to-insulator transition at the neel temperature. *Phys. Rev. Lett.* **1959,** *3*, 34-36.

28. Loehman, R. E.; Rao, C. N. R.; Honig, J. M., Crystallography and defect chemistry of solid solutions of vanadium and titanium oxides. *J. Phys. Chem.* **1969,** *73*, 1781-1784.

29. Pavia, D. L.; Lampman, G. M.; Kriz, G. S.; Vyvyan, J. A., *Introduction to Spectroscopy*. Cengage Learning: 2014.

30. Pinna, N.; Garnweitner, G.; Antonietti, M.; Niederberger, M., A general nonaqueous route to binary metal oxide nanocrystals involving a C-C bond cleavage. *J. Am. Chem. Soc.* **2005,** *127*, 5608-12.

31. Meffre, A.; Lachaize, S.; Gatel, C.; Respaud, M.; Chaudret, B., Use of long chain amine as a reducing agent for the synthesis of high quality monodisperse iron(0) nanoparticles. *J. Mater. Chem.* **2011,** *21*, 13464-13469.

32. Tarannum, M.; Heidtmann, W. P.; Dixon, J. M.; Egusa, S., Valence state-controlled synthesis of vanadium oxide nanocrystals. *J. Phys. Chem. C* **2022,** *127*, 490-498.

33. Buonsanti, R.; Grillo, V.; Carlino, E.; Giannini, C.; Kipp, T.; Cingolani, R.; Cozzoli, P. D., Nonhydrolytic synthesis of high-quality anisotropically shaped brookite TiO_2 nanocrystals. *J. Am. Chem. Soc.* **2008,** *130*, 11223-33.

34. Yu, H.; Gibbons, P. C.; Kelton, K. F.; Buhro, W. E., Heterogeneous seeded growth: a potentially general synthesis of monodisperse metallic nanoparticles. *J. Am. Chem. Soc.* **2001,** *123*, 9198-9.

35. Jana, N. R.; Gearheart, L.; Murphy, C. J., Evidence for seed-mediated nucleation in the chemical reduction of gold salts to gold nanoparticles. *Chem. Mater.* **2001,** *13*, 2313-2322.

36. Gordon, T. R.; Cargnello, M.; Paik, T.; Mangolini, F.; Weber, R. T.; Fornasiero, P.; Murray, C. B., Nonaqueous synthesis of TiO_2 nanocrystals using TiF_4 to engineer morphology, oxygen vacancy concentration, and photocatalytic activity. *J. Am. Chem. Soc.* **2012,** *134*, 6751-61.

37. Mourdikoudis, S.; Menelaou, M.; Fiuza-Maneiro, N.; Zheng, G.; Wei, S.; Perez-Juste, J.; Polavarapu, L.; Sofer, Z., Oleic acid/oleylamine ligand pair: a versatile combination in the synthesis of colloidal nanoparticles. *Nanoscale Horiz.* **2022,** *7*, 941-1015.

CHAPTER 5 : CONCLUSION & FUTURE WORK

5.1 Conclusion

In this dissertation, colloidal syntheses of vanadium oxide nanocrystals were explored, and characterization of the resulting nanocrystals were discussed. In chapter 2, a valence-state controlled synthesis of vanadium oxide nanocrystals was presented. Using a hot-injection method, colloidal synthesis of newly discovered anosovite polymorph of V_3O_5 was demonstrated for the first time. The effect of varying V/ODE/OAm ratios on resulting crystalline phases, particle sizes, and morphologies was evaluated. It was found that presence of excess alcohol in the synthesis negatively impacted V_3O_5 nanocrystal formation, resulting in poor yield. Notably, anosovite V_3O_5 formation occurred within a broad parameter space of V/ODE/OAm = 1:[1–7]:[2–7], while corundum-structured V_2O_3 formation required a narrower range of V/ODE/OAm = 1:[7–9]:[1.5–2]. Examination of the kinetics of the nanocrystal growth indicated a slow nucleation followed by a delayed growth. Furthermore, the nanocrystal growth occurred via an Ostwald ripening process. The reaction pathways leading to the formation of the nanocrystals were investigated with time-course ATR-FTIR spectroscopy. Alkyl halide elimination and aminolysis pathways were identified as key intermediate processes in the reaction. Phase stability of the metastable anosovite V_3O_5 was evaluated at different temperatures. The nanocrystals showed superior stability compared to the bulk due to the high surface-to-volume ratio and the presence of the surface ligand.

In Chapter 3, another method to selectively synthesize pure corundum-structured V_2O_3 nanocrystals was presented. It was demonstrated that the choice of alcohol influenced the reduction of the V^{5+} precursor and the reaction pathway in the synthesis. More specifically, V_2O_3 formation occurred in the presence of benzyl alcohol while anosovite V_3O_5 resulted with octadecanol, with V/alcohol/oleylamine ratio of 1:7:3. The synthesis of V_2O_3 nanocrystals using benzyl alcohol

involved an S_N1 reaction mechanism, where benzyl carbocation forms and undergoes nucleophilic substitution with amino groups to form benzylamine, leading to a metal hydroxide species that undergoes condensation to form metal oxide. Diffuse reflectance spectroscopy revealed deviations in the properties of V_2O_3 nanocrystals from bulk electronic behavior. This discrepancy occurred likely due to broadening of the a_{1g} band in V_2O_3 nanocrystals. Spectroscopic ellipsometry was employed to determine the optical properties of the nanocrystal films including complex dielectric constants and optical conductivity.

This dissertation facilitated formation of anosovite V_3O_5 nanocrystals for the first time, from readily available precursors. We presented the optical constants of the V_3O_5 nanocrystal films in the 0.73 eV − 3.1 eV range. A direct bandgap energy of ~ 2 eV for direct allowed transition was deduced from Tauc-plot analysis of the absorbance spectra of V_3O_5 nanocrystals.

In chapter 4, a heat-up method for synthesis of VOx nanocrystals was discussed. Thermal decomposition of Vanadyl (IV) acetylacetonate in the presence of oleylamine and benzyl ether resulted in formation of vanadium monoxide nanocrystals. FTIR analysis of the reaction intermediates suggested formation of an intermediate complex between $VO(acac)_2$ and oleylamine, and an additional amide byproduct during synthesis. Seeded growth approaches were explored to achieve size control of the nanocrystals. However, they did not enhance size control as anticipated. Using oleic acid as an additional ligand led to the formation of anosovite V_3O_5 nanocrystals. Further studies are required to understand the reaction pathway that leads to the formation of V_3O_5 when oleic acid is present, in comparison to the formation of VO_x when oleic acid is absent.

5.2 Future work

This dissertation serves as a starting point for the study of anosovite V_3O_5 nanocrystals. Since the initial discovery in 2012,[1] no other routes to synthesize anosovite V_3O_5 has been reported except for this work.[2] Further theoretical and experimental studies are needed for a complete understanding of the physical properties of this material in nanoscale. Theoretical studies on anosovite V_3O_5 should be conducted to calculate the electronic band structure which is crucial for understanding its electronic, magnetic, and optical properties.

The optical constants and optical conductivity of V_3O_5 and V_2O_3 nanocrystal films were reported in this work in the photon energy range of $0.7 - 3.1$ eV.[3] Further optical studies are needed to complete the picture in the IR region of the spectra. Corundum-structured V_2O_3 films have been known to exhibit Drude-like characteristics in the IR region of the optical conductivity spectra.[4] It is of great interest to investigate whether nanocrystalline V_2O_3 will exhibit similar characteristics or not.

V_2O_3 undergoes phase transition from the monoclinic antiferromagnetic insulating (AFI) state to the corundum paramagnetic metallic (PM) state at a transition temperature of ~150 K at ambient pressure.[5] In a previous study, Ishibashi and coworkers suggested that the size control of V_2O_3 down to ~10 nm yields a spontaneous uniaxial strain along the c axis leading to the disappearance of the metal-insulator transition.[6] This strain causes contraction along the c axis, broadening the a_{1g} band and enhancing the mixing of the a_{1g} and e_g^{π} bands. The researchers concluded that this spontaneous uniaxial strain is specific to nanocrystals with a large surface area to volume ratio, stabilizing the metallic phase far below the bulk IMT temperature. Later, the same group of researchers reported that Cr – doping in V_2O_3 nanocrystals induces narrowing of the a_{1g} band and effectively sustains the IMT.[7] The synthetic route to obtain V_2O_3 nanocrystals in this dissertation

can be modified to obtain doped V_2O_3 nanocrystals and characterized to corroborate the above-mentioned findings.

This dissertation explored the hot-injection synthesis and heat-up synthesis of vanadium oxide nanocrystals using vanadium (V) oxytrichloride ($VOCl_3$) and vanadyl (IV) acetylacetonate ($VO(acac)_2$)as the precursor, respectively. Other precursors e.g. vanadium (III) acetylacetonate, vanadium sulfate ($VOSO_4$) as well as different synthetic methods (heat-up synthesis, continuous injection) should be explored. Such exploration will open new opportunities to selectively synthesize vanadium oxides in desired oxidation state and crystal structure without necessitating high temperature annealing.

REFERENCES

1. Weber, D.; Wessel, C.; Reimann, C.; Schwickert, C.; Muller, A.; Ressler, T.; Pottgen, R.; Bredow, T.; Dronskowski, R.; Lerch, M., Anosovite-type V_3O_5: a new binary oxide of vanadium. *Inorg. Chem.* **2012,** *51*, 8524-8529.

2. Tarannum, M.; Heidtmann, W. P.; Dixon, J. M.; Egusa, S., Valence state-controlled synthesis of vanadium oxide nanocrystals. *J. Phys. Chem. C* **2022,** *127*, 490-498.

3. Tarannum, M.; Egusa, S., Optical properties of correlated metallic V_2O_3 and anosovite V_3O_5 nanocrystals and nanocrystal films. *J. Phys. Chem. C* **2024,** *128*, 4215-4223.

4. Qazilbash, M. M.; Schafgans, A. A.; Burch, K. S.; Yun, S. J.; Chae, B. G.; Kim, B. J.; Kim, H. T.; Basov, D. N., Electrodynamics of the vanadium oxides VO_2 and V_2O_3. *Phys. Rev. B* **2008,** *77*, 115121.

5. Imada, M.; Fujimori, A.; Tokura, Y., Metal-insulator transitions. *Rev. Mod. Phys.* **1998,** *70*, 1039-1263.

6. Ishiwata, Y.; Suehiro, S.; Kida, T.; Ishii, H.; Tezuka, Y.; Oosato, H.; Watanabe, E.; Tsuya, D.; Inagaki, Y.; Kawae, T., Spontaneous uniaxial strain and disappearance of the metal-insulator transition in monodisperse V_2O_3 nanocrystals. *Phys. Rev. B* **2012,** *86*, 035449.

7. Ishiwata, Y.; Shiraishi, T.; Ito, N.; Suehiro, S.; Kida, T.; Ishii, H.; Tezuka, Y.; Inagaki, Y.; Kawae, T.; Oosato, H.; Watanabe, E.; Tsuya, D.; Nantoh, M.; Ishibashi, K., Metal-insulator transition sustained by Cr-doping in V_2O_3 nanocrystals. *Appl. Phys. Lett.* **2012,** *100*, 043103.

APPENDIX A: SUPPORTING INFORMATION FOR CHAPTER 3

This appendix includes results of Rietveld refinement for the XRD pattern of V_3O_5 nanocrystals. It also includes TEM images and XRD patterns of nanocrystals synthesized in excess alcohol, VO_x nanoparticles and nanocrystals synthesized in different solvents (octyl ether and squalene). Time-course TEM images of V_2O_3 nanocrystal formation are presented. Time-course FTIR spectra of reaction intermediates as well as control reactions involving alcohol and amine are provided. Additionally, it provides a TEM image of the sample obtained in a control reaction ($VOCl_3$:OAm:ODE=1:7:0), studies on the phase stability of anosovite V_3O_5 nanocrystals and evaluation of oleylamine stability.

Table A.1. Results of Rietveld Refinement

Crystal System	Orthorhombic
Space Group	*Bbmm*
Unit Cell Dimensions	a = 9.66518 Å, b = 9.90535 Å, c = 3.70572 Å, β = 90°
Unit Cell Volume	354.774 × 10^6 pm^3
Calculated Density	4.359 g/cc
2θ range	10°-60°
Radiation	Cu/Kα
Wavelength	1.5418 Å
Temperature of Measurement	25°C
Method of Refinement and Program	GSAS + EXPGUI
Number of Refined Parameters	29
R_p	8.557
R_{wp}	4.497
χ^2	1.46

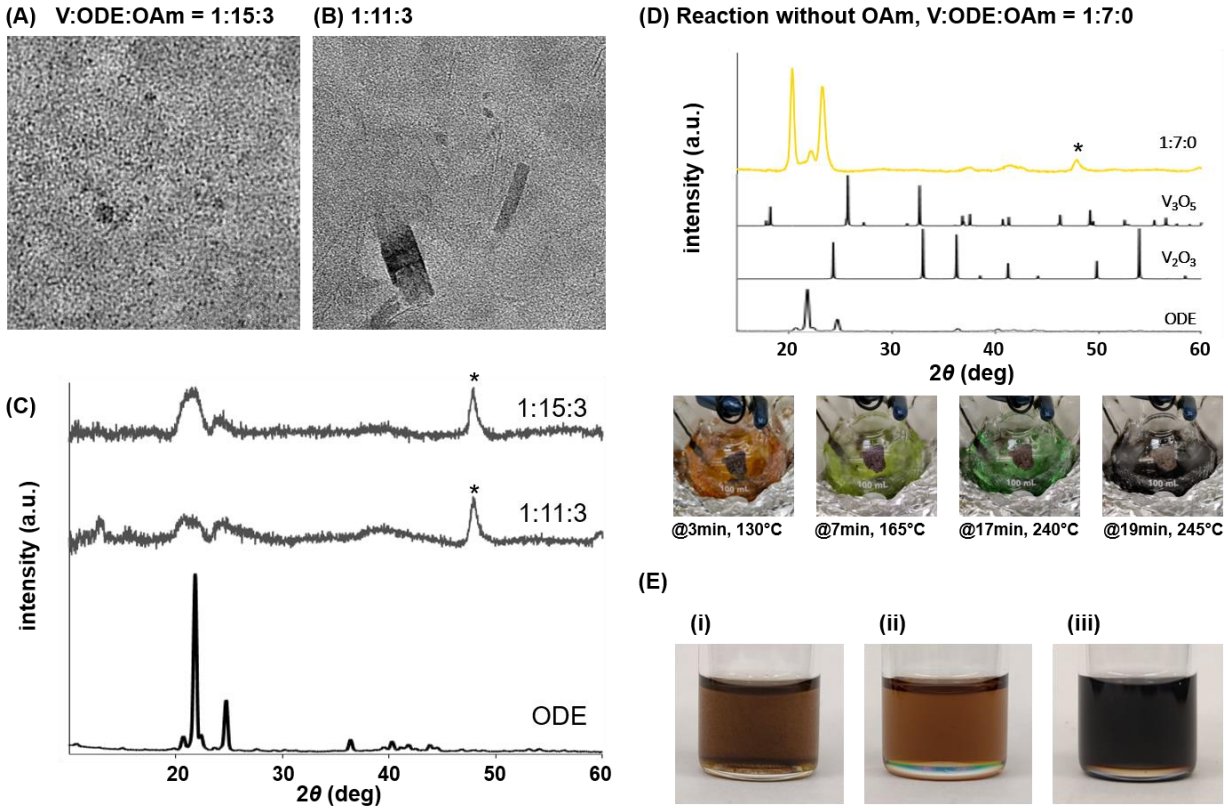

Figure A.1. Effect of excess alcohol. TEM images of nanoparticles synthesized with V:ODE:OAm ratio of (A) 1:15:3 and (B) 1:11:3 (Scale bar = 50 nm). (C) XRD patterns for 1:15:3 and 1:11:3 comprised peaks from excess ODE and the unindexed peak at $2\theta = 47.90°$ (*). (D) The unindexed peak is a compound result from reacting $VOCl_3$ and ODE. This is evidenced by XRD of the compound obtained with the reaction with V:ODE:OAm = 1:7:0, kept at 250 °C for 20 min, showing the same $2\theta = 47.90°$ (*) peak along with unreacted ODE. Interestingly, in the absence of OAm, reduction of V^{5+} was observed by the color change of orange → yellow-green → blue-green. (E) The color of the compound exhibiting $2\theta = 47.90°$ (*) peak was brown (picture (i)), similar to that of V:ODE:OAm = 1:7:0 (picture (ii)). On the other hand, the color of pure V_3O_5 was black (picture (iii)).

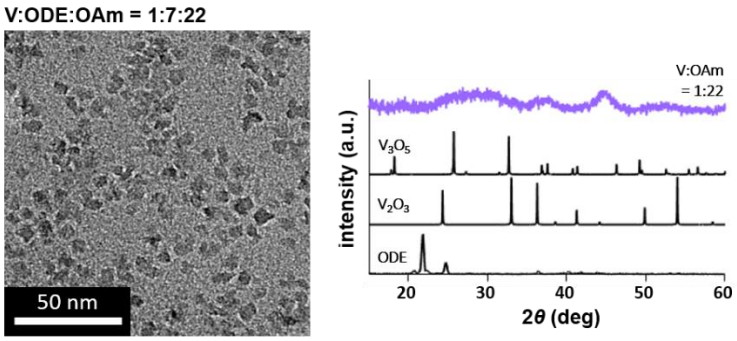

Figure A.2. Formation of VO_x nanoparticles. With V:ODE:OAm ratio 1:7:22 (no HD was used), the product was small sub-10 nm nanoparticles. The XRD patterns showed broad low-intensity peaks similar to that obtained with V:ODE:OAm ratio 1:7:40 (Figure 4A), presumably due to an amorphous structure (VO_x)[1] (indicated by the "hump" at $2\theta \sim 25 - 35°$). These findings are consistent with those reported by Murray and co-workers[2].

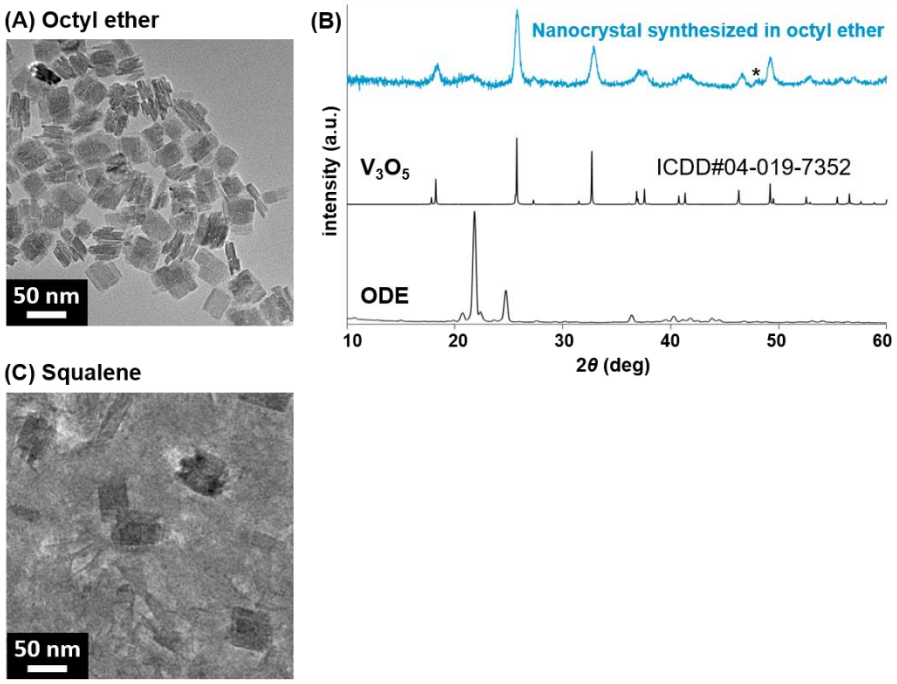

Figure A.3. Effects of solvents. (A) TEM image of nanocrystals synthesized in octyl ether with V:ODE:OAm = 1:7:3, and (B) XRD pattern indexed to anosovite V_3O_5, along with the unindexed peak at $2\theta = 47.90°$ (*). (C) TEM image of the product synthesized in squalene with V:ODE:OAm = 1:7:3.

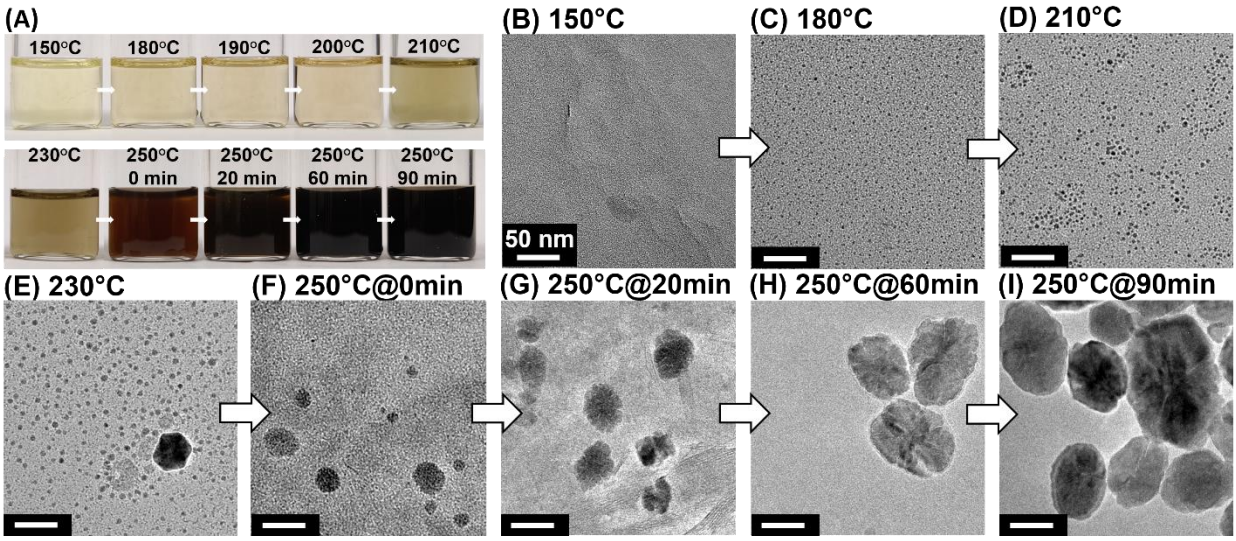

Figure A.4. (A) Evolution in the color of reaction solution during V_2O_3 nanocrystal synthesis. TEM image of the aliquot taken at (B) 150 °C, (C) 180 °C, (D) 210 °C and (E) 230 °C showing slow nucleation. (F) TEM image of the aliquot taken upon reaching 250 °C at 0 min, and (G) maintaining 250 °C at 20 min, (H) at 60 min, and (I) 90 min, showing subsequent growth of nanocrystals by Ostwald Ripening. (Scale bar = 50 nm)

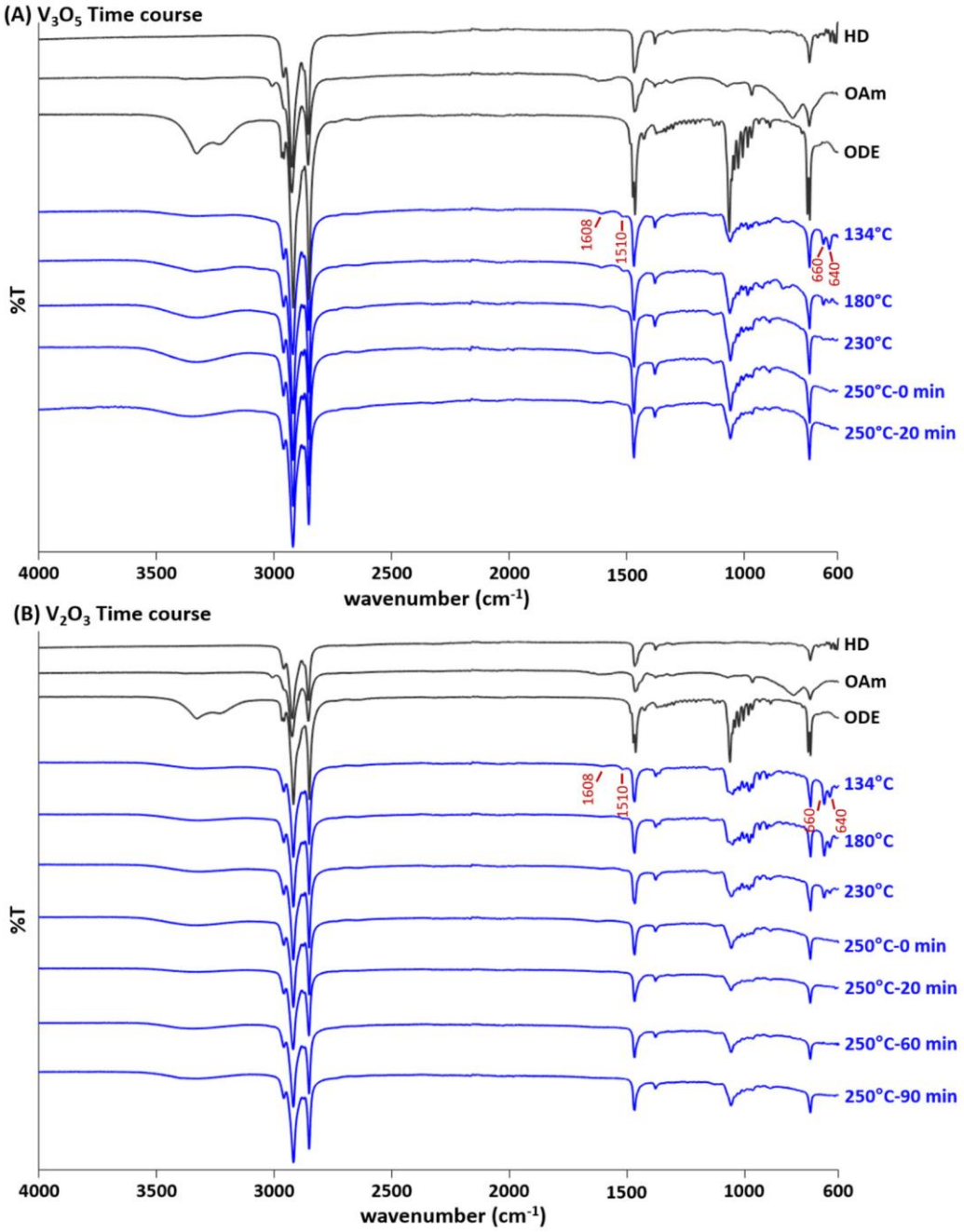

Figure A.5. FTIR spectra of reaction intermediates. FTIR spectra of the aliquots collected during the time-course of (A) V_3O_5 and (B) V_2O_3 nanocrystal synthesis. Immediately after $VOCl_3$ injection, the FTIR spectra of both V:ODE:OAm=1:7:3 (V_3O_5 synthesis) and 1:7:2 (V_2O_3 synthesis) showed new peaks at ~640 cm^{-1}, ~660 cm^{-1}, ~1608 and ~1510 cm^{-1}. FTIR spectra of the controls are shown at the top: heptadecane (HD), oleylamine (OAm), and 1-octadecanol (ODE).

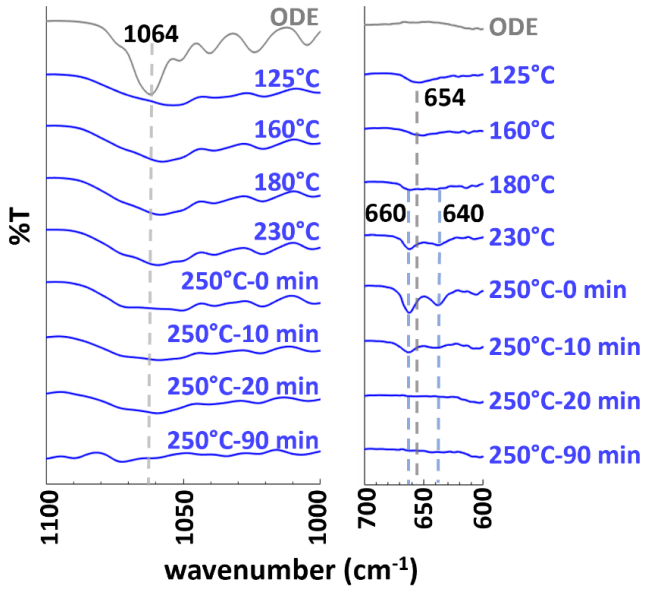

Figure A.6. Time course FTIR spectra of control reaction with alcohol (no amine). FT-IR spectrum of pure 1-octadecanol (ODE) and aliquots of a mixture of $VOCl_3$:ODE at 1:7 molar ratio, which was heated up at 5 °C/min up to 250 °C and then kept at this temperature for additional 90 minutes. Upon $VOCl_3$ injection at 125 °C, the C−O stretch peak (1064 cm^{-1}) of ODE broadened while shifting to shorter wavenumbers and gradually decreased while the reaction mixture was kept at 250 °C for 90 minutes. Simultaneously, a broad peak appeared at 654 cm^{-1} indicating a complex formation between ODE and $VOCl_3$. With continued heating, peaks appeared at 640 cm^{-1} (V−OR bend) and 660 cm^{-1} (C−Cl stretch) indicating the presence of alkyl halide elimination pathway[3] which yields an alkoxo chloro oxovanadium compound $(VOCl_{x-y}(OR)_y)$[4-6] and an alkyl halide byproduct.[7] Further heating and maintaining the temperature at 250 °C for 20 min resulted in the gradual disappearance of the V−OR and C−Cl stretch peaks.

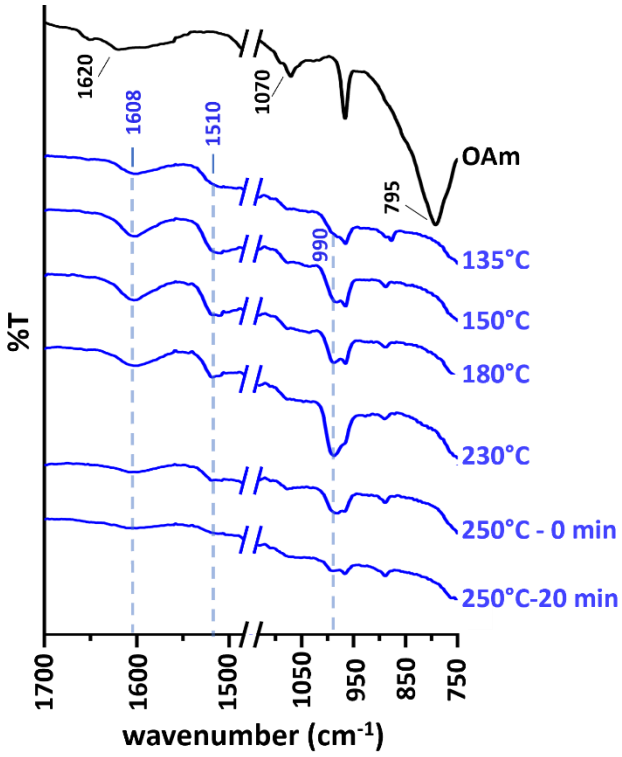

Figure A.7. Time course FTIR spectra of control reaction with amine (no alcohol). FT-IR pure oleylamine (OAm) and aliquots of a mixture of $VOCl_3$:OAm at 1:3 molar ratio, which was heated up at 5 °C/min up to 250 °C and maintained for additional 20 minutes. Upon $VOCl_3$ injection at 125 °C, N−H bend peaks (795 cm^{-1} and 1620 cm^{-1}) and the C−N bend peak (1070 cm^{-1}) of oleylamine disappeared. Simultaneously, two peaks appeared at 1608 and 1510 cm^{-1} indicating the presence of an amine-hydrochloride reaction by-product[8]. The peak at 990 cm^{-1} was assigned to V=O stretching vibration.[9] These spectral changes suggest the formation of a chloro-amino vanadium complexes.[10, 11]

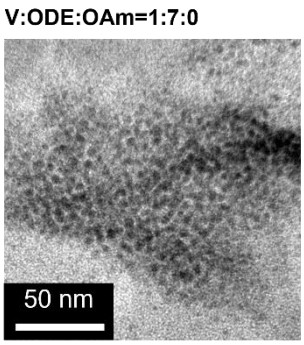

Figure A.8. TEM image of control reaction with amine (no alcohol). With V:ODE:OAm ratio 1:7:0, nanocrystals could not be obtained. The XRD pattern of the sample could not be indexed to known vanadium oxides (please refer to Figure A.1 D).

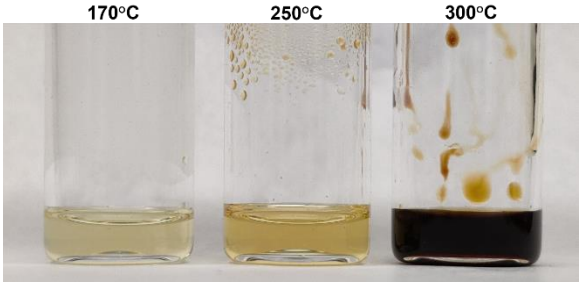

Figure A.9. Stability of oleylamine. Color change and evaporation of oleylamine (70%, technical grade) as heated from room temperature to 170 °C, 250 °C and 300 °C respectively.

REFERENCES

1. Cullity, B. D.; Stock, S. R.; Stock, S. R., *Elements of x-ray diffraction*. Prentice Hall: 2001.

2. Paik, T.; Hong, S. H.; Gaulding, E. A.; Caglayan, H.; Gordon, T. R.; Engheta, N.; Kagan, C. R.; Murray, C. B., Solution-processed phase-change VO_2 metamaterials from colloidal vanadium oxide (VO_x) nanocrystals. *ACS Nano* **2014,** *8*, 797-806.

3. Niederberger, M.; Pinna, N., *Metal oxide nanoparticles in organic solvents: synthesis, formation, assembly and application*. Springer Science & Business Media: 2009.

4. Crans, D. C.; Chen, H. J.; Felty, R. A., Synthesis and reactivity of oxovanadium(V) trialkoxides of bulky and chiral alcohols. *J. Am. Chem. Soc.* **1992,** *114*, 4543-4550.

5. Rosenthal, E. C.; Cui, H.; Koch, J.; Escarpa Gaede, P.; Hummert, M.; Dechert, S., Chloride-bridged oxovanadium(V) complexes with alkoxyalkoxide ligands. Synthesis, structure, electrochemistry and reactivities. *Dalton Trans* **2005**, 3108-17.

6. Miles, S. J.; Wilkins, J. D., Coordination Chemistry of methoxydichlorooxovanadium(V). *J. lnorg. Nucl. Chem.* **1975,** *37*, 2271-2276.

7. Smith, B. C., *Infrared Spectral Interpretation: A Systematic Approach*. CRC Press: 2018.

8. Nakanishi, K.; Goto, T.; Ohashi, M., Infrared spectra of organic ammonium compounds. *Bull. Chem. Soc. Jpn.* **1957,** *30*, 403-408.

9. Barraclough, C. G.; Lewis, J.; Nyholm, R. S., The stretching frequencies of metal–oxygen double bonds. *J. Chem. Soc.* **1959,** *0*, 3552-3555.

10. Baker, K. L.; Edwards, D. A.; Fowles, G. W. A.; Williams, R. G., The reduction of vanadium(V) oxytrichloride by aliphatic amines and thioethers. *J. lnorg. Nucl. Chem.* **1967,** *29*, 1881-1885.

11. Fowles, G. W. A., Reaction of metal halides with ammonia and aliphatic amines. *Prog. Inorg. Chem.*, 1964; pp 1-36.

APPENDIX B: SUPPORTING INFORMATION FOR CHAPTER 4

This appendix includes the XRD pattern of V_2O_3 and V_3O_5 nanocrystals, TEM images showing morphological evolution of V_2O_3 nanocrystals synthesized in varying benzyl alcohol concentration. The S_N1 reaction mechanism for nanocrystal formation is illustrated. The effect of alcohol in nanocrystal synthesis is shown. FTIR spectra of reaction intermediates for V_2O_3 nanocrystal synthesis (V:BnOH:OAm=1:7:3) and the control reaction (V:BnOH:OAm=1:7:0) are provided. Images of nanocrystal films obtained by spin-coating are shown. Results of SiO_2 layer thickness measurement on the Si substrate using spectroscopic ellipsometry and ellipsometry model fit parameters are provided. Tauc plot to determine the indirect bandgap of V_3O_5 nanocrystals is included.

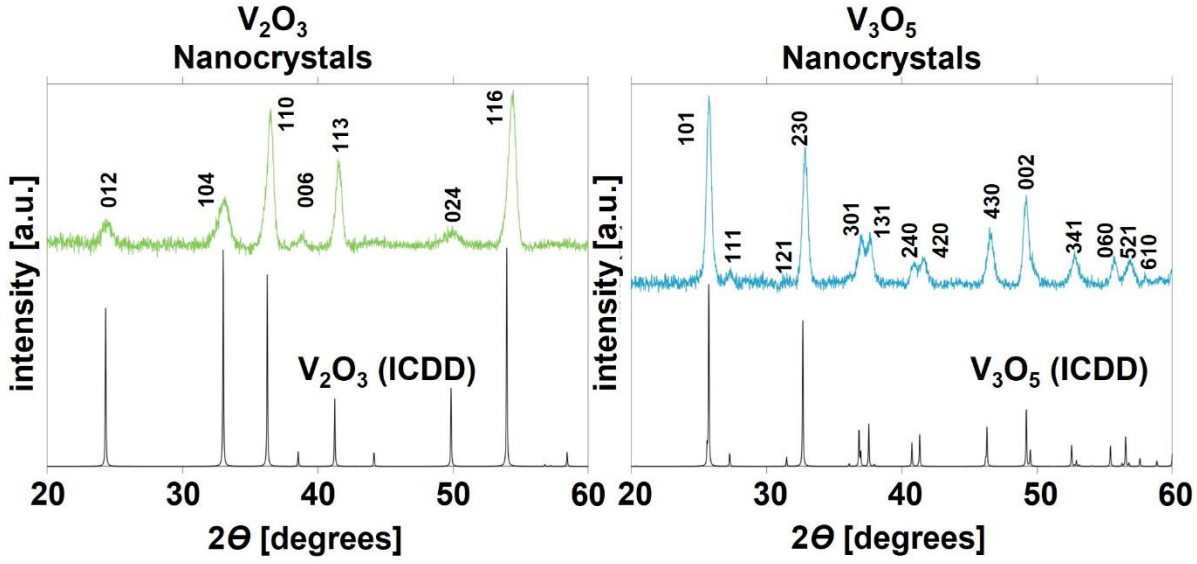

Figure B.1. XRD of V_2O_3 and V_3O_5 nanocrystals. XRD patterns of nanocrystals with indexed peaks. Reference spectra: corundum structured V_2O_3 (ICDD#01-071-0280) and anosovite V_3O_5 (ICDD#04-019-7352).

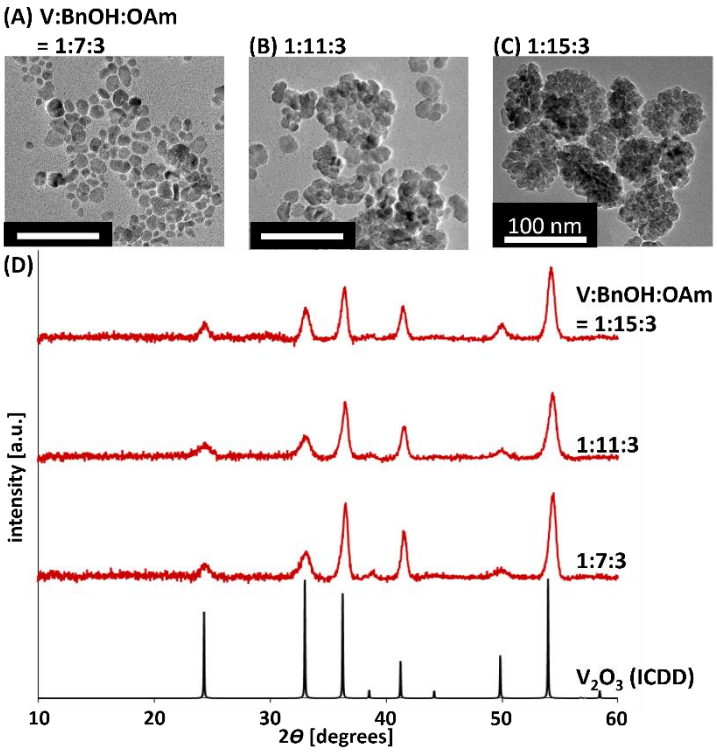

Figure B.2. Morphology of V_2O_3 nanocrystals. V_2O_3 nanocrystals were synthesized with varied BnOH/V ratios, keeping OAm/V = 3. (A – C) TEM images of the samples with increasing BnOH/V ratios showed evolution of the morphology into nanoflowers (Scale bar = 100 nm). (D) XRD patterns of nanocrystals synthesized with the V:BnOH:OAm ratios in the range of 1:[7–15]:3 confirmed corundum crystal structure. Reference spectra: corundum V_2O_3 (ICDD#01-071-0280).

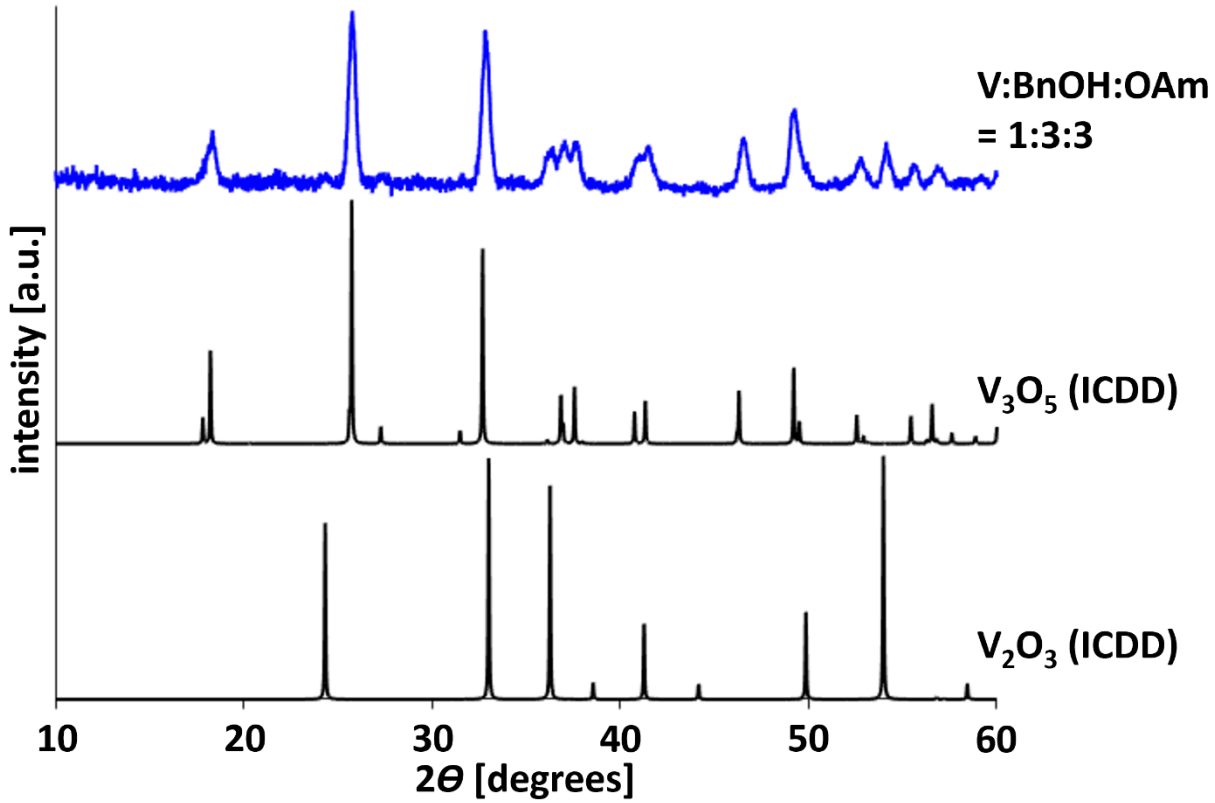

Figure B.3. Effect of alcohol in nanocrystal synthesis. XRD pattern of nanocrystals synthesized with V:BnOH:OAm = 1:3:3 showing a mixture of anosovite V_3O_5 and corundum structured V_2O_3 phase. Reference spectra: anosovite V_3O_5 (ICDD#04-019-7352) and corundum structured V_2O_3 (ICDD#01-071-0280).

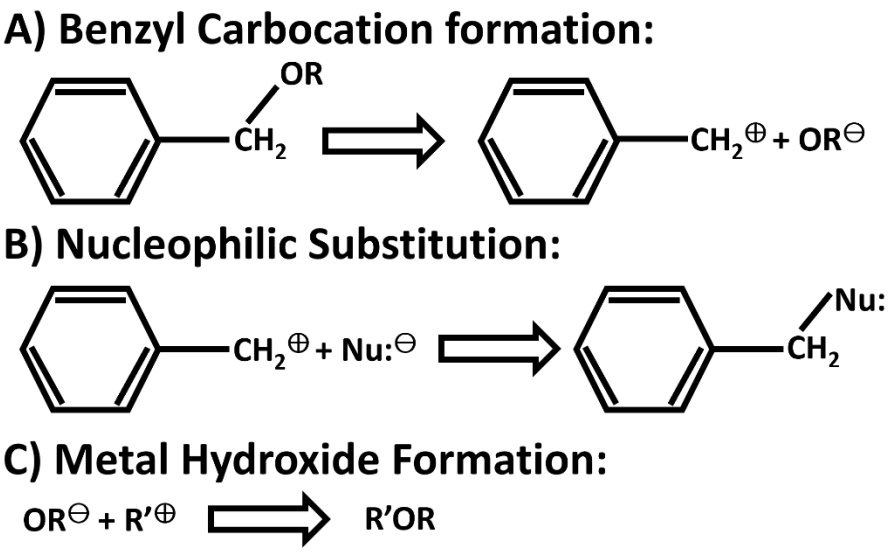

Figure B.4. S_N1 reaction mechanism for nanocrystal formation. Nu: stands for nucleophilic agents, such as Cl^- ions, amino, benzyloxy group.

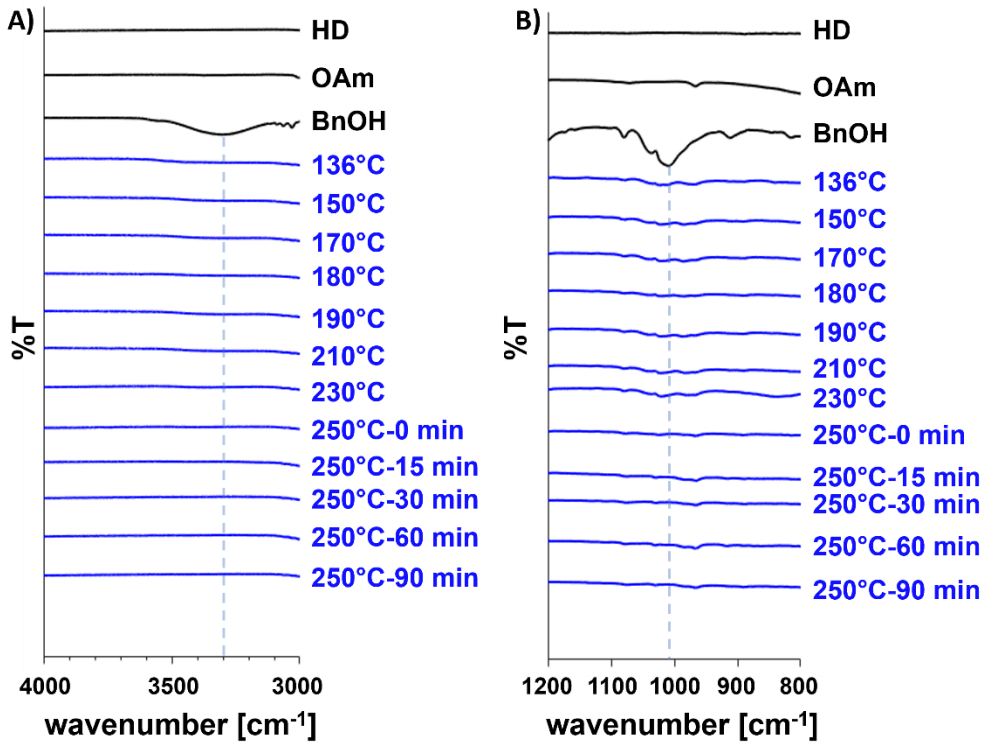

Figure B.5. ATR-FTIR spectra of reaction mixtures collected at different intervals during the heating of V:BnOH:OAm=1:7:3 (V_2O_3 nanocrystal synthesis). Reference spectra for Heptadecane (HD) and benzyl alcohol (BnOH) are shown (black solid line). Upon $VOCl_3$ injection, the O – H (~ 3300 cm^{-1}) and C – O (~ 1018 cm^{-1}) stretching vibrations of benzyl alcohol diminished indicating benzyl carbocation formation in the reaction.

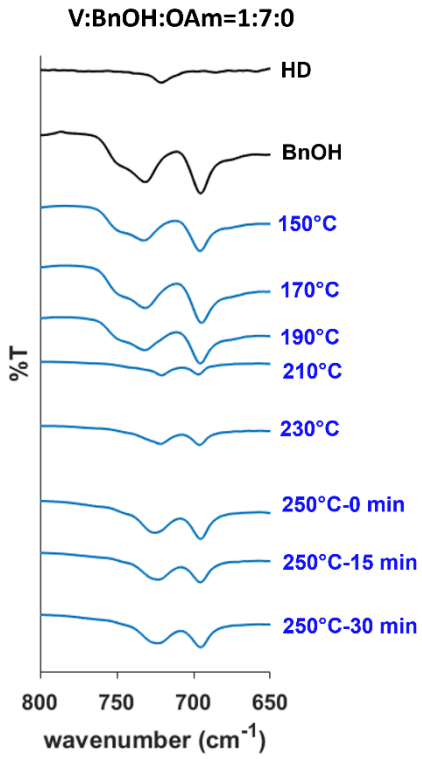

Figure B.6. ATR-FTIR spectra of reaction mixtures collected at different intervals during the heating of V:BnOH:OAm=1:7:0 (control) synthesis. Reference spectra for Heptadecane (HD) and benzyl alcohol (BnOH) are shown (black solid line). In the absence of oleylamine in the reaction, no peak at ~740 cm^{-1} related to benzylamine formation was observed.

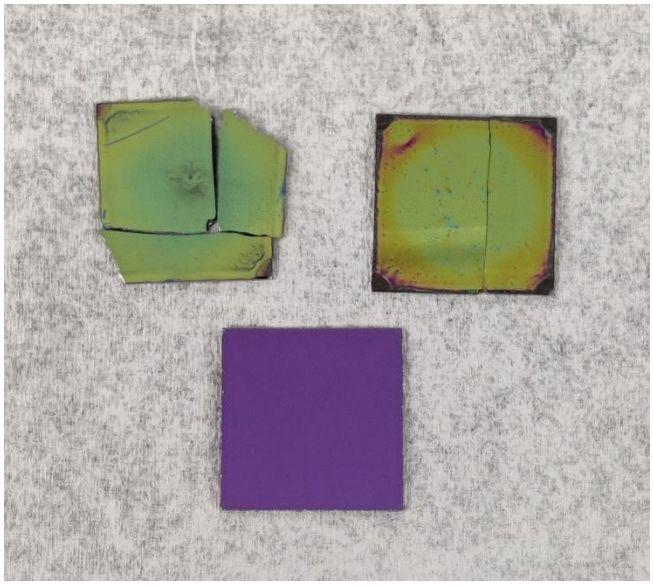

Figure B.7. V_2O_3 (top left) and V_3O_5 (top right) nanocrystal films spin coated on SiO_2/Si wafer. Samples were cleaved to determine the film thickness using SEM. A blank SiO_2/Si substrate is shown in the bottom for comparison between coated and bare substrate.

SiO_2	304.206 nm
Si	0.5 mm

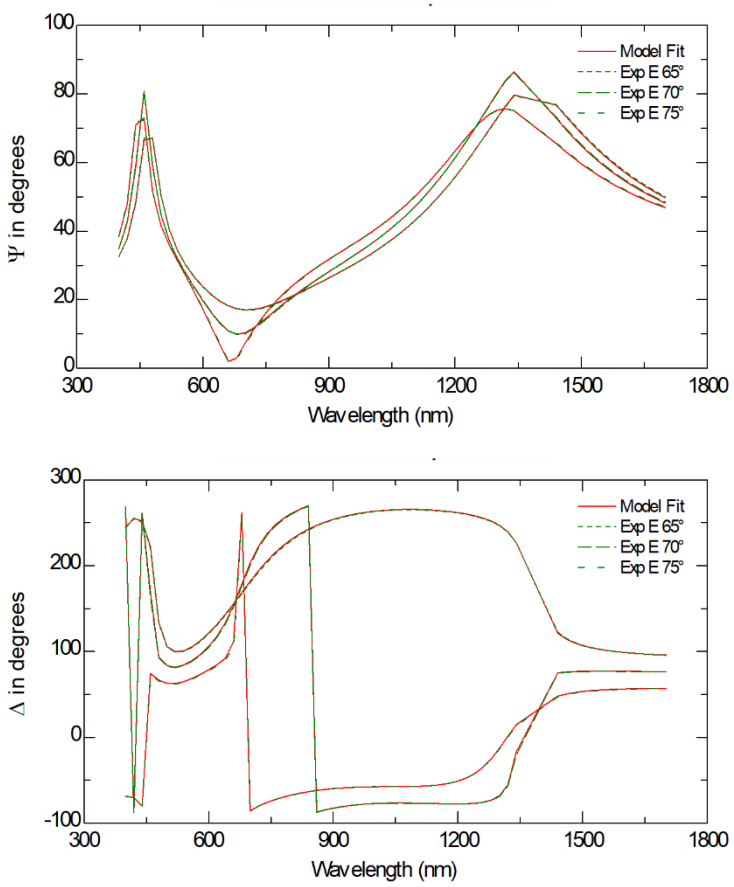

Figure B.8. Measurement of SiO_2 layer thickness on Si substrate using spectroscopic ellipsometry. A two-layer model (SiO_2 layer on top of 0.5 mm Si layer at bottom) was used to fit the SE data using the optical constants in the WVase materials directory. The SiO_2 layer thickness was determined to be 304.206 nm.

Table B.1. Ellipsometry fit parameters for V_2O_3 nanocrystal film on 300 nm SiO_2/.5 mm Si.

MSE = 12.18	
Common parameters	
V_2O_3 thickness	40.555±1.55 nm
SiO_2 Thickness	304.000±1.84 nm
$\varepsilon_{1\ Offset}$	3.5346±0.0444
Thickness Non-Uniformity	8.3775±0.526 nm
Lorentz Oscillator 1	
Amplitude, A_1	4.1965±0.153
Energy, E_{01}	0.84737±0.0305
Broadening, Γ_1	1.8459±0.185
Lorentz Oscillator 2	
Amplitude, A_2	0.2871±0.0714
Energy, E_{02}	2.7828±0.274
Broadening, Γ_2	2.9164±1.37

Table B.2. Ellipsometry model fit parameters with three Lorentz oscillators for V_2O_3 nanocrystal film on 300 nm SiO_2/.5 mm Si.

MSE = 12.46	
Common parameters	
V_2O_3 thickness	39.590±2.17 nm
SiO_2 Thickness	305.191±2.5 nm
$\varepsilon_{1\ Offset}$	3.4459±0.321
Thickness Non-Uniformity	8.4254±0.553 nm
Lorentz Oscillator 1	
Amplitude, A_1	4.1079±0.193
Energy, E_{01}	0.89903±0.0298
Broadening, Γ_1	2.2045±0.197
Lorentz Oscillator 2	
Amplitude, A_2	0.11635±0.179
Energy, E_{02}	2.5±0.562
Broadening, Γ_2	1.4105±2.15
Lorentz Oscillator 2	
Amplitude, A_3	0.50647±0.906
Energy, E_{03}	4±3.47
Broadening, Γ_3	0.87413±4.25

Table B.3. Ellipsometry fit parameters for V_3O_5 nanocrystal film on 300 nm SiO_2/.5 mm Si considering three angles of incidence.

MSE = 7.192	
Common parameters	
V_3O_5 thickness	83.854±0.535 nm
SiO_2 Thickness	276.532±0.683 nm
$\varepsilon_{1\ Offset}$	1.3902±0.342
Thickness Non-Uniformity	8.3437±0.142 nm
Pole Position	6.0175±0.519
Pole Magnitude	55.327±21.6
Lorentz Oscillator	
Amplitude, A	3.0189±0.186
Energy, E	0.43974±0.0207
Broadening, Γ	5.3213±1.7
Gaussian Oscillator	
Amplitude, A	0.45166±0.117
Energy, E	0.86194±0.0119
Broadening, Γ	1.2756±0.0992

Table B.4. Ellipsometry model fit parameters considering four angles of incidence for V_3O_5 nanocrystal film on 300 nm SiO_2/.5 mm Si.

MSE = 7.861	
Common parameters	
V_3O_5 thickness	83.034±0.496 nm
SiO_2 Thickness	277.749±0.621 nm
$\varepsilon_{1\ Offset}$	1.5174±0.288
Thickness Non-Uniformity	7.7799±0.0925 nm
Pole Position	5.8007±0.465
Pole Magnitude	45.755±17
Lorentz Oscillator	
Amplitude, A	0.4086±0.0812
Energy, E	3.303±0.752
Broadening, Γ	8.8981±6.56
Gaussian Oscillator	
Amplitude, A	0.24842±0.194
Energy, E	0.92224±0.138
Broadening, Γ	1.0629±0.257

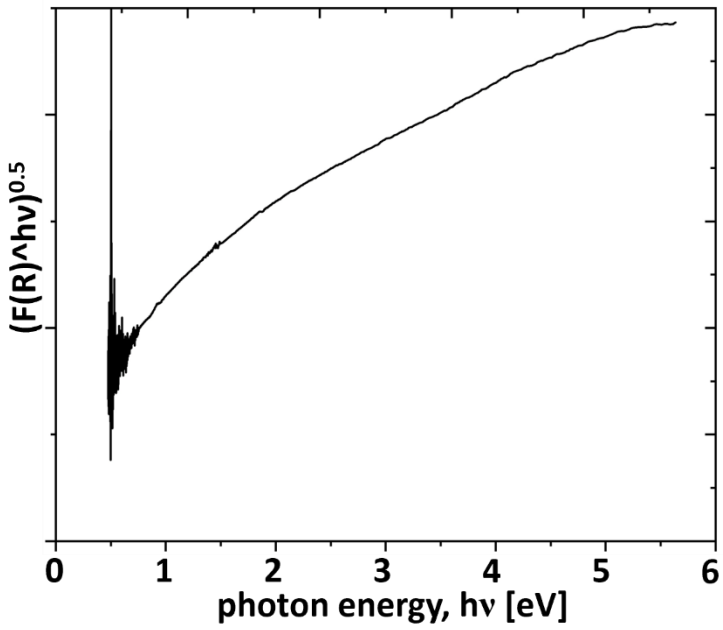

Figure B.9. Tauc plot analysis for indirect transition in V_3O_5 nanocrystals. Plot of $[F(R)\cdot h\nu]^{1/2}$ vs hν showing no available linear region to be extrapolated for indirect absorption edge determination for V_3O_5 nanocrystals.

TECHNICAL PUBLICATIONS

1. Tarannum, M.; Egusa, S. Optical properties of correlated metallic V_2O_3 and anosovite V_3O_5 nanocrystal films. *The Journal of Physical Chemistry C* 2024, *128* (10), 4215-4233.

2. Tarannum, M.; Heidtmann, W. P.; Dixon, J. M.; Egusa, S. Valence state-controlled synthesis of vanadium oxide nanocrystals. *The Journal of Physical Chemistry C* 2022, *127* (1), 490-498.

3. Palermo, G.; **Tarannum, M.**; Egusa, S. Luminescence onset and mechanism of the formation of gold(I)–thiolate complexes as the precursors to nanoparticles. *The Journal of Physical Chemistry C* 2020, *124* (20), 11248-11255.